# Investigating the Memory Effect in Neutron Star Mergers

**Auteur :** Brabant, Thomas
**Promoteur(s) :** 31306; Cudell, Jean-René
**Faculté :** Faculté des Sciences
**Diplôme :** Master en sciences spatiales, à finalité approfondie
**Année académique :** 2025-2026
**URI/URL :** http://hdl.handle.net/2268.2/25509

# Investigating the Memory Effect in Neutron Star Mergers

Submitted in partial fulfillment of the requirements
For the degree of Master in Space Science, research focus

by

THOMAS BRABANT

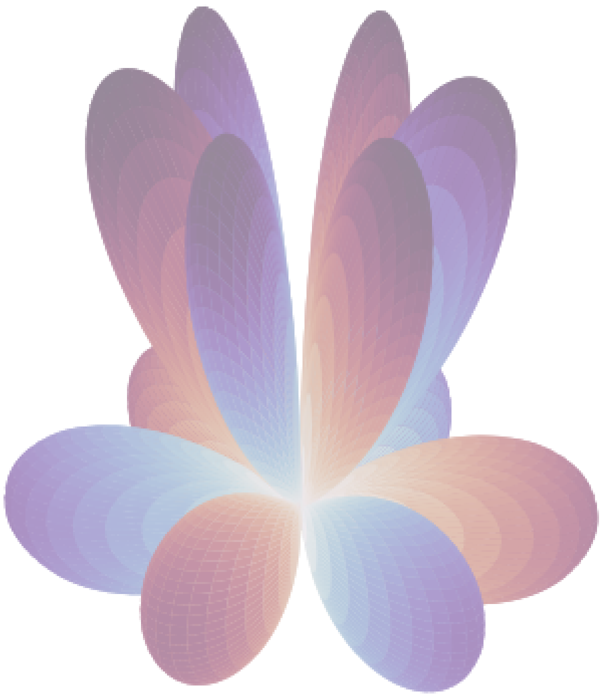

*Supervisor:*
Marion Pillas
*Co-supervisor:*
Jean-René Cudell

*Academic Year 2025–2026*

# Abstract

This master thesis investigates the gravitational wave memory effect, a prediction of general relativity, characterized by a permanent displacement in spacetime geometry. While this effect remains undetected, next-generation detectors such as the Einstein Telescope (ET) and the Laser Interferometer Space Antenna (LISA) are poised to enable its first observation. This work focuses on modeling and estimating the nonlinear & linear memory effect generated by neutron star mergers. By assessing its detectability across both instruments, I demonstrate that a memory signal in ET would be resolvable for an event analogous to the landmark multi-messenger discovery of August 17, 2017. Furthermore, a dedicated analysis of the memory effect from gamma-ray bursts shows that detection with ET and LISA is achievable in principle, yet sensitive to the modeling and requires a combination of several extreme physical characteristics.

# Acknowledgments

First of all, I would like to thank my thesis supervisors, M. Pillas and J.-R. Cudell, for their guidance, patience, and dedication throughout this year. Their (digital) door was always open whenever I had a question or ran into difficulty. Despite supervising her first master's thesis, M. Pillas demonstrated exceptional mentorship. I deeply appreciate her guidance and the valuable research opportunities she provided throughout this project. I would also like to extend my thanks to H. Inchauspé, who joined the project and generously shared his expertise on the LISA aspects of this work. This thesis would not have reached its current form and completeness without their collective support.

I would also like to thank the members of the reading committee: M. Pillas, J.-R. Cudell, M. Fays and G. Rauw. I wish them an enjoyable reading.

Finally, I would also like to extend my thanks to Noah Jamsin for the many discussions we shared about our respective theses, which, I hope, did not contribute further to the loss of sanity that such work inevitably entails.

# Contents

To aid in readability and prevent any potential confusion, the table below provides a comprehensive list of all abbreviations employed in this thesis, along with their corresponding definitions.

| Abbreviation | Meaning |
|---|---|
| GW | Gravitational Wave |
| GR | General Relativity |
| TT | Transverse-Traceless (gauge) |
| CBC | Compact Binary Coalescence |
| GRB | Gamma Ray Burst |
| ET | Einstein Telescope |
| CE | Cosmic Explorer |
| LISA | Laser Interferometer Space Antenna |
| LIGO | Laser Interferometer Gravitational-Wave Observatory |
| SNR | Signal-to-Noise-Ratio |
| EM | Electromagnetic |
| NS | Neutron Star |
| BH | Black Hole |
| BNS | Binary Neutron Stars |
| BBH | Binary Black Hole |
| NSBH | Neutron Star Black Hole |
| HMNS | Hypermassive Neutron Star |
| SMNS | Supramassive Neutron Star |
| TOV | Tolman-Oppenheimer-Volkoff |
| EFE | Einstein Field Equations |
| NR | Numerical Relativity |
| EOB | Effective-one-body |
| FT | Fourier Transform |
| DFT | Discrete Fourier Transform |
| FFT | Fast Fourier Transform |
| QMC | Quasi-Monte Carlo |

# Introduction

*"If you ask me whether there are gravitational waves or not, I must answer that I do not know. But it is a highly interesting problem."*

A. Einstein

The historic detection of the first gravitational wave [1] (GW) GW150914 provided validation of Einstein's theory of general relativity [2] (GR) and marked the beginning of GW astronomy. Subsequent detections have continued to test GR and so far all observations remain consistent with its predictions [3, 4]. Nevertheless, some aspects of GW physics have yet to be probed experimentally. One such prediction is the memory effect. This phenomenon corresponds to a non-oscillatory component of the GW signal that produces a permanent change in the relative separation of two freely falling test masses after the passage of the wave [5]. Detecting this effect would therefore constitute an important test of GR and of the structure of spacetime.

Compact binary coalescences (CBCs), the merger of two compact bodies, are the sole class of GW sources detected to date. Their waveforms are expected to carry an imprint of the memory effect which clearly differs from the typical evolution of these signals. In essence, a GW produced by a CBC without memory can be described as an oscillatory signal whose frequency and amplitude increase as the two compact objects (a combination of neutron stars or black holes) spiral closer together and peaks at the merger. Immediately after the merger, the signal transitions to a post-merger phase characterized by a ringdown of the remnant (a black hole or a neutron star) that emits GWs before settling down into a stable configuration where the signal returns to zero at late times. However, this description is incomplete as it does not include the memory effect. The GW amplitude of a source with memory does not damp to zero at late times. This translates into the lasting distortion of spacetime in the path of the GW [5]. An example of a CBC signal with and without memory is illustrated in Fig. 1.

Although this phenomenon has been known theoretically since the 1970s [6], its full implications for GW physics and astrophysics remain under active investigation. The possibility of detecting the memory effect with the next generation of GW telescopes has sparked renewed interest in this theoretical prediction, as it has the potential to provide a new approach to probing high-energy astrophysical sources. To provide a clear description of the memory effect in neutron star (NS) mergers, the introduction is organized into several sections. First, this work distinguishes the two regimes of the memory effect: linear and nonlinear memory.

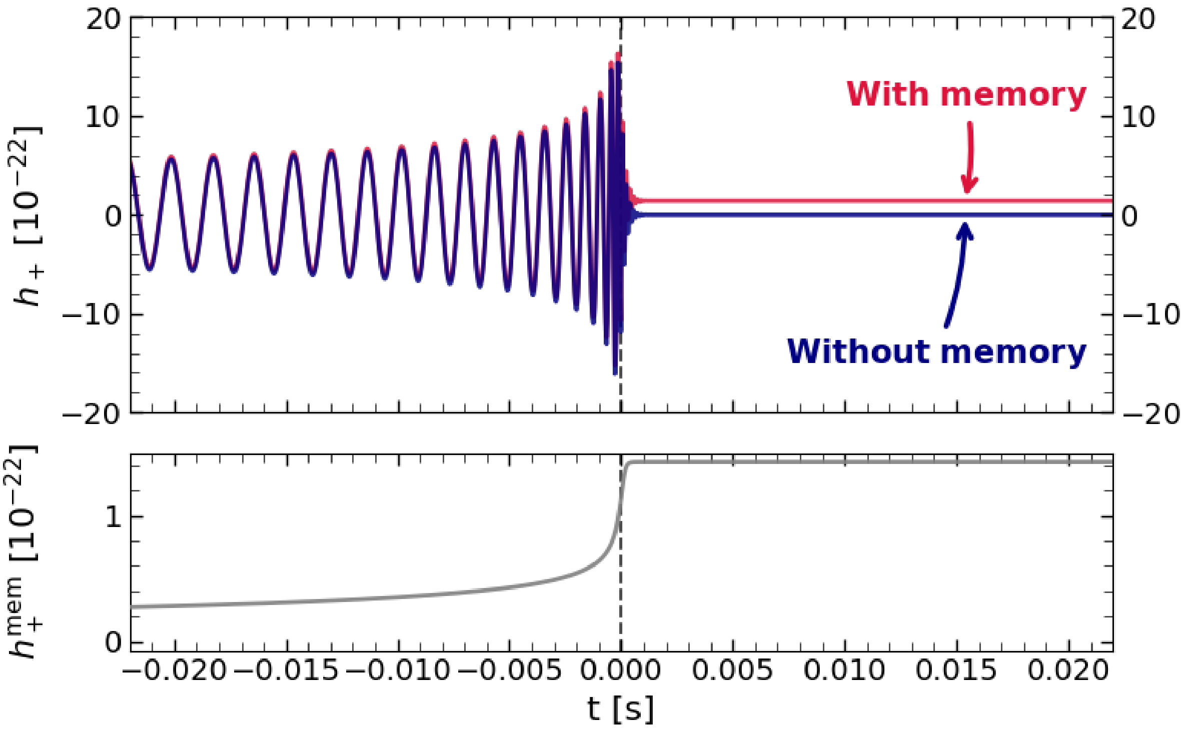


Figure 1: GW signal without (blue) and with (red) memory, where the memory component is displayed in the bottom axis. The dotted vertical line denotes the merger time. The GW strain and nonlinear memory were computed using the SEOBNRv4 approximant from `PyCBC` [7] and `GWMemory` [8] Python libraries, respectively, for two equal mass, non-spinning BNs with a total mass of $3M_\odot$ at a distance of 100 Mpc observed edge-on.

Subsequently, the question of the detectability of the memory effect will be addressed in the context of GW astronomy. After describing the principles and current performance of current GW detectors, the discussion will lead to an explanation of why present-day detectors are poorly adapted to capture the memory effect produced by a single event.

Finally, the role of GW memory will be considered in the broader context of multi-messenger astrophysics. Binary neutron star (BNS) mergers constitute promising systems in this regard, as they should emit both GW and electromagnetic (EM) radiation. The EM counterparts include a kilonova emission as well as a gamma-ray burst (GRB) with an afterglow. The kilonova emission is itself powered by different ejecta components, notably the dynamical ejecta expelled during the merger and the disk wind ejecta launched from the remnant accretion disk. If these outflows are anisotropic, they can generate a contribution to the linear memory. In addition to the nonlinear memory, these processes may therefore contribute to the total memory signal. Accounting for each contribution is important, as their combined effect determines the overall amplitude of the memory and consequently its detectability.

# The memory effect

Two distinct classes of memory exist. The first, the nonlinear memory, stems from the self-interaction of GWs, and was described earlier and illustrated in Fig. 1. This effect is embedded in every GW signal and has received extensive theoretical study. Moreover, a second memory class, the linear memory, originates from different physics: the anisotropic ejection of matter or radiation, independent of GW generation. While both types produce a permanent shift in spacetime, they differ in their origins and typical amplitudes. The following subsections detail each mechanism.

## Linear memory effect

The linear contribution to the memory effect originates from the linearized Einstein equations. This characteristic was discovered first in 1974 by Zel'dovich and Polnarev in their study of close encounter bodies [9]. However, it was not until 1985 that Braginski and Grishchuk [10] proposed the name "memory effect" to describe the permanent displacement. A general formula was developed by Braginsky and Thorne in 1987 [11], making it easier to describe the memory effect based on the initial and final states of $N$ unbound bodies with rest masses $M_A$ and velocities $v_A^i$. The net change on the metric $h$ after scattering is given by the following formula:

$$\Delta h_{ij}^{\mathrm{TT}} = \frac{4}{r}\Delta\left[\sum_{A=1}^{N}\frac{M_A}{\sqrt{1-v_A^2}}\left(\frac{v_A^i v_A^j}{1-v_A\cos(\theta_A)}\right)\right]^{\mathrm{TT}} \tag{1}$$

where $r$ denotes the observer-source (luminosity) distance, $\theta_A$ is the angle between $\vec{v}_A$ and the observer's line of sight, and the operator $\Delta$ preceding the summation indicates the difference between the sum evaluated for outgoing particles and incoming particles.

This formula is expressed in the Transverse-Traceless (TT) gauge, the standard coordinate system for GW's interpretation with the correct number of physical polarizations. Let's also emphasize that this formula is nonzero for unbound masses in their initial or final states (or both) ejected *anisotropically.* The angular dependence will be examined in detail in a dedicated section, as it behavior differs according to whether the source is relativistic or not. In short, for non-relativistic sources, linear memory is maximized when the source is viewed edge-on ($\theta = \pi/2$, where $\theta$ denotes the angle between the direction of the source emission and the line of sight). For ultra-relativistic sources, the memory instead is maximum in quasi face-on configuration ($\theta = 0$).

The linear memory includes a range of GW sources, such as binary systems whose components are disrupted (or any mass loss), asymmetric supernova explosions with their neutron star kick [12], hyperbolic trajectories of massive objects [13], and GRB jets [14]. The linear memory effects caused by these phenomena is labeled as *ordinary* memory. The latter depends on physical properties of the ejecta, such as its mass, velocity or released energy. To give an idea of the scale, the amplitude of the ordinary memory effect is generally small, typically at least three orders of magnitude lower than the peak oscillatory GW signal. Later in this work, we will investigate cases in which linear memory becomes a non-negligible factor.

## Nonlinear memory effect

A nonlinear form of memory was discovered independently in the 1990s by Blanchet & Damour [15] (in the context of Post-Minkowskian theory[1]) and Christodoulou [16] in a rigorous mathematical formalism. This effect, also known as the Christodoulou effect, exemplifies a nonlinearity behavior in GR: GWs act as their own source of gravity. In the linear approximation of Einstein's equations, GWs propagate without affecting spacetime. However, once nonlinearity is included, the stress-energy tensor of the GWs themselves becomes a source term in Einstein's equations. This creates a self-interaction mechanism. As GWs propagate, their energy and momentum curve spacetime, which in turn affects how the waves themselves evolve. The nonlinear feedback produces the permanent offset known as the nonlinear memory effect.

A different picture has been mentioned by Thorne [17] where he describes the nonlinear memory as an extension of the linear case. A GW burst will emit a large quantity of graviton particles, where each graviton can be the source of a GW. Recent work by Bieri *et al.* [18] has demonstrated that EM radiation and neutrinos also produce a nonlinear memory effect. They treated these radiations as massless particles and named the resulting effect *null* memory. Using this terminology, the nonlinear memory produced by GWs is also a type of null memory, as it arises from the null radiation of GWs traveling at light speed. To review all types of effects and their sources, a summary table is provided in Table 1.

Table 1: Classification of memory effects by order and terminology. Sources marked with ($\star$) are studied in this work.

| Order | Terminology | Source type | Example sources |
|---|---|---|---|
| Linear | Ordinary | Non-null (massive) baryonic matter | $\star$ Mass loss in binary disruptions<br>$\star$ GRB jets (point-particle approx)<br>• Hyperbolic encounters of massive objects<br>• Asymmetric supernova explosions |
| Nonlinear | EM null | EM radiation | $\star$ Kilonova |
| | Neutrino null | Neutrino radiation | • Supernova neutrino burst |
| | GW null | Gravitational waves | $\star$ CBC mergers |

[1]In 1992, Blanchet & Damour demonstrated that the gravitational memory effect can also be derived using a perturbative approach to GR, by expanding the metric as a series in powers of Newton's gravitational constant $G$. This led to the development of the Post-Minkowskian perturbative formulation of gravity. Within this context, gravitational memory is recognized as part of a broader class of heredity effects. They also revealed new phenomena such as the tail effect, characterized by a slow, power-law decay of the waveform at late times.

The expression of the null memory reads:

$$\delta h_{ij}^{\mathrm{TT}} = \frac{4}{r}\int_{-\infty}^{t_r} dt' \left[\iint \frac{dE}{dt'd\Omega'}\frac{n_i'n_j'}{(1-\mathbf{n}'.\mathbf{N})}d\Omega'\right]^{\mathrm{TT}} \tag{2}$$

with $t_r = t - r/c$ the retarded time, $\frac{dE}{dt'd\Omega'}$ the energy flux per unit time and solid angle in the radial direction $n_i$ and $\mathbf{N}$ a unit vector from the source to the detector. We recover the same equation in the case of linear memory Eq. (1) by interpreting that each graviton has an energy $E_A = M_A/\sqrt{1-v_A^2}$ and a velocity $v_A^i = cn_A^i$ [17]. Here, the index $A$ labels individual gravitons and $n_A^i$ denotes the direction unit vector of the graviton's motion, and $c$ is the speed of light in vacuum.

Compared to the ordinary memory, the ratio of the CBC waveform to the the null GW memory amplitude is of the order of 10% [19]. Table 2 contains maximum amplitude values for the oscillating signal $h_{\mathrm{osc}}$ (without memory) and the memory component $h_{\mathrm{mem}}$ for various distances and total masses. The waveform and the memory have been computed with the approximant SEOBNRv4[2] for an equal mass system observed edge-on. The approximant was obtained using the `PyCBC` package [7], a Python package used to generate and manipulate GW waveforms and data.

Table 2: Maximum amplitudes of the oscillatory waveform ($h_{\mathrm{osc}}$) and the nonlinear memory effect ($h_{\mathrm{mem}}$)

| | | Max amplitude | |
|---|---|---|---|
| $M_{\mathrm{tot}}$ ($\mathrm{M}_\odot$) | Distance (Mpc) | $h_{\mathrm{osc}}$ | $h_{\mathrm{mem}}$ |
| 10 | 100 | $5.75\times10^{-22}$ | $5.67\times10^{-23}$ |
| 100 | 100 | $5.86\times10^{-21}$ | $6.45\times10^{-22}$ |

The nonlinear memory effect is of particular interest for several reasons. The memory is maximal for edge-on systems, such as the GW. Hence, a configuration suitable for detecting GWs is also suitable for its memory effect. The hereditary nature of the memory effect can also be observed in the integration of energy flux during inspiral, merger and post-merger times (by definition $\delta h_{\mathrm{nonlinear}}^{\mathrm{TT}} \propto E^{\mathrm{GW}}$). The buildup of the nonlinear memory concentrates during the final inspiral and merger phases, producing a step-function shape that saturates post-merger. Because the nonlinear memory amplitude depends directly on the GW energy, it carries information about the binary parameters, complementary to the oscillatory. The memory effect thus provides an additional means to prove the intrinsic properties of the source.

Furthermore, the origin of the Christodoulou effect is linked to the nonlinear part of GR. Such an observation would enable to experimentally test this theory of gravity in a new regime or apply new constrains in modified gravity theories [20]. As mentioned by Favata [21], the detection of the nonlinear memory would allow a direct probe of "the ability of gravity to gravitate".

[2]An approximant is an analytical template that models the GW emitted by a CBC as a function of the system's parameters (mass, distance, inclination, . . . ), enabling for parameter inference by comparing approximant predictions to data. SEOBNRv4 is a specific waveform approximant within the effective-one-body (EOB) framework which describes the full coalescence (more details in 1.5.3).

Finally, it is worth mentioning that the nonlinear memory effect is related to soft theorems in scattering theory and BMS (Bondi-Metzner-Sachs) supertranslations [22]. In BMS groups, the universe is assumed to be asymptotically flat[3], and admit numerous possible vacua. Each initial and final state (early and late times) is linked by supertranslations, a type of gauge symmetry. In the description of quantum field theories, these vacuum variations are caused by the emission or absorption of soft gravitons. The same treatment can be applied to the GW point of view. When a GW passes through, it can cause the vacuum to change from one state to another, which is physically translated into a memory effect signature [22]. Conversely, the detection of the memory effect would confirm a transition between different BMS vacua connected by a supertranslation, whose quantum counterpart is the emission of soft gravitons. In this context, the memory signature would provide an indirect detection of soft gravitons.

# GW astronomy

To understand why such a property has not been detected, it is worthwhile to understand the nature of GWs. Unlike classical EM waves, GWs are produced by accelerating, asymmetric mass distributions characterized by changing quadrupole[4] moments. These waves propagate by distorting the fabric of spacetime itself, meaning only highly energetic events can produce the perturbations[5] necessary for detection. Consequently, CBCs are not the sole sources of GWs. It is also expected that non-spherical supernova explosions or bumped pulsars can generate detectable GWs. The GWs produced travel at light speed and the manifold of space-time will undergo periodic stretching and compression, dictated by a combination of two independent polarizations: the plus polarization ($h_+$) and the cross ($h_\times$) polarization. As a consequence, GWs can distort space-time along both of these polarization modes as represented in Fig. 2.

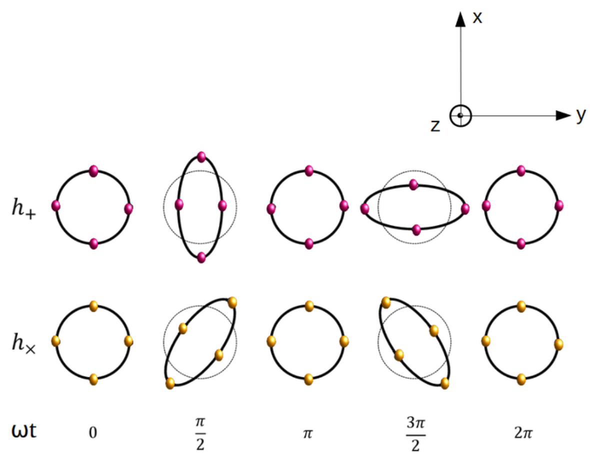


Figure 2: Illustration taken from [24] of the effect produced by the 2 possible polarizations $h_+$ and $h_\times$ of a GW in the $z = 0$ plan. The $h_+$ polarization induces a contraction along the $y$ axis and an elongation along the $x$ axis, and the opposite half a period later. The effect of $h_\times$ is analogous to a rotation of 45°.

[3] i.e. far from any source, spacetime is similar to a flat Minkowski space.

[4] A dipole formulation of GWs is impossible given the conservation of momentum. Therefore, the nature of GWs must be quadrupolar (at the lowest order).

[5] A classical derivation of the Young modulus of the fabric of space-time $Y_{\text{spacetime}}$ at 100 Hz, presented in [23], give an estimation by a dimensional analysis: $Y_{\text{spacetime}}(f = 100\text{ Hz}) \simeq 4.5 \times 10^{31}\text{Pa} \simeq 10^{20}\ Y_{\text{steel}}$.

It is based on these specific features of GWs that ground-based detectors such as LIGO (Laser Interferometer Gravitational-Wave Observatory) in Livingston and Hanford, Virgo and KAGRA [25] have been built to later form the LVK collaboration [26]. The core design of these detectors is a highly complex and advanced Michelson interferometer with a remarkable sensitivity. The detectors are L-shaped, with two perpendicular arms of equal length, of the order of kilometers. A powerful, frequency-stabilized laser is split at a central beam splitter, sending IR light down both arms. At the ends of each arm, massive mirrors of 40 kg in the case of LIGO[27] (acting as test masses in "free-fall") reflect the beams back, where they are recombined to produce an interference pattern. In the absence of a GW, the beams interfere destructively, and no light reaches the photodetector. When a GW passes, it causes a differential change in the arm lengths (of the order of $10^{-19}$m) resulting in a tiny but measurable change in the interference pattern. However, a conventional interferometer would not be able to detect the small variations in the interference pattern produced by the wave. To solve this problem, different features had to be implemented in the construction of the detectors in order to achieve record sensitivity.

Firstly, the longer the arms, the larger the deformation and consequently the longer the wavelength probed. We can relate the relative amplitude of the stretching of the arms (length $L_0$ at rest) via the dimensionless strain $h$ that is measured in GW interferometers:

$$h = \frac{\Delta L}{L_0} \tag{3}$$

To overcome the practical limitations of building even longer arms, LIGO incorporates Fabry-Perot cavities in each 4 km arm. This is achieved by placing an additional mirror near the beam splitter in each arm, creating a cavity where the laser bounces back and forth about three hundred times before recombining [28]. This increases the effective path length, amplifying the phase shift caused by GWs and making the instrument far more sensitive [29]. LIGO also uses power recycling mirrors to boost the circulating laser power inside the interferometer. This higher photon flux sharpens the interference fringes, improving the detector's ability to resolve extremely small variations in arm length [29]. Signal recycling mirrors are another key feature, allowing to tune its sensitivity across different frequency bands [30]. This flexibility enables the detector to optimize its response for various types of GW sources [29, 30]. Finally, mirrors are suspended by multi-stage pendulum systems and isolated from seismic and thermal noise by advanced vibration isolation platforms [29].

As a result, the first-generation LIGO detectors had a sensitivity of $2 \times 10^{-23}/\sqrt{\mathrm{Hz}}$ at 200 Hz, and technological advances have increased sensitivity to $8 \times 10^{-24}/\sqrt{\mathrm{Hz}}$ for the second generation detectors back in 2015 [28]. This increased sensitivity is the cornerstone that enabled the detection of GW150914 during the first observing run O1 (September 12, 2015 to January 19, 2016), over which two more BBH CBCs with masses over $5\,M_\odot$ were detected. The second observing run O2 (November 30, 2016 to August 25, 2017) made 8 detections, 7 BBHs and the last was the first BNS detection: GW170817. The addition of Virgo in Italy (operational since 2007, with its upgrade Advanced Virgo [31] in 2017) at the end of the O2 run had strengthened the global network for GW detection enabling such observations. The sensitivity of these detectors is illustrated in grey in Fig. 3.

For our later purposes, we shall now focus on the first BNS detection. GW170817 marked a milestone in GW astronomy as it corresponds to the first and unique event (to

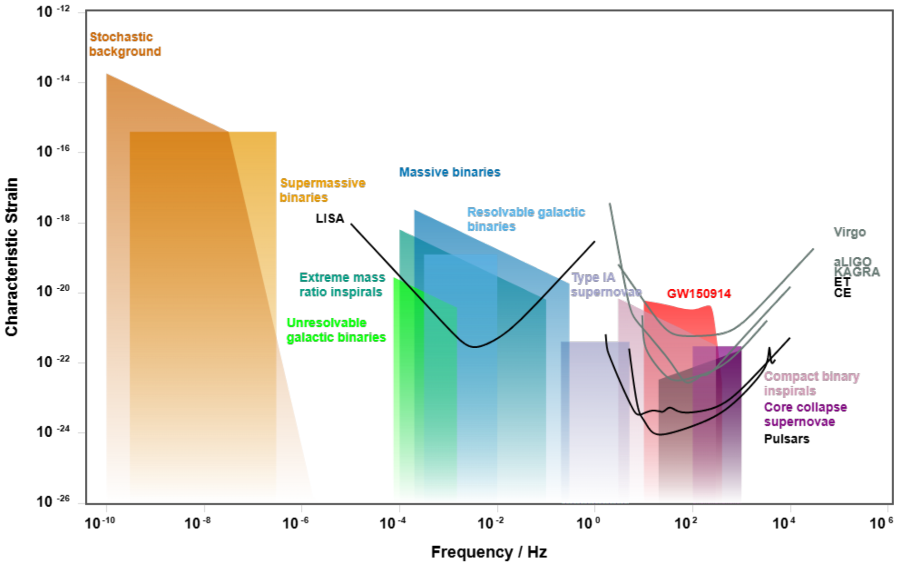


Figure 3: Sensitivity curves for current (grey) and next generation (black) GW detectors. LISA covers low frequencies ($10^{-4}$ to $10^{-1}$Hz), adapted for the detection of memory from supermassive and prompt mergers. ET and CE have an optimal frequency band slightly below 100Hz and an increased sensitivity needed to measure the two orders of magnitude smaller amplitude of the memory compared to the main signal. Solid surfaces refer to detectable sources. Credit: http://gwplotter.com / S. Rao et al. / K. Oide, G. Franchetti & F. Zimmermann / P. Chen.

date) for which an EM counterpart was observed [32]. Shortly after the GW signal was detected, a short GRB (GRB 170817A) was independently observed, followed by a wide range of EM observations across the spectrum attributed in particular to a kilonova and an afterglow emission. This made GW170817 the first confirmed case of multi-messenger astronomy combining GW and EM radiation. Further details regarding to this event will be discussed in the dedicated section about multi-messenger astrophysics.

The observation campaign following O2, O3 (April 1, 2019 to March 27, 2020) [33], considerably expanded the catalog of GW detections. Among its 90 candidates, it included the second BNS detection, namely GW190425 [34], as well as the first two confident mergers of neutron stars and black holes (NSHB) [35], the remainder being BBHs. The most recent run, O4 (May 24, 2023 to November 18, 2025), is the most prolific to date in terms of confirmed detections with its sensitivity of $2 \times 10^{-24}/\sqrt{\text{Hz}}$ [36]. Comprehensive analysis of its first segment O4a alone yielded 128 candidates [37], while the total number of signals detected across the full O4 run (O4a, O4b, O4c) is still being processed.

Having more active detectors is a powerful asset for GW detection. If a plus polarized wave arrives at exactly 45° to one of the arms, the movement of the two arms will be perfectly identical, resulting in no detection. By deploying a network of detectors with different orientations across the planet, this risk is reduced. Furthermore, locating the source is a major concern for GW astronomy. A single GW detector cannot provide precise information on the location of a source, even if a detection is made. In the case of GW170817, the combination of signals from LIGO detectors alone yielded an initial location region of about 190 deg$^2$. However, when the Virgo detector's data was added, triangulation across all three detectors allowed the location to be dramatically improved to 31 deg$^2$ at 90% confidence [32] as illustrated by the dark green region in Fig. 4.

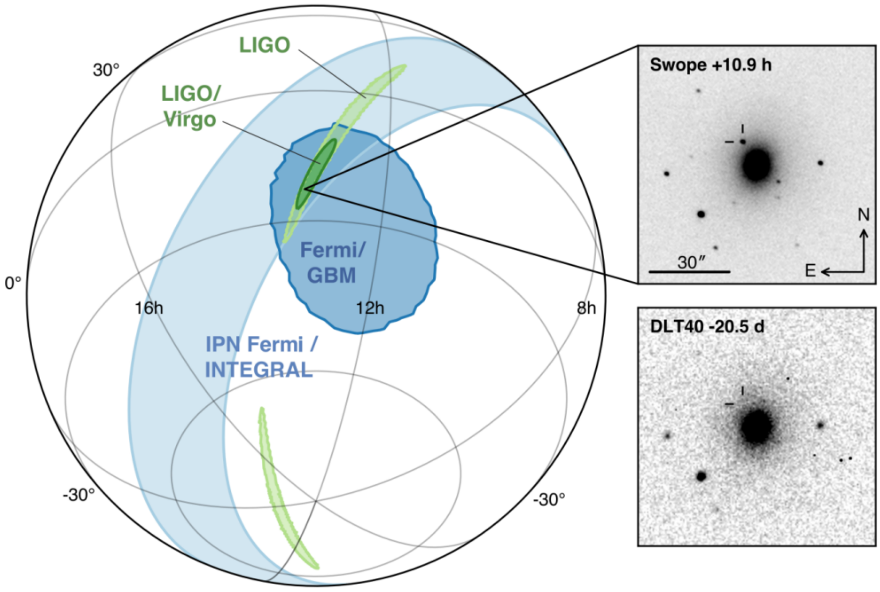


Figure 4: Location of GW170817/GRB 170817A in GW, gamma-ray, and optical data. The 90% confident region of detection from LIGO (190 deg$^2$) and the LIGO-Virgo (31 deg$^2$) are marked in green and dark green as well as the ones of Fermi-Integral and Fermi-GMB in blue and dark blue respectively. The inset displays NGC 4993, the apparent host, in Swope and DLT40 images (after and before the kilonova emission respectively), with the transient marked by a reticle. Image taken from [32].

# Memory effect detectability

No memory effect has been detected yet. This can be explained by reasons related to how GWs are detected with current detectors[6]. To begin, the detector test-masses are not truly free [5]. The instruments are mechanically returned to their equilibrium positions after each event, which erases the measurement of the memory effect. Moreover, current high-frequency detectors remain insensitive to the memory signal because of two constraints. First, the inverse of the rise time duration of the memory effect determines the optimal frequency band for its detection, requiring detectors whose sensitivity spans the characteristic frequency corresponding to each source class [38]. Various sources and their associated frequency ranges will be discussed in detail later in this work. For instance, LIGO, which achieves its best sensitivity around 100 Hz, can in principle detect events with short ejection timescales of approximately 0.01 seconds. However, sources producing longer-duration ejecta will generate characteristic frequencies below LIGO's sensitivity band, rendering the detector insensitive to their memory signatures. Second, even within an overlapping frequency band, the detector's sensitivity must be sufficiently low to resolve the memory amplitude, a condition that current detectors fail to meet. The advanced LIGO configuration, for instance, achieves its best strain sensitivity of $10^{-22}$ around 100 Hz, whereas the memory amplitude from an optimistic detection of a $10M_\odot$ CBC system at 100 Mpc is estimated at $10^{-23}$ in the same frequency range. A last reason is simply the fact that the memory strain will be easily masked by low-frequency noise in ground-based detectors like LIGO and Virgo [38]. Distinguishing this slow "ramp-up" signal from instrument and environmental noise requires enhanced sensitivity in low frequency bands [38].

[6]For the following, it would be helpful to have Fig. 3 in mind regarding the detectability of the memory effect for each detector.

An optimal strategy to detect the memory was first proposed by Braginsky and Thorne [11] and consists in the integration of the signal over a time $\tau \equiv 1/f_{\mathrm{opt}}$ where $f_{\mathrm{opt}}$ is the optimal frequency of the detector. It yields a memory sensitivity equivalent to an ordinary burst at the detector's optimal frequency if the memory jump is quicker than the detector's response $\tau$. Nevertheless, most detector data are high-passed for low-frequency noise, which removes information about the total memory offset. While the detection of memory from individual events remains out of reach, a possible approach is to stack a large number of observations to improve signal-to-noise ratio (SNR) [38]. However, the lack of CBC data with high SNR currently prevents substantial results [38].

Next-generation ground-based facilities, such as the Einstein Telescope (ET) [39], and space-based detectors as the Laser Interferometer Space Antenna (LISA) [40], are expected to achieve the sensitivity and bandwidth required for an observation of GW memory from individual astrophysical sources. An artist's impression of these two detectors is given in Fig. 5. ET configuration is more focused on a better sensitivity at $10^1$ to $10^2$ Hz while LISA will reach a characteristic strain sensitivity around $10^{-20}$ for lower frequencies between $10^{-4}$ Hz and $10^{-1}$ Hz.

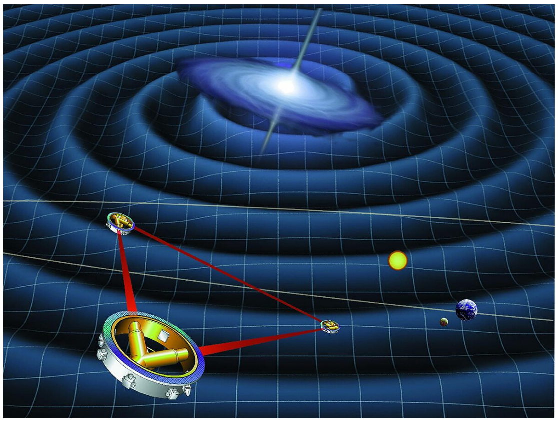

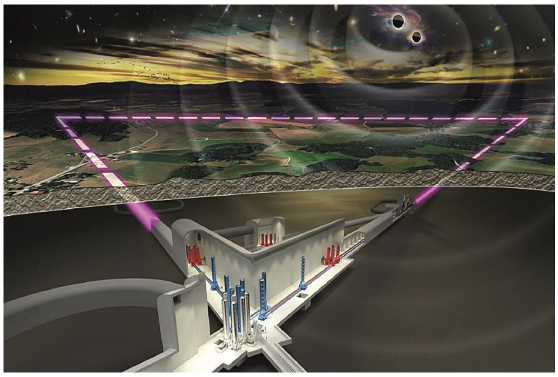

Figure 5: *Left*: Sketch of LISA detecting GWs from [41]. *Right*: Illustration from [42] of the underground detector ET, also with three 10 km long arms to cover more incident GW configuration.

ET's main solution for reducing low-frequency noise is to build the detector underground. Parasitic sources such as human and natural activity will be more easily contained. An even more radical solution for reducing seismic noise is to place the detector in space. In 2035, the LISA project plans to send three spacecraft at L1 forming an equilateral triangle with arms of 2.5 million km. LISA would be the first space-based GW detector to characterize low-frequency sources such as CBCs from massive BHs or yet unknown sources. In the case of the memory effect, LISA is expected to detect the memory effects of 300 massive sources per year [43], long before they merge. ET, with its intermediate band and high sensitivity, is well-placed to observe memory from more compact events. Fig. 3 combines the sensitivity curves of these detectors (black lines) and the associated detectable sources. Derived from simulations, ET would have detection rates of $10^6$ BBH and $7 \times 10^4$ BNS events per year [44].

# CBCs in the context of multi-messenger astrophysics

In this work, we focus on astrophysical sources that exhibit memory effects arising from multiple emission mechanisms. To maximize the wealth of information accessible through memory effects, we must identify which CBCs produce the richest variety of emission signatures.

Among the compact binary mergers detected, three main classes of sources have been identified: binary black holes (BBH), binary neutron stars (BNS), and neutron star-black hole (NSBH) systems. BBH mergers constitute the majority of observed events but are not expected to produce EM counterparts, limiting the multi-messenger information available. Conversely, mergers involving at least one neutron star, BNS and NSBH systems, can eject neutron-rich material during coalescence, leading to its radioactive decay in the form of a kilonova. Among these, BNS mergers emerge as the optimal candidates for studying memory effects through multiple emission channels. They produce both GW and EM radiation, while exhibiting post-merger dynamics expecting to also produce memory effects.

In BNS mergers, the post-merger remnant and its associated ejecta are determined by the total mass $M_{\rm tot}$ compared to the Tolman-Oppenheimer-Volkoff (TOV) mass[7] $M_{\rm TOV}$, the maximum mass that a non-rotating neutron star can support against gravitational collapse. For $M_{\rm tot} \gtrsim M_{\rm th} \simeq 1.3$ to $1.6\,M_{\rm TOV}$, with $M_{\rm th}$ the threshold mass for prompt collapse, the merger promptly forms a black hole [47]. For intermediate total masses, $1.2\,M_{\rm TOV} \lesssim M_{\rm tot} \lesssim M_{\rm th}$, the merger produces a hypermassive neutron star (HMNS), a differentially rotating remnant temporarily supported against collapse [47]. If $M_{\rm tot}$ lies between $M_{\rm TOV}$ and $1.2\,M_{\rm TOV}$, the remnant can be a supramassive neutron star (SMNS) supported by rapid rotation and collapsing into a BH only after sufficient angular momentum loss [47]. Each configuration reflects a different morphology of its ejecta and, consequently, in its memory signatures, as we will see in the following sections.

In essence, CBCs that are BNS mergers are particularly compelling for our study because they could present multiple distinct sources for memory effects. GW170817 stands as the sole example of a BNS merger detected through both GWs and EM radiation, also associated with GRB 170817A and a kilonova counterpart AT2017gfo. The last part of this introduction is devoted to providing a general explanation of each of the detected ejecta.

## Kilonova & AT2017gfo

A kilonova is the transient EM emission, from UV to NIR, that follows the merger of two NSs or a NS and a BH. The term kilo-nova refers to the typical peak luminosity being 1000 times brighter than a nova (and 1 to 10% that of a supernova) [47]. These mergers eject neutron-rich material into space at high velocity. Such ejecta are characterized by a high neutron density environment, originated from the progenitor(s), in which the timescale for neutron capture is shorter than the beta-decay lifetime. It implies that a kilonova is evidence for the creation of heavy elements, including lanthanides and actinides (gold, platinum, ...) produced by a rapid neutron capture process, commonly known as r-process [47, 48]. Such events have long been assumed to be a source of galac-

[7] The TOV mass is estimated to lie in the range $2.01 M_\odot$ to $2.16 M_\odot$ [45]. This interval reflects remaining uncertainties in the NS equation of state, although recent GW observations have narrowed the allowed range of models [45, 46].

tic heavy elements, and the current knowledge of kilonovae tends to fully confirm this [48].

Although the kilonova concept has been theoretically developed since the early 1990s, it was only after the historic joint detection of GWs with GW170817 and broad EM emission in 2017 that the observational evidence became indisputable [47]. Near the end of the second observing run (02), a close GW detection was detected by both LIGO and Virgo interferometers. The parameters of GW170817 used throughout this work are summarized in Table 3.

Table 3: Parameters of GW170817 for a low-spin prior [1, 49]

| Parameter | Value |
|---|---|
| Primary mass $m_1$ | $[1.36,\ 1.60]\ M_\odot$ |
| Secondary mass $m_2$ | $[1.17,\ 1.36]\ M_\odot$ |
| Luminosity distance | $40^{+8}_{-14}$ Mpc |
| Viewing angle $\theta$ | $32^{+10}_{-13}$ deg |

**Note:** The ranges of values are for 90% posterior probability intervals.

However, even with multiple detectors, the typical location area for this event remained large enough (31 degree$^2$ then refined to 28 degree$^2$ with data analysis [32]) to make it still challenging to pinpoint the exact origin. This triggered a rapid search for a EM counterpart in this region. Just 1.74s after the GW event, the Fermi and INTEGRAL satellites detected a prompt and short gamma-ray burst: GRB 170817A. Eleven hours later, the first optical counterpart, AT2017gfo, was reported. In the following weeks, multiple telescopes observed the evolving emission in ultraviolet, optical, and near-infrared wavelengths [47]. These EM observations revealed a kilonova and its afterglow enabled to pinpoint the source on the outskirts of galaxy NGC 4993 (as already illustrated in Fig. 4). This first and only multiple detections gave rise to a new era of multi-messenger astronomy, combining information from GW and EM messengers.

Such an observation enabled to construct the lightcurve of the kilonova, represented in Fig. 6. The temporal evolution of luminosity is dictated by the initial heating by radioactivity, followed by the emission of photons from the expending and cooling layers of matter. Originally, the lightcurve rises through the prompt expansion of the ejecta heated by the radioactive decay of newly synthesized heavy elements (through the r-process). The high temperature creates a strong luminosity that increases rapidly. The lightcurve peaks at the moment when density and temperature drop sufficiently for photons trapped in expanding matter to escape at the time $t_{\text{peak}}$. This peak luminosity reflects the mass $M_{\text{ej}}$, velocity $v_{\text{ej}}$, opacity $\kappa$ of the ejecta. An estimate of the time at the peak luminosity in the lightcurve is given by [47] :

$$t_{\text{peak}} \approx 1.6\,\text{d} \left(\frac{M_{\text{ej}}}{10^{-2} M_\odot}\right)^{1/2} \left(\frac{v_{\text{ej}}}{0.1c}\right)^{-1/2} \left(\frac{\kappa}{1\,\text{cm}^2\,\text{g}^{-1}}\right)^{1/2}, \tag{4}$$

This relation predicts a peak in luminosity of several days for a range of value of lanthanide-free to lanthanide-rich opacity medium $\kappa \sim 0.5 - 30$ cm$^2$ g$^{-1}$ of the ejecta [47]. This is in line with the lightcurve associated with the detection of GW170817.

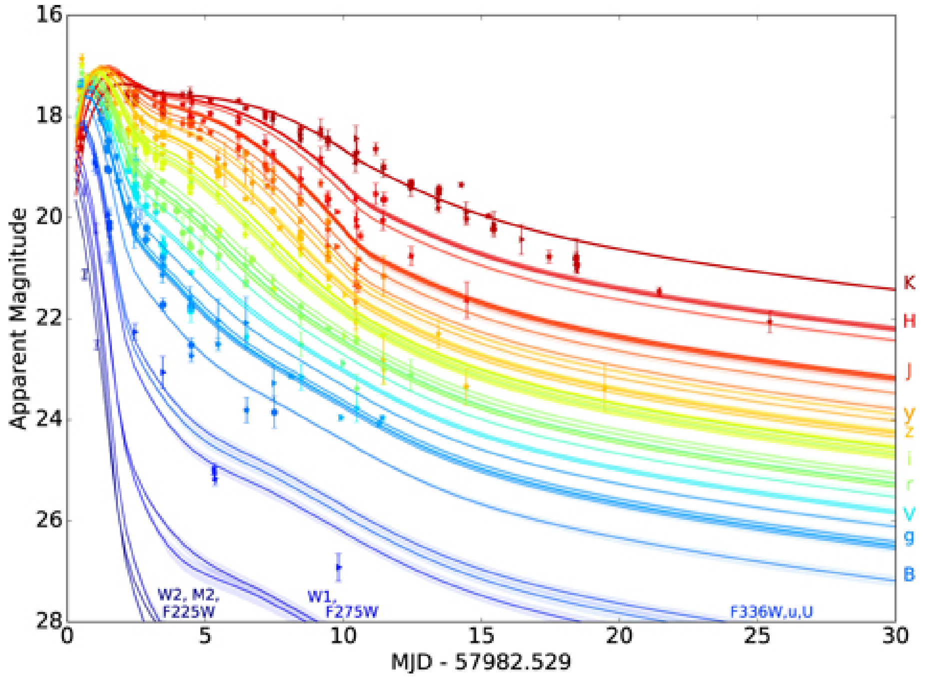


Figure 6: Lightcurves of the transient AT2017gfo measured from the UV (purple) to the NIR (red) obtained in [50].

## Dynamical ejecta

The dynamical ejecta refers to the matter produced during the merger phase through two distinct processes that occur on dynamical timescales. During the inspiral of BNS systems, NS matter is stripped and stretched by tidal forces, expanding outward primarily in the equatorial plane due to angular momentum transport by hydrodynamics processes. The second process involves material at the contact interface between the merging NSs which is squeezed out during the collision. This shocked material is primarily expelled in polar regions, on a timescale up to 10 ms after the merger [47, 48].

The relative importance of these two ejection mechanisms depends on several parameters. The NS equation of state (EOS) links mass and radius of a NS. Many different EOS models exist [51], each based on specific assumptions about composition, and each predicts a different mass–radius relation and ejecta outcome. The binary mass ratio $q$ also plays an important role, with more asymmetric systems ($q < 1$) typically ejecting larger amounts of mass [47]. The lighter NS is more strongly tidally disrupted during the inspiral, which can produce more neutron-rich ejecta. On the other hand, the formation of a remnant BH affects the total ejecta mass. In prompt collapse scenarios that characterize massive binaries, mass ejection from the contact interface is suppressed because of this region being rapidly swallowed by the newly formed black hole [47, 52]. The same situation occurs for NSBH.

For NS mergers, typical dynamical ejecta masses range from $10^{-4}$ to $10^{-2} M_{\odot}$, while NSBH mergers can eject up to $0.1 M_{\odot}$ if the NS undergoes complete tidal disruption [47]. This requires the BH to be low mass and/or rapidly spinning to allow the neutron star to be torn apart outside the innermost stable circular orbit. Depending on merger dynamics and mass ratios, the ejected material achieves velocities of 0.1 up to $0.3c$ [47].

Another property is the electron fraction $Y_e$ in the ejecta, defined from the proton densities $n_p$ and neutron densities $n_n$:

$$Y_e = \frac{n_p}{n_n + n_p} \tag{5}$$

The electron fraction $Y_e$ in the kilonova ejecta indicates whether the material is neutron-rich enough to synthesize heavy nuclei with mass numbers $A \gtrsim 90$ via the r-process. In practice, if $Y_e \lesssim 0.5$, the ejecta is sufficiently neutron-rich for the r-process to proceed efficiently and produce heavy elements [47]. Simulations accounting for weak interactions predict that $Y_e$ from the shock-interface ejecta could produce elements with $A$ between 90 and 130 thanks to r-process [47]. This lanthanide-poor ejecta emits in blue wavelengths mainly in the polar regions, giving rise to a blue kilonova as shown in panels (a) and (b) of Fig. 7. On the other hand, the tidally ejected matter distributed in the equatorial plane contains a lower $Y_e \lesssim 0.1$. Thus, the neutron-rich equatorial ejecta undergoes stronger r-process, producing heavy lanthanide elements. As these lanthanides create high opacity due to their numerous strong absorption lines in the short wavelength range, it leads the kilonova emission to appear redder and persist for approximately one week [47]. This tidal dynamical ejecta is observed as a red kilonova in Fig. 7.

## Disk wind outflow

In the case of a BNS merger, there is typically a large amount of debris that does not immediately fall into the central remnant. This neutron-rich matter, possessing enough angular momentum, circularizes into an accretion disk around the remnant. For NSBH mergers, a disk arises only if the NS is tidally disrupted before being swallowed by the BH. If disruption does not occur, almost no disk forms and little or no ejecta is produced. In both scenarios with disk formation, the disk can generate late-time (roughly a second after the merger [48]) outflow. As this disk evolves, several energy sources unbind part of its material and drive it outward. Within the first 100 ms after merger [53], intense neutrino emission from the hot remnant deposits energy in the disk and launches neutrino-driven winds [47, 48]. Viscous and magnetic stresses in the differentially rotating disk transport angular momentum outward, causing the disk to spread and heat up, so that some gas becomes gravitationally unbound and escapes as a thermally driven wind [47].

As a post-merger consequence, this ejecta will be located behind the dynamical ejecta and with a more isotropic distribution. The disk wind can be composed of neutron-rich or poor matter with velocities of the order of 0.05 c to 0.1 c and masses of $10^{-2}M_\odot$ to $10^{-1}M_\odot$ [47, 48]. The electron fraction in the wind ejecta will depend on the nature of the remnant[8] and the neutrino flux produced by the merger and hot environment [47].

If the merger undergoes a prompt collapse to a BH, the disk is relatively low mass and remains highly neutron-rich, so only a weak, quasi-isotropic disk wind is produced, and the resulting kilonova emission is dominated by red, lanthanide-rich ejecta [47]. This case is shown in panel (b) of Fig. 7.

If the remnant instead is a short-lived HMNS with a lifetime of tens to a few hundred milliseconds, neutrino flux interactions convert neutrons into protons and thus raise the electron fraction $Y_e$ in the surrounding disk, so the HMNS drives neutrino-powered winds that eject lanthanide-poor material along the poles, giving a blue kilonova component until the HMNS collapses to a BH, after which the remaining disk is a source of

[8] Which depends on the remnant mass and progenitor masses, as mentioned at the beginning of the section.

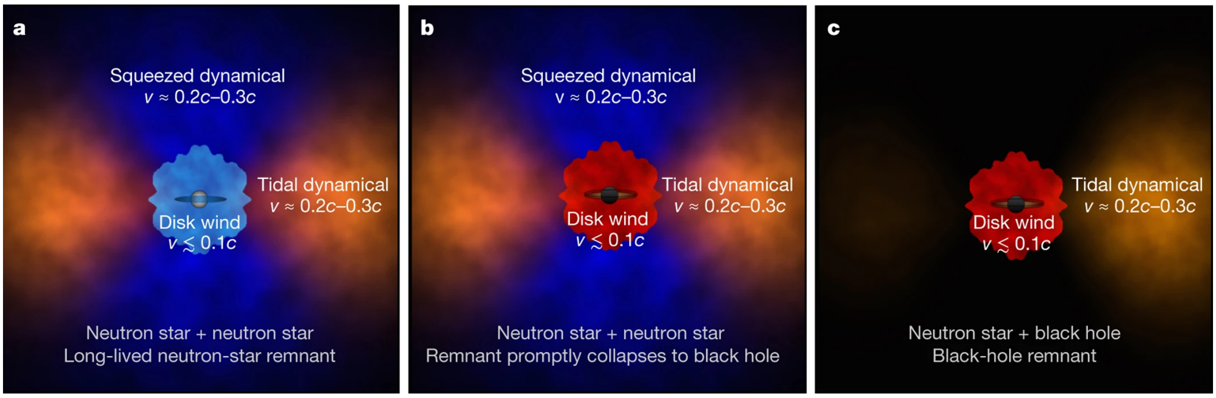


Figure 7: Red and blue emissions from different components of the ejected matter after a merger. The dynamical ejecta is composed of the equatorial tidal dynamical ejecta (orange) and the shock-heated ejecta (blue) in the polar regions. ***a***: If a long-lived NS results from the merger, the neutrino irradiation produced by the remnant creates a blue, lanthanide-poor wind ejecta. ***b***: If the remnant promptly collapses into a BH, the neutrino irradiation is suppressed and the wind ejecta is richer in neutrons, so appearing redder. ***c***: For the case of NSBH, the disruption of the NS produces a single tidal arm of ejecta, and the associated disk outflows are dominated by neutron-rich material, making the kilonova emission red. Illustrations from [48].

a more neutron-rich and redder outflow [47]. For a SMNS with that survives for more than 0.3 s, the same basic picture applies but with longer-lived, stronger neutrino irradiation and magnetic activity, so the polar blue ejecta are even more massive and energetic before the eventual collapse quenches the heating and leaves a late-time, redder disk wind. Such a blue-to-red evolution is compatible with a short-lived SMNS as suggested for GW170817[47, 48].

Finally, if the remnant is a stable and long-lived NS, it can act as a persistent magnetar-like central engine whose strong magnetic and neutrino-driven winds, possibly aided by a GRB jet, eject large amounts of high-$Y_e$, lanthanide-poor material along the rotation axis, boosting the blue disk-wind component of the kilonova [47]. Such a situation is illustrated in panel (a) of Fig. 7.

## Kilonova modeling

Because the morphology of a kilonova lightcurve is highly sensitive to the ejecta mass, velocity, opacity, composition and observing configuration, different models have been developed to reproduce lightcurves. By comparing such models to observations, one can directly study the effect of individual ejecta properties and thereby infer their values. A detailed modeling of the kilonova lightcurve can therefore be used to constrain the extrinsic parameters of the system that, in turn, shape the associated GW signal and its memory. For instance, simple models such as the one presented in [54] allow the population of kilonova counterparts to be constrained to GWs from BNS based on the peak magnitude in different bands and the observing angle. More complex models have also been developed, such as `Fiesta` [55], which generate kilonova lightcurves (and GRB afterglow). Building on this, the model can be coupled to GW measurements of the same merger, allowing joint analysis of the GW signal and EM counterpart to place tighter and more self-consistent constraints on the kilonova ejecta parameters. This multi-messenger study, applied specifically to BNS, is investigated in the master's thesis of Noah Jamsin, where messenger matching is used to reduce uncertainty. There are also ejecta models that take into account the morphologies of dynamical ejecta and disk wind [52]. This would be particularly useful for a more rigorous estimation of the linear memory effect.

## Gamma-ray burst

When two NSs merge, a very high-energy EM signature associated to a GRB can be observed. Although the physics of GRBs remains unclear, GRBs are believed to be powered by the conversion of the kinetic energy of highly relativistic outflows from compact central engines into radiation [56]. The fireball model provides a simple framework to model the GRB observations through two main phases. The first one is the prompt emission, i.e. the initial intense gamma-ray flash, which is believed to originate from internal dissipation processes within the jet. These include internal shocks between overtaking conical shells of material [56] or magnetic reconnection events [56, 57], both of which accelerate electrons to relativistic velocities and produce synchrotron radiation. At early times, the fireball is optically thick and expands relativistically [58]. As it propagates, it becomes optically thin and the gamma-rays are able to escape [56, 58]. The second phase is the afterglow emission, a longer-lasting multi-wavelength radiation resulting from the interaction of the jet with the surrounding interstellar medium [59]. More details on this second phase will be provided in the next section.

Observational evidence suggests two primary origins for GRBs: (i) short GRBs (duration $\lesssim$ 2s) seem to be associated with CBCs (BNS or NSBH systems), and (ii) long GRBs (duration $\gtrsim$ 2s) could result from the core collapse of massive stars [59]. However, exceptions of this classification exist [60, 61]. In both scenarios, highly relativistic bipolar jets are thought to be launched approximately perpendicular to the orbital or accretion disk plane [56]. These jets have Lorentz factors $\Gamma \sim 100 - 1000$ [56, 59], resulting in relativistic beaming that confines the emission to narrow cones with half-opening angles $\theta_j \lesssim 10^{-2}$rad [56].

To illustrate these two distinct channels, we examine in the following two landmarks observations: (i) GRB 170817A associated to GW170817, and (ii) GRB 221009A, called the "BOAT" (Brightest Of All Time), the most luminous long GRB ever recorded. It will also be of interest to compare later the memory effect generated by these GRBs.

(i) Lightcurves of GRB 170817A, as illustrated in Fig. 8, reveal an estimated duration of $2.0 \pm 0.5$ s [59] obtained via the $T_{90}$ statistics[9]. In addition to the fact that GRB 170817A is the sole case of joint detection with GWs, it is a confirmation that BNs are the progenitors of (at least some) short GRBs.

GRB 170817A was notably underluminous with an isotropic energy release of $E_{\text{iso}} = (3.1 \pm 0.7) \times 10^{46}$ erg [63], approximately $10^4$ times fainter than typical short GRBs. It has been first interpreted as evidence for an off-axis jet geometry. The relativistic jet was misaligned with our line of sight by $32^{+10}_{-13}$ degrees as inferred from GW and EM observations [49]. The faintness of its prompt gamma-ray emission has also motivated three theoretical models to explain the observations, and represented in Fig. 9. In the top-hat model, energy is uniformly distributed within a sharp cone, with the observer located away of the jet axis [63]. The structured jet model posits a continuous energy profile peaked on-axis [63]. The cocoon model invokes a two-component outflow: a narrow ultra-relativistic core surrounded by a wider-angle and

[9] In short, it represents the time interval in which the integrated photon counts increase from 5% to 95% of the total counts above the background [62].

slower cocoon produced by jet-cocoon interaction [63]. If the observer is off-axis, the emission is dominated by the latter component [63].

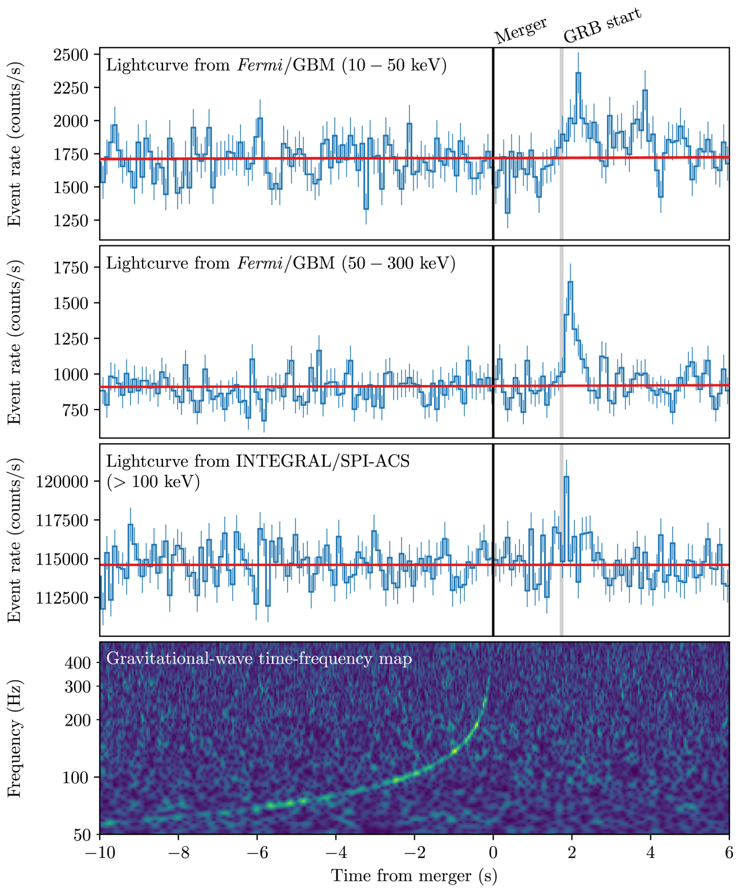


Figure 8: Multi-messenger detection of GW170817 and GRB 170817A obtained with *Fermi*/GBM, *INTEGRAL*/SPI-ACS and LIGO-Virgo detectors/intruments. Top two panels: GBM lightcurves for GRB 170817A in 10–50 keV and 50–300 keV energy ranges with background estimates (red). Third panel: SPI-ACS lightcurve. Bottom panel: Time-frequency map of GW170817 from coherently combined LIGO-Hanford and LIGO-Livingston data, displaying the chirp signature for a CBC [63].

(ii) GRB 221009A represents the most extreme long GRB ever observed and has been dubbed the BOAT [64]. With a duration of $T_{90} \sim 600$s [64, 65] estimated from the lightcurve obtained with *Fermi*, and an isotropic-equivalent energy of $E_{\rm iso} = 10^{55}$erg, the BOAT is believed to originate from the core collapse of a Wolf-Rayet star associated to the supernova SN 2022xiw located at a luminosity distance of 745 Mpc [65]. A small half-opening angle of the jet ($\sim 0.8^{\circ}$) could explain the high energy release with current models [66].

## Afterglow

After releasing the prompt emission, the jet continues its outward propagation and collides with the interstellar medium. This collision results into two distinct shock waves. A forward shock that propagates outward into the external medium at relativistic velocity, sweeping and heating the medium behind it. As pressure builds behind the forward shock, a reverse shock is driven back into the ejecta, decelerating the outflow and converting its bulk kinetic energy into internal energy and accelerating particles [56]. The reverse shock

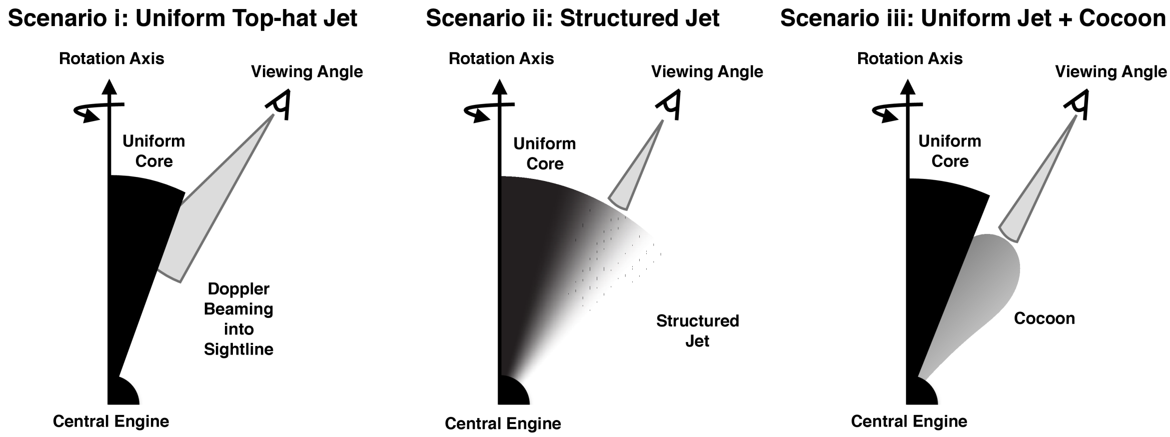


Figure 9: Illustration of top-hat, structured jet, and cocoon models that may explain the observations of GRB 170817A. Extrated from [63].

is associated with the production of optical photons while inverse Comptom scattering of the synchrotron radiation can produce GeV-TeV photons [58]. The combined interaction of both shocks results in broadband synchrotron afterglow emission spanning radio to X-ray wavelengths.

While this standard forward-shock picture reproduces the bulk of multi-wavelength afterglow observations, early-time features such as plateaus and re-brightenings in the lightcurve elude the fire ball model [67, 68]. One possible interpretation invokes a prolonged activity of the central engine, which would continue to inject energy into the blast wave well after the prompt emission has ceased [68]. However, whether these features truly reflect central engine activity or arise instead from other unknown processes [67, 69] remains an open question.

# Scope of the work

The attentive reader will already have noticed that the different ejecta from a BNS and post-merger counterparts produce memory effects. Nonlinear memory, on the other hand, naturally emerges from the GW radiation emitted during the merger itself. The resulting amplitude of the memory from the BNS depends on different factors such as the inclination of the system, the energy of the kilonova related to the ejecta opacity through the merger remnant (and its lifetime) and the mass and velocity of the ejecta. All these parameters can be derived from lightcurves and the GW analysis. Consequently, extrinsic properties imprinted in the lightcurves and GW waveform allow one to predict the memory contribution. In this way, BNSs serve as ideal laboratories for studying different types of (ordinary) memory effect. This thesis will therefore apply the memory formalism specifically to BNS and determine its detectability for each ejecta. To achieve this, a theoretical introduction to the memory effect is first presented including a section on the numerical generation of the nonlinear memory effect. The following chapter addresses the processing of this numerical signal, which exhibit artifacts in its frequency response. Subsequently, models of the ordinary memory effect are developed. The last chapter builds on the previous ones to determine the detectability of the memory effect in ET and LISA detectors for a typical BNS case by examining the contribution of each ejecta and their cumulative impact. A more specialized section on GRBs is also discussed.

Chapter 1

# Memory effect in the context of General Relativity

This first chapter aims at introducing the memory effect (linear and nonlinear) in the GR framework. The notations and basic components of GR will first be introduced, followed by some reminders of relevant equations in the study of GW memory (mainly based on [70]). The chapter concludes with a derivation of the equations expressing memory effects and their numerical computation.

## 1.1 Fundamentals of General Relativity

### 1.1.1 Notations

GR extends Newton's classical theory of gravity to curved spacetimes, describing gravitation as a manifestation of spacetime curvature rather than a force. In this framework, spacetime is modeled as a four-dimensional (differentiable) manifold, and each point $x^\mu$ in it, denoted as an event, is specified by four coordinates as

$$x^\mu = (x^0, \mathbf{x}) \,, \tag{1.1}$$

where $x^0 = ct$ and $\vec{x} = (x^1, x^2, x^3)$ represent time and spatial position. Such vector $x^\mu$ is called a 4-vector. Likewise, we introduce the partial derivatives as

$$\partial_\mu = \frac{\partial}{\partial x^\mu} = \left(\frac{1}{c}\partial_t, \partial_i\right). \tag{1.2}$$

The equations of GR are dense with indices and summations. The Einstein summation convention is thus employed to greatly simplify the readability and satisfy the theorist's innate laziness. Under this convention, an explicit sum of repeated upper and lower indices becomes implicit, and the summation symbol is no longer useful. Moreover, it is customary to use Greek indices for values $(0, 1, 2, 3)$ while Latin letters are for $(1, 2, 3)$. For instance, the following expression reads

$$\sum_{\mu=0}^{3}\sum_{\nu=0}^{3} g_{\mu\nu}x^\mu x^\nu = g_{\mu\nu}x^\mu x^\nu. \tag{1.3}$$

Unless otherwise stated, we adopt natural units by setting $G = c = 1$ throughout this work.

### 1.1.2 Distance and metric

As displacement is at the core of GW memory, the notion of distance must be well defined. In GR, the metric tensor $g_{\mu\nu}$ expresses the invariant line element $s$ between two points on a curved manifold. The metric tensor is assumed to be symmetric, $g_{\mu\nu} = g_{\nu\mu}$ and non-degenerate, i.e. its determinant $\det(g_{\mu\nu}) = g$ is nonzero. The infinitesimal line element $ds$, given the basis dual vector $dx^\mu$ [70], is defined by its square through the expression :

$$ds^2 = g_{\mu\nu} dx^\mu dx^\nu. \tag{1.4}$$

For a (flat) Minkowski spacetime, e.g. the one in special relativity, the convention in this work for its metric $\eta_{\mu\nu}$ is

$$\eta_{\mu\nu} = (-,+,+,+) = \begin{pmatrix} -1 & 0 & 0 & 0 \\ 0 & 1 & 0 & 0 \\ 0 & 0 & 1 & 0 \\ 0 & 0 & 0 & 1 \end{pmatrix}. \tag{1.5}$$

The metric tensor helps to determine the causal structure of spacetime by classifying 4-vectors by the sign of $ds^2$ as timelike ($< 0$), null ($= 0$), or spacelike ($> 0$). This naturally leads to the notion of light cones, which define the possible causal (timelike) or noncausal (spacelike) paths of events evolution. Fig. 1.1 illustrates the causal structure constrained by the light cone on particle worldlines. Particles following a null trajectory on their light cone are particles moving at the speed of light, i.e photons.

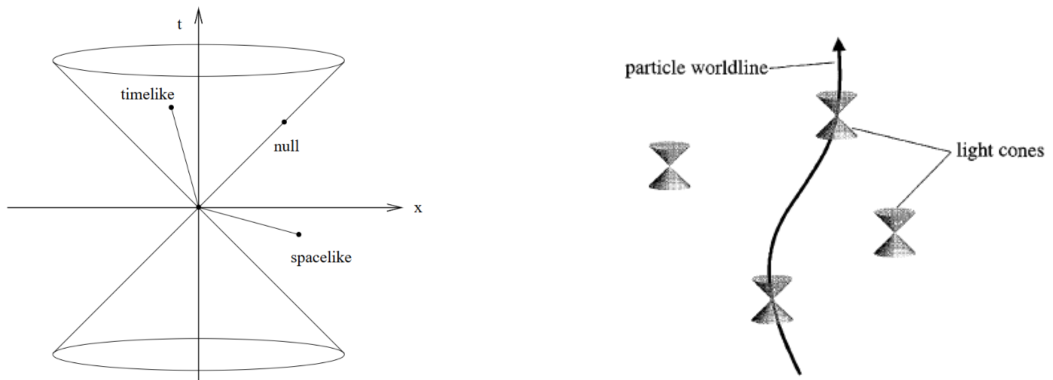


Figure 1.1: *Left*: Light cone representation with the different intervals of $ds^2$, from [71]. *Right*: Trajectory of a particle in spacetime where its light cone constrains the possible causal trajectories at each point. Image adapted from [72].

Additionally, the metric provides a systematic way to raise (resp. lower) indices via contraction with $g^{\mu\nu}$ (resp. $g_{\mu\nu}$, the inverse[1] of $g^{\mu\nu}$), enabling one to convert contravariant components to covariant ones (and vice versa).

### 1.1.3 Gauge symmetry

The tensorial formulation of GR ensures that the theory is invariant under the group of smooth, invertible coordinate transformations (i.e. diffeomorphisms). In other words, the laws in GR retain the same form under any change of coordinates,

$$x^\mu \to x'^\mu(x) \quad \text{and} \quad dx^\mu = \frac{\partial x^\mu}{\partial x'^\nu} dx'^\nu \ , \tag{1.6}$$

[1] As the metric tensor is non-degenerate, the inverse of the metric exists only if the matrix representing it is invertible. Hence the inverse metric, $g^{\mu\nu}$, is defined as $g^{\mu\nu} g_{\nu\alpha} = \delta^\mu_\alpha$.

with $x'$, a differentiable and invertible function with a differentiable inverse that allows a diffeomorphism. As a result, each point of the manifold can be related by a change of coordinates where the line element has to be invariant, so we need to have the relation

$$ds^2 = g_{\mu\nu}(x)dx^\mu dx^\nu = g_{\alpha\beta}(x')dx'^\alpha dx'^\beta. \tag{1.7}$$

Under this assumption, the metric transforms as follows :

$$g_{\mu\nu}(x) \to g'_{\mu\nu}(x') = \frac{\partial x^\alpha}{\partial x'^\mu}\frac{\partial x^\beta}{\partial x'^\nu} g_{\alpha\beta}(x). \tag{1.8}$$

This relation demonstrates the gauge symmetry in GR and expresses that physical laws are equivalent under a change of coordinate system, emphasizing that only geometric quantities physically matter.

### 1.1.4 Covariant derivative

To describe how vectors change as they move through a curved manifold, the Christoffel symbols $\Gamma$ (or connection coefficients) have to be introduced to correct the ordinary definition of the derivative (in the tangent plane of the manifold) caused by changing basis vectors. They are essential for defining the covariant derivative, which generalizes the concept of differentiation to curved spaces[2]. The covariant derivative acting on a vector $V^\alpha$ is then written

$$D_\mu V^\alpha = \partial_\mu V^\alpha + \Gamma^\alpha_{\mu\nu} V^\nu. \tag{1.9}$$

This covariant derivative enables one to define the parallel transport of a vector along a path on a manifold. In order to keep lengths and angles unchanged when a vector is parallel transported, we expect the covariant derivative of the metric to be zero since it is the object that measures these geometric quantities. To satisfy the condition $D_\rho g^{\mu\nu} = 0$, the Christoffel symbols are defined as:

$$\Gamma^\rho_{\mu\nu} = \frac{1}{2} g^{\rho\sigma}\left(\frac{\partial g_{\sigma\mu}}{\partial x^\nu} + \frac{\partial g_{\sigma\nu}}{\partial x^\mu} - \frac{\partial g_{\mu\nu}}{\partial x^\sigma}\right). \tag{1.10}$$

These symbols are not tensors themselves as they depend on the coordinate systems. Christoffel symbols can be non zero due to two facts: the underlying manifold is curved, or the coordinate system itself is curvilinear.

### 1.1.5 Implications of curvature on motion

Consider a test particle on a time-like curve, defined by $ds^2 < 0$ along the curve. The time perceived by this particle along its worldline on the curve is the proper time $\tau$ defined as

$$c^2 d\tau^2 = -ds^2. \tag{1.11}$$

As $\tau$ is assumed to be defined for each point on the curve, it seems natural to parametrize the trajectory as $x^\mu = x^\mu(\tau)$. Thus we obtain :

$$-c^2 = g_{\mu\nu}\frac{dx^\mu}{d\tau}\frac{dx^\nu}{d\tau}. \tag{1.12}$$

[2]The concept of Christoffel symbols and covariant derivative are analogous to the connection and covariant derivative in the context of gauge theory.

If we want to minimize the distance from a starting point $x^\mu(\tau_A)$ to $x^\mu(\tau_B)$, the action $S$ has to be stationary between these two events. As a result, one gets the equation of geodesic that describes the trajectory of a particle on a curved manifold:

$$\frac{d^2x^\mu}{d\tau^2} + \Gamma^\mu_{\nu\rho}(x)\frac{dx^\nu}{d\tau}\frac{dx^\rho}{d\tau} = 0. \tag{1.13}$$

As the name suggests, that specific curve is named a geodesic and represents the shortest path between two points, whose length is stationary. In a flat spacetime, a geodesic is a straight line. In curved spacetime, geodesics can take much more intricate shapes than the straight lines seen in flat geometry. A familiar illustration comes from air travel: the shortest route between Brussels and New York is not a straight line on a map, but rather a curved trajectory on the surface of the Earth.

If an object is accelerated, it will not follow the same geodesic. Such a deviation can be parametrized by two nearby curves : $x^\mu(\tau)$ and $x^\mu(\tau)+\xi^\mu(\tau)$. Taking the difference of the geodesic equation of the two curves and using the definition of the covariant derivative, we get at first linear order the geodesic deviation equation :

$$\frac{D^2\xi^\mu}{D\tau^2} = -R^\mu_{\ \nu\rho\sigma}\,\xi^\rho\,\frac{dx^\nu}{d\tau}\frac{dx^\sigma}{d\tau}\,, \tag{1.14}$$

with $R^\mu_{\ \nu\rho\sigma}$ the Riemann tensor measuring the curvature of the manifold. This can be seen from the fact that the Riemann tensor depends on the derivatives of Christoffel symbols, which themselves depend on the derivative of the metric through :

$$R^\mu_{\ \nu\rho\sigma} = \partial_\rho\Gamma^\mu_{\ \nu\sigma} - \partial_\sigma\Gamma^\mu_{\ \nu\rho} + \Gamma^\mu_{\ \alpha\rho}\Gamma^\alpha_{\ \nu\sigma} - \Gamma^\mu_{\ \alpha\sigma}\Gamma^\alpha_{\ \nu\rho}. \tag{1.15}$$

We now get a physical interpretation of the geodesic deviation equation thanks to the Riemann tensor. The relative displacement between 2 nearby geodesics is induced by the curvature of spacetime (through the Riemann tensor) acting like a classical tidal gravitational force. One can also define the (symmetric) Ricci tensor $R_{\mu\nu} = R^\alpha_{\mu\alpha\nu}$ and contract it to form the Ricci scalar $R = g^{\mu\nu}R_{\mu\nu}$.

### 1.1.6 Einstein's equations

The Einstein field equations (EFE) provide a way to relate how matter and energy, represented by the stress-energy tensor $T_{\mu\nu}$, can affect the curvature of space-time. Einstein's equations, for a non-expanding universe, take the form

$$G_{\mu\nu} \equiv R_{\mu\nu} - \frac{1}{2}g_{\mu\nu}R = \frac{8\pi G}{c^4}T_{\mu\nu}\ , \tag{1.16}$$

providing a geometric formulation of gravitation, where "matter tells spacetime how to curve and spacetime tells matter how to move". The constant $\frac{8\pi G}{c^4}$ is used because, in the appropriate weak-field and non-relativistic limit, these equations reduce to Poisson's equation for the Newtonian gravitational potential.

The EFE are nonlinear in the metric tensor. This nonlinearity arises because the curvature tensor $R_{\mu\nu}$ and $R$ depend not only on the metric itself, but also on its first and second derivative in a nonlinear way, making this set of equations complex and most of the time impossible to solve analytically.

## 1.2 GWs in linearized GR

In view of the complexity of Einstein's coupled, nonlinear equations, we first consider a linear expansion, called a weak field approximation, of Einstein's equations. To do so, we analyse a small perturbation $h$ on top of a flat metric $\eta_{\mu\nu}$. Therefore, the metric reads

$$g_{\mu\nu} = \eta_{\mu\nu} + h_{\mu\nu}\,, \qquad |h_{\mu\nu}| \ll 1. \tag{1.17}$$

In the weak field expansion described above, we implicitly choose a reference frame in which $|h_{\mu\nu}| \ll 1$ holds. This choice breaks the full diffeomorphism invariance of GR, since an arbitrary coordinate transformation would in general eliminate the condition $|h_{\mu\nu}| \ll 1$. Nevertheless, a residual gauge symmetry survives: transformations that are themselves small enough not to spoil the perturbative expansion [70]. Consider an infinitesimal shift of the form

$$x^\mu \to x'^\mu = x^\mu + \xi^\mu(x), \tag{1.18}$$

where $\xi^\mu(x)$ is a vector field such that the derivatives of $\xi^\mu$ be the same order as the perturbation itself,

$$|\partial_\nu \xi^\mu(x)| \sim |h_{\mu\nu}| \ll 1. \tag{1.19}$$

This ensures that the shifted coordinates still describe a nearly flat spacetime and the perturbative framework remains valid. Under this transformation, the metric perturbation changes as

$$h_{\mu\nu}(x) \to h'_{\mu\nu}(x') = h_{\mu\nu}(x) - (\partial_\nu \xi_\mu + \partial_\mu \xi_\nu). \tag{1.20}$$

As $|\partial_\nu \xi^\mu(x)| \ll 1$, the condition $h_{\mu\nu} \ll 1$ is preserved and these diffeomorphisms are a symmetry of the linearized EFE [70].

To compute the linearized EFE, the Riemann tensor, made of Christoffel symbols, has to be linearized by neglecting terms of $\mathcal{O}(h^2)$. In the following, the flat metric $\eta_{\mu\nu}$ is used to raise and lower indices. Given these assumptions, the Christoffel symbols are approximated by

$$\Gamma^\mu_{\nu\rho} = \frac{1}{2}\eta^{\mu\lambda}(\partial_\nu h_{\rho\lambda} + \partial_\rho h_{\nu\lambda} - \partial_\lambda h_{\nu\rho}) + \mathcal{O}(h^2). \tag{1.21}$$

The Riemann tensor defined as Eq. (1.15) takes the form

$$R_{\mu\nu\rho\sigma} = \frac{1}{2}(\partial_\nu\partial_\rho h_{\mu\sigma} + \partial_\mu\partial_\sigma h_{\nu\rho} - \partial_\mu\partial_\rho h_{\nu\sigma} - \partial_\nu\partial_\sigma h_{\mu\rho}). \tag{1.22}$$

To simplify the derivation of the linearized field equations, we employ the trace-reversed perturbation $\bar{h}_{\mu\nu}$, also called the gothic metric:

$$\bar{h}_{\mu\nu} = h_{\mu\nu} - \frac{1}{2}\eta_{\mu\nu}h \quad \text{with } h = \eta^{\mu\nu}h_{\mu\nu}. \tag{1.23}$$

The redefinition is particularly advantageous as it eliminates tedious terms. This equation can be inverted as

$$h_{\mu\nu} = \bar{h}_{\mu\nu} - \frac{1}{2}\eta_{\mu\nu}\bar{h} \quad \text{because } \bar{h} = \eta^{\mu\nu}\bar{h}_{\mu\nu} = -h. \tag{1.24}$$

Given all these ingredients[3], Einstein's equations (1.16) adopt the following form:

$$\Box\bar{h}_{\mu\nu} - \partial_\mu\partial^\rho\bar{h}_{\rho\nu} - \partial^\rho\partial_\nu\bar{h}_{\mu\rho} + \eta_{\mu\nu}\partial^\alpha\partial^\beta\bar{h}_{\alpha\beta} = -\frac{16\pi G}{c^4}T_{\mu\nu}\,. \tag{1.25}$$

where $\eta_{\mu\nu}\partial^\nu\partial^\mu = \partial_\mu\partial^\mu \equiv \Box$ is the d'Alembertian operator in flat space.

[3] A comprehensive demonstration is given in the annex A.1.

### 1.2.1 Harmonic gauge

We can better restrain this equation by applying the invariance under infinitesimal coordinate transformations as in Eq. (1.20). In terms of $\bar{h}_{\mu\nu}$, the transformation becomes

$$\bar{h}_{\mu\nu} \rightarrow \bar{h}'_{\mu\nu} = \bar{h}_{\mu\nu} - (\partial_\mu \xi_\nu + \partial_\nu \xi_\mu - \eta_{\mu\nu} \partial_\rho \xi^\rho). \tag{1.26}$$

If we take the derivative $\partial^\nu$ of the gauge freedom, the transformation is

$$\partial^\nu \bar{h}_{\mu\nu} \rightarrow (\partial^\nu \bar{h}_{\mu\nu})' = \partial^\nu \bar{h}_{\mu\nu} - \Box \xi_\mu. \tag{1.27}$$

In general, $\bar{h}_{\mu\nu}$ will not automatically satisfy any particular constraint, which means its 4-divergence $\partial^\nu \bar{h}_{\mu\nu}$ can be an arbitrary function of spacetime $f_\mu(x)$:

$$\partial^\nu \bar{h}_{\mu\nu} = f_\mu(x). \tag{1.28}$$

We can therefore choose[4] $\xi_\mu$ specifically to cancel $f_\mu(x)$, by requiring it to satisfy:

$$\Box \xi_\mu = f_\mu(x). \tag{1.29}$$

This choice ensures that, in the new gauge, the 4-divergence of the trace-reversed perturbation vanishes :

$$\partial^\nu \bar{h}_{\mu\nu} = 0. \tag{1.30}$$

This specific constraint is called the harmonic gauge[5]. Substituting this into the linearized field equations (1.25) eliminates three of the four terms on the left-hand side, reducing the equation to:

**EFE in harmonic gauge**

$$\Box \bar{h}_{\mu\nu} = -\frac{16\pi G}{c^4} T_{\mu\nu} \tag{1.31}$$

which has a form similar to a wave equation, whose right-hand side acts as a source term for the wave generation coming from the perturbation of the flat metric.

### 1.2.2 Transverse-Traceless gauge

If we are interested in the physical GW detected by LIGO or Virgo, the stress-energy tensor far from the source reduces to $T_{\mu\nu} = 0$, and we simply get

$$\Box \bar{h}_{\mu\nu} = 0. \tag{1.32}$$

which defines a wave propagating in the vacuum at the speed of light.

If we look at the expression of the symmetrical and rank-2 tensor $\bar{h}_{\mu\nu}$, we notice that it has ten independent components, i.e. ten independent degrees of freedom. The four conditions from the harmonic gauge Eq. (1.30) lead to six independent components.

[4]Such a $\xi_\mu$ always exist [70]. The condition Eq. (1.29) is an inhomogeneous wave equation, which can always be solved thanks to the retarded Green's function for any source $f_\mu(x)$.

[5]Many names are given to this gauge in the literature [70]. For instance, the harmonic gauge is called the Hilbert gauge, Lorenz gauge or De Donder gauge.

Having imposed the harmonic gauge, we can demonstrate that there is still a remaining gauge freedom. Under a further coordinate transformation generated by $\xi_\mu$, the divergence transforms as:

$$\partial^\nu \bar{h}_{\mu\nu} \to \partial^\nu (\bar{h}_{\mu\nu})' = \partial^\nu \bar{h}_{\mu\nu} - \Box\xi_\mu \underbrace{=}_{(1.30)} -\Box\xi_\mu. \tag{1.33}$$

The harmonic gauge condition is therefore preserved if and only if the new gauge vector[6] satisfies:

$$\Box\xi_\mu = 0. \tag{1.34}$$

The gauge transformation and the field equation are fully compatible, and the four independent components of $\xi_\mu$ can be freely used to impose four further conditions on $h_{\mu\nu}$. These conditions require that the metric $h_{\mu\nu}$ be:

- purely spatial : $h^{0\mu} = 0$,
- traceless : $h^i{}_i = 0$,
- transverse : $\partial^j h_{ij} = 0$.

This residual gauge is called the transverse-traceless (TT) gauge, as we retain only the transverse and traceless part of $h_{\mu\nu}$. It is denoted by $h_{ij}^{\mathrm{TT}}$. As a result, the two truly physical polarizations of the GW have been isolated by requiring firstly the harmonic gauge and then the residual gauge freedom from $\xi^\mu$, under the assumption to be far from the source [70].

In order to apply the TT gauge to a wave in the harmonic gauge, propagating in a certain direction $\vec{n}$ from the source, it is convenient to apply a projector onto the transverse-traceless part of this wave. Therefore, we first define [70]

$$P_{ij}(\vec{n}) = \delta_{ij} - n_i n_j \ , \tag{1.35}$$

which is a symmetric and transverse projector ($P_{ik}P_{kj} = P_{ij}$) with a trace equals to two. To construct a traceless projector from it, we define the TT projector $\Lambda_{ij,kl}$ as

**TT projector**

$$\Lambda_{ij,kl}(\vec{n}) = P_{ik}P_{jl} - \frac{1}{2}P_{ij}P_{kl} \tag{1.36}$$

$$h_{ij}^{\mathrm{TT}} = \Lambda_{ij,kl}h_{kl} \tag{1.37}$$

### 1.2.3 Polarization basis

A solution of Eq. (1.32) is given by a generic plane-waves solution where we define the wave vector k $= (\omega/c, \vec{k})$ with $\omega/c = |\vec{k}|$. If we assume a wave propagating along the $z$ axis, the solution in TT gauge becomes

$$h_{ij}^{\mathrm{TT}}(t,z) = \begin{pmatrix} h_+ & h_\times & 0 \\ h_\times & -h_+ & 0 \\ 0 & 0 & 0 \end{pmatrix}_{ij} \cos[\omega(t-z)] \ , \tag{1.38}$$

[6] It is important to note this residual $\xi_\mu$, satisfying $\Box\xi_\mu = 0$ is distinct from the gauge vector used in 1.2.1 to reach the harmonic gauge. While the latter was fixed up to a solution of the homogeneous equation, the present $\xi_\mu$ represents the additional freedom that remains after the harmonics gauge has been imposed.

with $h_+, h_\times$ being the plus and cross polarizations, respectively. The interval $ds^2$ reads:

$$ds^2 = dt^2 + dz^2 + [1 + h_+ \cos(\omega(t-z)]dx^2 \tag{1.39}$$
$$+ [1 - h_\times \cos(\omega(t-z))]dy^2 + 2h_\times \cos(\omega(t-z))dxdy\,. \tag{1.40}$$

Finally, a plane wave solution in TT gauge can be explicitly expressed in an orthogonal basis in the transverse plane. If $\mathbf{n}$ is an arbitrary propagation direction unit vector, the standard polarization tensors $e^+_{ij}(\mathbf{n})$ , $e^\times_{ij}(\mathbf{n})$ can be defined as [70]:

$$e^+_{ij}(\mathbf{n}) = \mathbf{u}_i\mathbf{u}_j - \mathbf{v}_i\mathbf{v}_j \ , \quad e^\times_{ij}(\mathbf{n}) = \mathbf{u}_i\mathbf{v}_j + \mathbf{v}_i\mathbf{u}_j \ , \tag{1.41}$$

where $\mathbf{u}, \mathbf{v}$ are unit vectors in the transverse plane (i.e., orthogonal to $\mathbf{n}$) and are orthogonal to each other.

It is straightforward to demonstrate that the polarization tensors are normalized as:

$$e^X_{ij}e^{ij,\ X'} = 2\ \delta^{X,X'}, \tag{1.42}$$

with $X = (+, \times)$. Hence, we obtain:

$$h_+ = \frac{1}{2}e^+_{ij}h^{ij,\ \mathrm{TT}}\,, \quad h_\times = \frac{1}{2}e^\times_{ij}h^{ij,\ \mathrm{TT}}. \tag{1.43}$$

An alternative method for defining the orthonormal basis is to use the vectors' definitions and their inner product. In particular, the following properties hold:

$$\begin{aligned} \mathbf{u}_i\mathbf{u}_j\, e^{+,\ ij} &= 1 \\ \mathbf{u}_i\mathbf{u}_j\, e^{\times,\ ij} &= 0 \\ \mathbf{u}_i\mathbf{v}_j\, e^{+,\ ij} &= 0 \\ \mathbf{u}_i\mathbf{v}_j\, e^{\times,\ ij} &= 1 \end{aligned} \quad \Rightarrow \quad \begin{aligned} h_+ &= \mathbf{u}_i\mathbf{u}_j\, h^{ij,\ \mathrm{TT}} \\ h_\times &= \mathbf{u}_i\mathbf{v}_j\, h^{ij,\ \mathrm{TT}} \end{aligned} \tag{1.44}$$

It is this decomposition that we will use later to determine each polarization.

### 1.2.4 First hint of the memory effect

A first basic formulation of the memory effect can be derived from the geodesic deviation equation expressed in a more suitable frame for detection. While the TT gauge allows GWs to be written easily, what is physically observed is the test mass movement in the proper detector frame. The latter frame is described as a locally inertial frame centered on a detector. In this frame, the coordinate displacement caused by GWs on an object with respect to the detector is explicitly non-zero, which is not the case in the TT frame where the coordinate positions are unaffected by GWs and the effect is encoded in the perturbation of the metric. To express the deformation caused by the passage of GWs, we must evaluate the geodesic deviation equation in the detector's proper reference frame. Starting from Eq. (1.14) and applying the conditions of this frame, the equation simplifies to [70]:

$$\ddot{\xi}^i = \frac{1}{2}\ddot{h}^{\mathrm{TT}}_{ij}\xi^j_0\ , \tag{1.45}$$

where $\xi^i$ is the spatial separation between two freely falling test particles, $\xi^j_0$ is to first order, the constant initial separation and the dot denotes the derivative with respect to the coordinate time $t$ of the proper time frame [70].

Assuming no relative velocity and static condition at early ($t \to -\infty$) and late ($t \to +\infty$) times, and integrating twice over time between early and late times, we obtain simply

$$\int_{-\infty}^{+\infty}\left(\int_{-\infty}^{t'}\ddot{\xi}^i(t") \, dt"\right) dt' = \int_{-\infty}^{+\infty}\left(\int_{-\infty}^{t'}\frac{1}{2}\ddot{h}_{ij}^{\mathrm{TT}}(t")\xi_0^j \, dt"\right) dt' \tag{1.46}$$

$$\Rightarrow \Delta\xi^i = \frac{1}{2}\xi_0^j\Delta h_{ij}^{\mathrm{TT}} \ , \tag{1.47}$$

with $\Delta$ is the difference between late and early times.

It follows directly from the previous relation that if $\Delta h_{ij}^{\mathrm{TT}}$ experiences a net change due to the passage of a GW, meaning its value at late times differs from its initial value, then the test masses will undergo a permanent shift $\Delta\xi^i$ in their relative positions, even after the GW has passed. In other words, *if there is a persistent change in the metric, it leads to a lasting displacement i.e. a memory effect.*

## 1.3 Derivation of the linear memory effect

A more suitable approach for determining the amplitude of the linear memory effect is to work directly with the linearized EFE. The metric perturbation in Eq. (1.31) can be isolated by applying the appropriate Green's function[7] evaluated at the retarded time $t_r$. The retarded Green's function $\Box_{\mathrm{ret}}^{-1}$ applied to a function $f$ is [73]:

$$(\Box_{\mathrm{ret}}^{-1}f)(t,\mathbf{x}) = -\frac{1}{4\pi}\int\frac{d^3x'}{|\mathbf{x}-\mathbf{x}'|}f(t_r,\mathbf{x}') \ , \tag{1.48}$$

where $\mathbf{x}$ denotes the point where we want to evaluate, $\mathbf{x}'$ the source point, and $t_r = t - |\mathbf{x}-\mathbf{x}'|/c$ is the retarded time.

Thus, a general solution to the linearized EFE (1.31) is

$$\bar{h}_{\mu\nu}(t,\mathbf{x}) = \frac{4G}{c^4}\int d^3x'\frac{T_{\mu\nu}(t_{\mathrm{r}},\mathbf{x}')}{|\mathbf{x}-\mathbf{x}'|}. \tag{1.49}$$

For a system of $N$ non-interacting point-like particles, each with mass $m_A$ and position $\mathbf{x}_A(t)$, the stress-energy tensor is [73, 74]

$$T^{\mu\nu}(t,\mathbf{x}) = \sum_{A=1}^{N} m_A\gamma_A u_A^\mu u_A^\nu \, \delta^{(3)}(\mathbf{x}-\mathbf{x}_A(t)) \ , \tag{1.50}$$

where $\gamma_A = 1/\sqrt{1-v_A^2/c^2}$ is the Lorentz factor and $u_A^\mu = \frac{dx_A^\mu}{dt}$ is the four-velocity.

Inserting this $T^{\mu\nu}$ into the expression for $\bar{h}_{\mu\nu}$:

$$\bar{h}_{\mu\nu}(t,\mathbf{x}) = \frac{4G}{c^4}\int d^3x'\int dt_\star\sum_{A=1}^{N} m_A\gamma_A u_A^\mu u_A^\nu\delta^{(3)}(\mathbf{x}'-\mathbf{x}_A(t_\star))\frac{\delta(t_\star - t_r(\mathbf{x}_A(t_\star)))}{|\mathbf{x}-\mathbf{x}'|} \tag{1.51}$$

$$= \frac{4G}{c^4}\int dt_\star\sum_{A=1}^{N} m_A\gamma_A\frac{u_A^\mu u_A^\nu}{|\mathbf{x}-\mathbf{x}_A(t_\star)|}\delta(t_\star - t_r(\mathbf{x}_A(t_\star))) \ . \tag{1.52}$$

[7] Acting as the inverse of the d'Alembertian (wave) operator

Now, we set the observer at a distance $r = |\mathbf{x}|$ from the origin and the source point at $r' = |\mathbf{x}'|$. For an observer far from the source ($r \gg r'$), an expansion gives:

$$\frac{1}{|\mathbf{x}-\mathbf{x}'|} = \frac{1}{r} + \frac{\mathbf{n}\cdot\mathbf{x}'}{r^2} + \frac{1}{2}\sum_{ij}\left[3\frac{x_i x_j}{r^5} - \frac{\delta_{ij}}{r^3}\right] x'_i x'_j + \dots \tag{1.53}$$

$$= \frac{1}{r} + \mathcal{O}(r^{-2}) \ , \tag{1.54}$$

with $\mathbf{n} = \mathbf{x}/r$ the unit vector toward the observer.

Similarly, the relative difference between the point of observation and the source is

$$|\mathbf{x} - \mathbf{x}_A(t)| \simeq r - \mathbf{n}\cdot\mathbf{x}_A(t). \tag{1.55}$$

On the other hand, the Dirac delta distribution of a composite function can be simplified and obeys:

$$\delta(f(t_\star)) = \sum_i \frac{\delta(t_\star - t_{r,i})}{|f'(t_{r,i})|} \ , \tag{1.56}$$

where $t_{r,i}$ are the roots of $f$.

Here,

$$f(t_\star) = t_\star - t + \frac{|\mathbf{x}-\mathbf{x}_A(t_\star)|}{c} \simeq t_\star - t + \frac{r}{c} - \frac{\mathbf{n}\cdot\mathbf{x}_A(t_\star)}{c} \tag{1.57}$$

$$f'(t_r) = 1 - \frac{\mathbf{n}\cdot\mathbf{v}_A(t_r)}{c}. \tag{1.58}$$

Therefore, if we assume that all the point sources are located in a region far from the observer, Eq. (1.52) becomes

$$\bar{h}_{\mu\nu}(t,\mathbf{x}) = \frac{4G}{rc^4}\sum_{A=1}^{N} m_A\gamma_A \frac{u_A^\mu u_A^\nu}{1-\mathbf{n}\cdot\mathbf{v}_A(t_r)/c} \ , \tag{1.59}$$

where all quantities on the right-hand side are evaluated at the retarded time.

In the TT gauge and natural units, the far-zone metric perturbation reduces to:

$$h_{ij}^{\mathrm{TT}}(t,\mathbf{x}) = \frac{4}{r}\sum_{A=1}^{N}\left[\frac{m_A}{\sqrt{1-\mathbf{v}_A^2}}\left(\frac{v_A^i v_A^j}{1-\mathbf{n}\cdot\mathbf{v}_A}\right)\right]^{\mathrm{TT}} . \tag{1.60}$$

The linear memory effect is then the net change:

$$\Delta h_{ij}^{\mathrm{TT}} = \lim_{t\to+\infty} h_{ij}^{\mathrm{TT}}(t,\mathbf{x}) - \lim_{t\to-\infty} h_{ij}^{\mathrm{TT}}(t,\mathbf{x}). \tag{1.61}$$

Thus,

**Linear memory**

$$\Delta h_{ij}^{\mathrm{TT}}(t,r) = \frac{4}{r}\Delta\sum_{A=1}^{N}\left[\frac{m_A}{\sqrt{1-\mathbf{v}_A^2}}\left(\frac{v_A^i v_A^j}{1-\mathbf{n}\cdot\mathbf{v}_A}\right)\right]^{\mathrm{TT}} \tag{1.62}$$

where $\Delta$ signifies the difference between final and initial states.

## 1.4 Derivation of the nonlinear memory

The Christodoulou effect is mathematically more complex and tedious to extract. Nevertheless, to give an insight into the origin of this effect, we adopt an analysis similar to that of Favata in [6]. Rather than truncating the Einstein equations at first order in $h_{\mu\nu}$ as in Section 1.2, we now retain the quadratic contributions from the Christoffel symbols. The EFE in harmonic gauge can be written as [6]:

$$\Box h^{\alpha\beta} = \frac{16\pi G}{c^4}\mathcal{T}^{\alpha\beta}\ , \tag{1.63}$$

where the new source term $\mathcal{T}^{\alpha\beta}$ is a pseudo-tensor made of the matter fields $T^{\alpha\beta}$ and the gravitational field $\Lambda^{\alpha\beta}$:

$$\mathcal{T}^{\alpha\beta} = (-g)T^{\alpha\beta} + \frac{c^4}{16\pi G}\Lambda^{\alpha\beta}. \tag{1.64}$$

$\Lambda^{\alpha\beta}$ is an expression containing non-linear terms (from the Christoffel symbols and Riemann tensor) at least quadratic in $h^{\alpha\beta}$ and its derivatives [73]:

$$\begin{aligned}\Lambda^{\alpha\beta} =& - h^{\mu\nu}\partial^2_{\mu\nu}h^{\alpha\beta} + \partial_\mu h^{\alpha\nu}\partial_\nu h^{\beta\mu} + \frac{1}{2}g^{\alpha\beta}g_{\mu\nu}\partial_\lambda h^{\mu\tau}\partial_\tau h^{\nu\lambda}\\ &- g^{\alpha\mu}g_{\nu\tau}\partial_\lambda h^{\beta\tau}\partial_\mu h^{\nu\lambda} - g^{\beta\mu}g_{\nu\tau}\partial_\lambda h^{\alpha\tau}\partial_\mu h^{\nu\lambda} + g_{\mu\nu}g^{\lambda\tau}\partial_\lambda h^{\alpha\mu}\partial_\tau h^{\beta\nu}\\ &+ \frac{1}{8}(2g^{\alpha\mu}g^{\beta\nu} - g^{\alpha\beta}g^{\mu\nu})(2g_{\lambda\tau}g_{\epsilon\pi} - g_{\tau\epsilon}g_{\lambda\pi})\partial_\mu h^{\lambda\pi}\partial_\nu h^{\tau\epsilon}.\end{aligned} \tag{1.65}$$

It captures the fact that gravity carries energy, and this gravitational energy in turn acts as a source for the gravitational field.

Favata links $\Lambda^{\alpha\beta}$ to the Landau-Lifshitz pseudotensor $t^{\alpha\beta}_{\rm LL}$ [75] which expresses locally the conservation of energy-momentum of matter and the energy of the gravitational field[8]. The two elements are similar[9] and one obtains the EFE in harmonic gauge for the gothic metric:

$$\Box\bar{h}^{\alpha\beta} = -16\pi(-g)(T^{\alpha\beta} + t^{\alpha\beta}_{\rm LL}) - \partial_\nu\bar{h}^{\alpha\mu}\partial_\mu\bar{h}^{\beta\nu} + \bar{h}^{\mu\nu}\partial_\mu\partial_\nu\bar{h}^{\alpha\beta}. \tag{1.66}$$

A specific part of the Landau-Lifshitz pseudotensor is equivalent to the energy carried by GWs, described by the GW stress-energy tensor $T^{\rm gw}_{jk}$. This tensor can be written in terms of the averaged squared time derivatives of the wave amplitudes, and in the far-zone where the waves can be treated as plane waves, it simplifies to an explicit dependence on the energy flux (of the GW) per unit solid angle, directed radially [6]:

$$T^{\rm gw}_{jk} = \frac{1}{32\pi}\left\langle h^{\rm TT}_{ab,j}h^{\rm TT}_{ab,k}\right\rangle \approx T^{\rm gw}_{00}n_j n_k = \frac{1}{r^2}\frac{dE^{\rm gw}}{dtd\Omega}n_j n_k\ , \tag{1.67}$$

where $\frac{dE^{\rm gw}}{dtd\Omega}$ is the energy flux emitted per unit time and solid angle at a distance $r$, and $n_j$ is the unit vector pointing radially outward from the source. The brackets denote averaging over several wavelengths, and the plane wave approximation has been used for the last equality [6].

Substituting this in Eq. (1.66) shows that the contribution from the GW energy flux adds a specific correction to the observed GW field. This correction to the GW field is the nonlinear memory:

[8] The Landau-Lifshitz object is a pseudotensor rather than a true tensor because, in GR, gravitational energy cannot be localized in a coordinate-independent manner. In any local inertial frame (where the metric is Minkowskian), the pseudotensor vanishes, reflecting the equivalence principle.

[9] An expression of the Landau-Lifshitz pseudotensor is given in the appendix A.2.

Nonlinear memory

$$\delta h_{ij}^{\mathrm{TT}}(t,r) = \frac{4}{r}\int_{-\infty}^{t_r} dt' \left[\int \frac{dE^{\mathrm{gw}}}{dt'd\Omega'}\frac{n_i n_j}{1-\mathbf{n}\cdot\mathbf{N}}d\Omega'\right]^{\mathrm{TT}} \tag{1.68}$$

which is the integral over the energy flux in all directions, weighted by geometric factors, and projected onto the transverse-traceless part. Here, $t_r$ is the retarded time, $\mathbf{N}$ is the direction to the observer and $\mathbf{n}$ the unit vector pointing in the direction of energy emission.

## 1.5 Modeling the nonlinear memory effect

### 1.5.1 Mode decomposition

It can be shown [6, 76, 77] that the GW energy flux is related to the GW polarizations through

$$\frac{dE^{\mathrm{gw}}}{dt\,d\Omega} = \frac{r^2}{16\pi}\left\langle \dot{h}_+^2 + \dot{h}_\times^2 \right\rangle. \tag{1.69}$$

where the brackets mean to average over multiple wavelengths.

Substituting this expression into Eq. (1.68) leads to a complex integral, because the polarizations depend on both time and angular components. To simplify the double integration, it is standard in the literature [5, 77, 78] to decompose the complex strain $h_+ - ih_\times$ into multipoles $h_{\ell m}(t)$ of spin-weighted spherical harmonics ${}_{-2}Y_{\ell m}$:

$$h_+(t,\theta,\phi) - ih_\times(t,\theta,\phi) = \sum_{\ell=2}^{\infty}\sum_{m=-\ell}^{\ell} h_{\ell m}(t)\ {}_{-2}Y_{\ell m}(\theta,\phi), \tag{1.70}$$

where ${}_{-2}Y_{\ell m}(\theta,\phi)$ are the spin-weighted spherical harmonics with spin weight $-2$. This mathematical tool will be discussed in the following section. Here $\theta$ is the polar inclination angle measured from the positive $z$-axis[10], and $\phi$ is the azimuthal angle around the $z$-axis measured from the $x$-axis. For the same reason that there is no GWs emission from a monopole or dipole, the sum over $\ell$ starts at $\ell = 2$[11].

#### Spin-weighted spherical harmonics

The formalism associated to spin-weighted spherical harmonics was first introduced by Newman and Penrose [79] in the context of asymptotically flat spacetimes. In short, the linearized EFE admit separable solutions in terms of spin-weighted spherical harmonics [80]. The decomposition in Eq. (1.70) cleanly factorizes the signal into a time-dependent part, carried by the mode amplitudes $h_{\ell m}(t)$, and a purely angular part, encoded in the ${}_{-2}Y_{\ell m}$ basis. In this decomposition, $\ell$ and $m$ ($-\ell \leqslant m \leqslant \ell$) are defined in the same way as for spherical harmonics.

The spin weight $s$ characterizes how a field transforms under rotations around the line of sight. A function $f_s(\theta,\phi)$ on the sphere is said to have spin weight $s$ if it transforms

[10] In our work, $\theta = 0$ corresponds to the North Pole (viewing the binary face-on along the positive $z$-axis), while $\theta = \pi$ corresponds to the South Pole (face-on along the negative $z$-axis).

[11] An illustration of the real and imaginary parts of the spin–2 harmonics is provided in the appendix A.3.

under the local $U(1)$ gauge freedom parametrized by an angle $\psi$ in the plane perpendicular to the propagation direction [79, 81],

$$f_s \to f'_s = e^{-is\psi} f_s. \tag{1.71}$$

For the case $s = 0$, one recovers the ordinary spherical harmonics ${}_0Y_{\ell m} = Y_{\ell m}(\theta, \phi)$ [81].

As the name suggests, spin-weighted spherical harmonics are constructed on the basis of the standard spherical harmonics $Y_{\ell m}$. They take the explicit form [82]:

$$ {}_sY_{\ell m}(\theta,\phi) = \begin{cases} \sqrt{\dfrac{(\ell-s)!}{(\ell+s)!}}\,\eth^s Y_{\ell m}(\theta,\phi), & \ell \geqslant s \geqslant 0 \\ (-1)^s\sqrt{\dfrac{(\ell+s)!}{(\ell-s)!}}\,\bar{\eth}^{-s} Y_{\ell m}(\theta,\phi), & 0 > s \geqslant -\ell \\ 0, & |s| > \ell \end{cases} \tag{1.72}$$

where the operator $\eth$ and its conjugate $\bar{\eth}$, when acting on a scalar function $f_s(\theta, \phi)$ with spin-weight $s$, are defined by [82]

$$\eth f_s(\theta,\phi) \equiv -\sin^s\theta\left(\partial_\theta + i\sin^{-1}\theta\,\partial_\phi\right)\left(f_s\sin^{-s}\theta\right), \tag{1.73}$$
$$\bar{\eth} f_s(\theta,\phi) \equiv -\sin^{-s}\theta\left(\partial_\theta - i\sin^{-1}\theta\,\partial_\phi\right)\left(f_s\sin^{s}\theta\right). \tag{1.74}$$

### Properties of spin-weighted spherical harmonics

These spin-weighted spherical harmonics are particularly well suited to GWs because their polarizations behave as a spin-2 tensorial field: under a rotation by an angle $\psi$ around the line of sight, the combination $h_+ - ih_\times$ transforms as [81]

$$h_+ - ih_\times \;\to\; e^{2i\psi}\left(h_+ - ih_\times\right), \tag{1.75}$$

which is exactly the transformation law of a tensor field with spin weight $-2$ as defined in Eq. (1.71).

Spin-weighted spherical harmonics form a complete and orthogonal basis of functions on the sphere [81]. Hence, the orthogonality for a set of functions with spin weight $s$ is expressed as:

$$\int_{4\pi} {}_s\bar{Y}_{\ell' m'}\ {}_sY_{\ell m} d\Omega = \delta_{\ell'\ell}\delta_{mm'}, \tag{1.76}$$

and satisfy the completeness relation

$$\sum_{\ell m} {}_s\bar{Y}_{\ell m}(\theta',\phi')\ {}_sY_{\ell m}(\theta,\phi) = \delta(\phi'-\phi)\ \delta(\cos\theta' - \cos\theta), \tag{1.77}$$

where ${}_s\bar{Y}_{\ell m}$ is the conjugate of ${}_sY_{\ell m}$.

### Relation to Wigner-D matrices

To compute spin-weighted spherical harmonics, it is convenient to express them in terms of Wigner-D matrices $d^l_{ms}(\theta)$. In practice, a spherical harmonics of spin $s$ is also defined by [6]:

$${}_sY_{lm}(\theta,\phi) = (-1)^s\sqrt{\frac{2l+1}{4\pi}}d^l_{ms}(\theta)e^{im\phi}. \tag{1.78}$$

And the Wigner-D matrices $d^l_{ms}(\theta)$ are

$$d^l_{ms}(\theta) = \sqrt{(l+m)!(l-m)!(l+s)!(l-s)!} \times \sum_{k=k_i}^{k_f} \frac{(-1)^k (\sin\frac{\theta}{2})^{2k+s-m} (\cos\frac{\theta}{2})^{2l+m-s-2k}}{k!(l+m-k)!(l-s-k)!(s-m+k)!}\,, \tag{1.79}$$

with $k_i = \max(0, m-s)$, $k_f = \min(l+m, l-s)$ [6].

As part of this master's thesis, we use Wigner-D matrices only as a tool for calculating the spin-weighted spherical harmonics, but these functions are more complex. Let's mention that these matrices related to quantum theory of angular momentum [83] and group theory [84]. We refer curious readers to the associated references.

### 1.5.2 Nonlinear memory in terms of Wigner-D matrices and multipoles

As a result of this formalism, the nonlinear memory effect can be rewritten in terms of spin-weighted spherical harmonics themselves made of Wigner-D matrices. The memory relation in Eq. 1.68 can be decomposed in terms of modes $(\ell, m)$ by first projecting the energy flux (a scalar quantity) on the basis made of spherical harmonics (of spin 0). The nonlinear memory in terms of modes $h^{\rm mem}_{\ell m}$ takes the form [6]:

$$h^{\rm mem}_{\ell m} = \frac{16\pi}{r}\sqrt{\frac{(\ell-2)!}{(\ell+2)!}} \int_{-\infty}^{t_r} dt' \int \frac{dE^{\rm gw}}{dt' d\Omega'} \bar{Y}_{\ell m}(\Omega), \tag{1.80}$$

and the energy flux of the GW, composed of the derivatives of the metric (a spin-2 tensorial field), can be obtained by projecting Eq. 1.69 on the ${}_{-2}Y_{\ell m}$ [6]:

$$\frac{dE^{\rm gw}}{dt\, d\Omega} = \frac{r^2}{16\pi} \sum_{\ell'=2}^{\infty} \sum_{\ell''=2}^{\infty} \sum_{m'=-\ell'}^{\ell'} \sum_{m''=-\ell''}^{\ell''} \dot{h}_{\ell' m'} \dot{\bar{h}}_{\ell'' m''}\, {}_{-2}Y_{\ell' m'}(\Omega) {}_{-2}\bar{Y}_{\ell m}(\Omega). \tag{1.81}$$

Hence, a new expression for the nonlinear memory effect decomposed in spin-weighted spherical harmonics is [6, 78]:

$$h^{\rm mem}_{\ell m} = r\sqrt{\frac{(\ell-2)!}{(\ell+2)!}} \sum_{\ell'=2}^{\infty} \sum_{\ell''=2}^{\infty} \sum_{m'=-\ell'}^{\ell'} \sum_{m''=-\ell''}^{\ell''} \times \mathcal{G}^{\ell\ell'\ell''}_{mm'm"} \int_{-\infty}^{t_r} dt\, \dot{h}_{\ell' m'}\, \dot{\bar{h}}_{\ell'' m''}, \tag{1.82}$$

with

$$\mathcal{G}^{\ell\ell'\ell''}_{mm'm''} = \int d\Omega\, {}_{-2}\bar{Y}^{\ell m}(\Omega)\, {}_{-2}Y^{\ell' m'}(\Omega)\, \bar{Y}^{\ell'' m''}(\Omega). \tag{1.83}$$

The angular integral $\mathcal{G}^{\ell\ell'\ell''}_{mm'm''}$ is then reduced to an integral expressed in terms of Wigner-D matrices thanks to the relation Eq. (1.78). Although only a factor $r$ explicitly appears in the expression, the $r^{-1}$ scaling is preserved because $h_{\ell m} \sim r^{-1}$. Thus, $h^{\rm mem}_{\ell m} \sim r^{-1}$ as in the previous treatment.

By applying Eq. (1.82), we can decompose the nonlinear memory effect into its constituent spherical harmonic components. Figure 1.2 highlights the resulting mode hierarchy for a quasi-circular, non-precessing binary for both the oscillatory and memory modes.

For the oscillating part, the quadrupolar mode $h_{22}^{\mathrm{osc}}$ drives the GW (right panel) and thus acting as the primary source of the memory flux[12] since it contains the most information about the GW. The specific dominance of $\ell = 2$ modes over the rest of the spectrum come from the assumed symmetries of the binary. Higher-order oscillatory modes ($h_{44}$, $h_{42}$) radiate less efficiently and odd-$\ell$ modes ($h_{32}$) are suppressed in binaries with comparable masses [76].

Although the dominant contribution to the nonlinear memory is sourced by $h_{22}^{\mathrm{osc}}$, the memory signal itself does not reside in this specific mode. For the memory modes, the non-oscillating part is contained mostly within the $h_{20}^{\mathrm{mem}}$ mode (left panel). This is a direct consequence of the phase dependence on the memory from the spin-weighted spherical harmonics decomposition ($\propto e^{im\phi}$ and $\phi$ the orbital phase), which dictates that only $m = 0$ modes can produce a non-oscillatory offset. In essence, $h_{22}^{\mathrm{osc}}$ acts as the primary *source* of the memory, while $h_{20}^{\mathrm{mem}}$ is the dominant *carrier* of the resulting nonlinear memory. Note that precession can also excite odd-$m$ memory components by breaking the symmetry of the system [85].

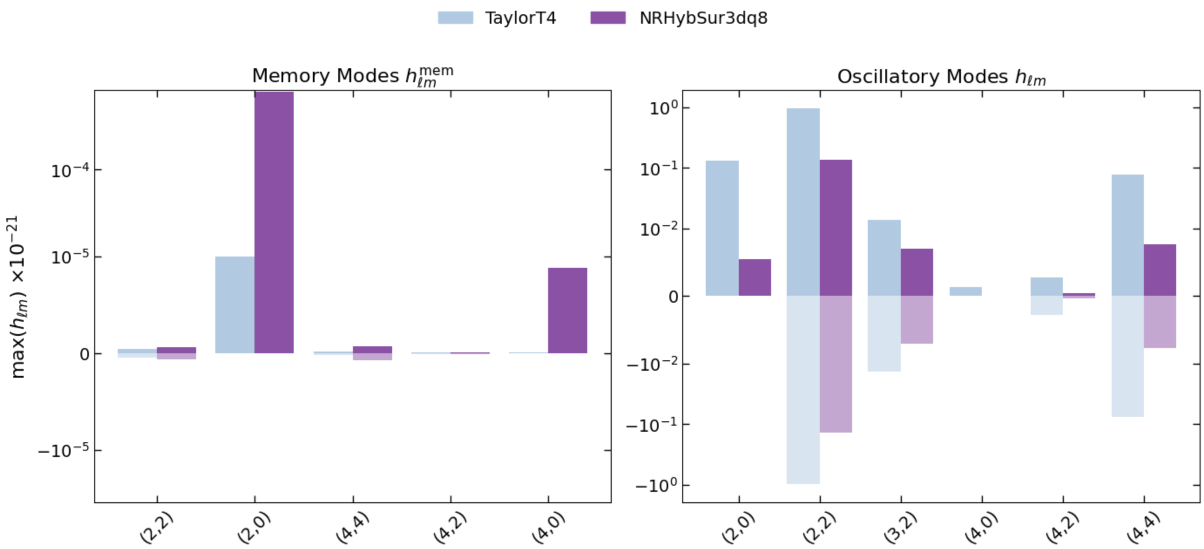


Figure 1.2: Contribution of the peak contribution per mode to the total memory (*left*) and to the waveform (*right*) between the TaylorT4 and NRHybSur3dq8 approximants. TaylorT4 is an inspiral-only approximant for low-mass binaries ($\lesssim 12M_{\odot}$) [86], while NRHybSur3dq8 is a surrogate model that captures the inspiral, merger, and ringdown stages by interpolating numerical relativity data (more detail in the next subsection). Upper (lower) bars correspond to $m > 0$ ($m < 0$), both representing maximum positive strain. A threshold at $10^{-30}$ has been used to only display the dominant modes. The differences between the values of the two approximations can be explained by their different nature. The modes $h_{\ell m}^{\mathrm{mem}}$ are obtained via relation Eq. (1.82) for the case of a system of two masses equal to 3 $M_{\odot}$, a luminosity distance of 40 Mpc seen edge-on.

[12]Through the GW energy flux $\propto \int_{-\infty}^{t_r} |\dot{h}_{22}|^2\, dt$.

### 1.5.3 Numerical implementation

From a numerical perspective, we used two Python packages to calculate and obtain the nonlinear memory effect. On the one hand, `GWSurrogate` [87] allows the $h_{lm}$ modes to be extracted directly from surrogate models. On the other hand, nonlinear memory can be obtained directly from the `GWMemory` package [8].

#### GWSurrogate

A surrogate model is a substitute or approximation that mimics the behavior of a full underlying model within a fixed range of parameters [87]. The model is created by first running a full computationally expensive underlying model at selected sample points in the parameter space of interest. Each run of the complex model takes a long time to complete but these high-fidelity evaluations form the training dataset that captures the behavior of the system across different trained parameters. Once this dataset of solutions is concatenated, interpolation between the samples is applied to form a more complete model [87].

The main advantage of surrogate models is their computational speed. Once the expensive dataset is created, the surrogate can evaluate outputs faster than re-running the whole complex model.

In our context, surrogate models are provided by `GWSurrogate` [87], a Python package designed specifically for GW waveform models built from numerical relativity (NR) simulations. The package returns the modes $h_{\ell m}$ of surrogate models, which is convenient for determining the memory effect as in Eq. (1.82). Table 1.1 below includes the models present in `GWSurrogate` and their scope of validity in terms of the parameters on which they were trained.

Table 1.1: Surrogate models contained in `GWSurrogate`

| | | Training details | | |
|---|---|---|---|---|
| Model | Description | Mass ratio | Spin | Memory |
| NRSur7dq4 [88] | Generically precessing BBHs | $q \leqslant 4$ | Yes | No |
| NRHybSur3dq8 [89] | Nonprecessing BBHs | $q \leqslant 8$ | No | No |
| NRHybSur2dq15 [90] | Nonprecessing BBHs | $q \leqslant 15$ | Yes | No |
| NRHybSur3dq8_CCE [91] | Nonprecessing BBHs | $q \leqslant 8$ | No | Yes |

#### GWMemory

For more accurate estimates of the nonlinear memory effect, we can use the Python package `GWMemory` [8]. `GWMemory` employs four distinct oscillatory waveform models to compute the nonlinear memory effect. These are summarized in Table 1.2.

Table 1.2: Waveform models present in `GWMemory` [76]

| Model | Type | Description | Modes |
|---|---|---|---|
| NRSur7dq4 | NR surrogate | Trained directly on NR simulations | $\ell \leqslant 4$ |
| SEOBNRv4 | Effective-one-body (EOB) | Maps two-body dynamics onto single particle in deformed metric using analytical results | $\ell = 2$, $\lvert m\rvert = 2$ |
| IMRPhenomD | Phenomenological | Combines theoretical approaches (EOB, post-Newtonian) calibrated to numerical data | $\ell = 2$, $\lvert m\rvert = 2$ |
| MWM | Minimal Waveform Model | Matches leading-order inspiral to ringdown using NR and EOB information | $\ell = 2$, $\lvert m\rvert = 2$ |

From these generated oscillatory modes, `GWMemory` computes the time derivative $\dot{h}_{\ell m}(t)$ (with its conjugate $\dot{\bar{h}}_{\ell m}(t)$) and then evaluates the energy integral between a finite lower time $t_0$ and the retarded time $t_r$:

$$H^{m_1 m_2}_{\ell_1 \ell_2}(t_0, t_r) = \int_{t_0}^{t_r} \dot{h}_{\ell_1 m_1}(t)\, \dot{\bar{h}}_{\ell_2 m_2}(t)\, dt. \tag{1.84}$$

The lower cutoff $t_0$ represents the time when the binary enters the sensitive band of LIGO, corresponding to a GW frequency of 20 Hz [76]. This truncation is physically justified because the memory accumulated at earlier times (lower frequencies) contributes negligibly to the observable signal.

This time integral is then coupled with geometric coefficients to produce the final memory amplitude $\delta h_{\ell m}$. For each output memory mode $(\ell, m)$, the calculation sums over all relevant pairs of input oscillatory modes $(\ell_1, m_1, \ell_2, m_2)$:

$$\delta h_{\ell m} = \frac{r}{4\pi c} \sum_{\ell_1, m_1} \sum_{\ell_2, m_2} \Gamma^{\ell_1 \ell_2 m_1 m_2}_{\ell m}(\theta, \phi)\, H^{m_1 m_2}_{\ell_1 \ell_2}(t_0, t_r). \tag{1.85}$$

Here, $\Gamma^{\ell_1 \ell_2 m_1 m_2}_{\ell m}$ are purely geometric coupling coefficients that describe how the energy from specific pairs of oscillatory modes contributes to each memory mode. These coefficients are independent of the binary's physical parameters and can be tabulated in advance for computational efficiency [76].

A major result provided by the package concerns the effect of higher-order oscillatory modes in shaping the memory signal. The `GWMemory` framework demonstrates that accounting for harmonic modes beyond the dominant quadrupole ($\ell = |m| = 2$) yields a difference in amplitude compared to the single-mode approximation. Models including all modes up to $\ell \leqslant 4$ exhibit deviations of $\mathcal{O}(10\%)$ in memory amplitude relative to the $\ell = |m| = 2$ only case. These deviations become more pronounced in systems characterized by unequal mass ratios or spin precession, as illustrated in Fig. 1.3. This behavior departs from the predictions of earlier approximations Eqs 1.86 and (1.87), which neglect higher multipoles. Notably, the inclusion of these additional modes generates a nonzero cross-polarization component $h_\times$ in nonspinning, unequal-mass systems, a feature that is completely absent when only the dominant $(\ell, m) = (2, 2)$ mode is retained [76].

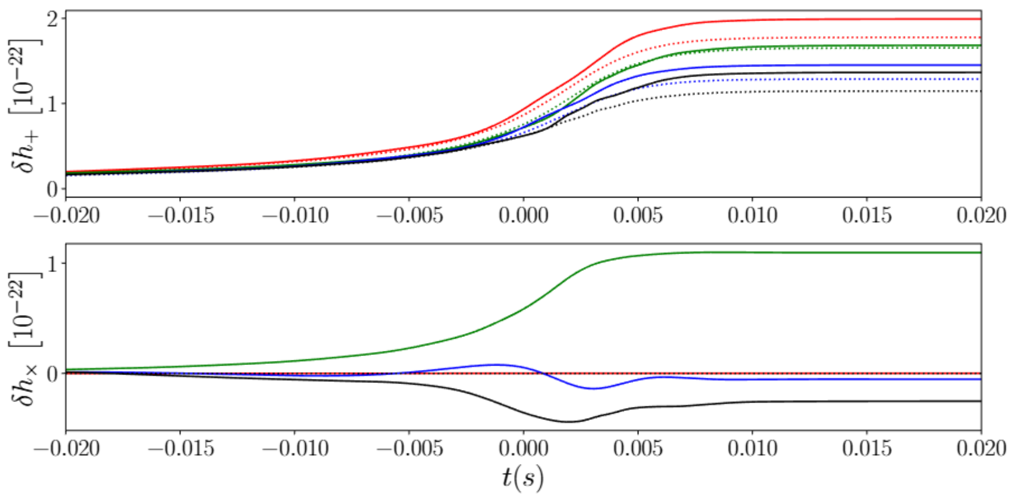


Figure 1.3: Importance of including higher order modes for $h_+$ (top panel) and $h_\times$ (bottom panel) polarizations of the memory signal when using only the $\ell = |m| = 2$ oscillatory modes (dotted) and when using all modes with $\ell \leqslant 4$ (solid). The colors are for binaries as follows: red is equal-mass ($q = 1$) and non-spinning, green is equal-mass with precessing spins, blue is unequal-mass and non-spinning, black is unequal-mass ($q \equiv m_1/m_2 = 2$) with precessing spins. The systems shown are edge-on ($\theta = \pi/2$, $\phi = 0$) with total mass, $M = 60M_\odot$, at a luminosity distance $D_L = 400$ Mpc. Figure extracted from [76].

### 1.5.4 Application to the memory mode in CBC systems

In NS mergers, the waveform is dominated by the quadrupolar and oscillatory mode $h_{22}$ [21]. Under the assumptions of quasi-circular and non-precessing orbits, the nonlinear memory effect can be directly computed from this dominant mode. Specifically, the memory signal observed with an inclination angle $\theta$, derived from the $h_{22}$ mode only, is given by [21, 76, 77, 92]:

$$h_+^{\text{mem}} = \frac{r}{192\pi} \sin^2\theta \, (17 + \cos^2\theta) \int_{-\infty}^{t_r} |\dot{h}_{22}|^2 \, dt, \tag{1.86}$$

$$h_\times^{\text{mem}} = 0. \tag{1.87}$$

Here, the polarization axes $x$ and $y$ in the plane of the sky are chosen such that the $x-$axis coincides with the projection of the binary(s orbital angular momentum. The cancellation of the $\times$ polarization stems from the assumptions of non-precession and circular orbit. Under these assumptions, the system possesses axial symmetry about the orbital axis, ensuring that the memory is purely $+$-polarized. A different choice of coordinates, such as a $45^\circ$ rotation around the propagation axis, would rotate the signal entirely into the $\times$ polarization. It is important to note that the expression in Eq. (1.86) assumes that memory is sourced predominantly by $h_{22}$ and carried by $h_{20}$. If additional modes such as $(\ell, m) = (4, 0)$ contribute, this simplified model is no longer correct and more advanced tools are required [6, 76].

A comparison of the behavior dictated by Eq. (1.86) and the package `GWMemory` is shown in Fig. 1.4. When we tried to implement this method using the PyCBC package, we noticed a difference of approximately a factor 0.5 between the memory obtained via Eq. (1.86) and that of `GWMemory` for the same parameters. After a thorough investigation, we found that this discrepancy is caused by the fact that `GWMemory` computes the memory with all the modes available in the model by default, while in our implementation of the formula Eq. (1.86), only the $(2,2)$ mode is used because it is assumed to be the single dominant mode. Since the $(2,-2)$ mode has the same amplitude as the $(2,2)$ mode and both dominate the waveform, this results in a factor-of-two difference, as shown. Setting `GWMemory` to exclusively use the $(2,2)$ mode resolves this discrepancy and confirms the consistency of our implementation. We will therefore use `GWMemory` for all subsequent nonlinear memory computation, as it is a standard tool adopted in the literature and provides a more complete estimate by incorporating contributions from all available modes beyond the dominant (2,2) pair.

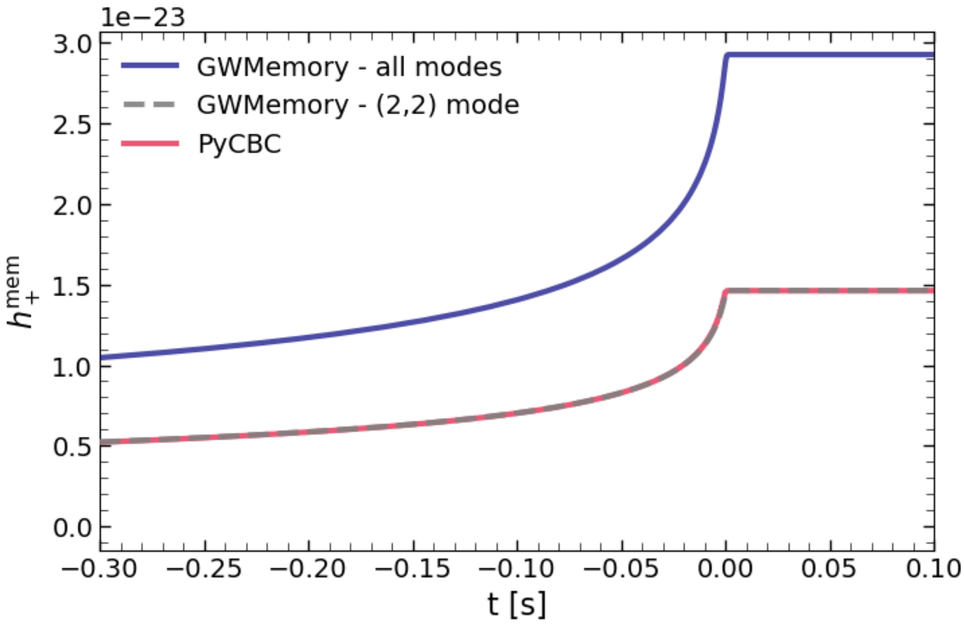


Figure 1.4: Comparison of the nonlinear memory effect, computed using the `GWMemory` package, and the PyCBC-based (with Eq. (1.86)) implementation. The waveforms were generated for a BNS with equal masses (total mass $M = 3M_\odot$), observed edge-on at a distance of 40 Mpc using the IRMPhenomD approximant.

# Chapter 2

# Memory signal pre-processing and detectability

To estimate the detectability of the memory effect, its frequency content must be compared to the one of the detector. To this end, we compute the Fourier Transform (FT) of the temporal memory signal to determine its frequency-domain evolution.

If the memory signal is not based on a mathematical function but rather on an algorithm (such as `GWMemory`) or calculated from a simulation, it must be processed before computing its FT. In this chapter, we will examine the two pre-processing methods: padding and tapering, to reduce artifacts resulting from the FT of a non-periodic function. Ignoring these artifacts would result in an incorrect frequency evolution of the signal. This would in turn affect the theoretical detectability of the signal through the computation of the SNR. Sections 2.1.1, 2.1.2, 2.2 and 2.3.1 are structured similarly to the article [93].

## 2.1 Fast Fourier Transforms of step-like functions

### 2.1.1 Frequency characteristics

The memory signal alone, whether linear or nonlinear, takes the form of a step function. As a first step, we model the temporal evolution of memory using a Heaviside function $H(t)$. The frequency trend of this simplified memory is determined by calculating the FT. It is well known that the FT of the Heaviside step function $\tilde{H}(f)$ reads

$$\tilde{H}(f) = \int_{-\infty}^{+\infty} dt\ H(t)e^{2\pi ift} = \int_{0}^{+\infty} dt\ e^{2\pi ift} = \frac{1}{2}\delta(f) + \frac{1}{i2\pi f} \sim f^{-1}\ , \tag{2.1}$$

where $\delta(f)$ is the Dirac delta distribution. The first term, $\frac{1}{2}\delta(f)$, represents the zero-frequency contribution inherent to the step. This means that most of the power of our modeled memory is present near zero-frequency, and the other part diminishes with frequency. The former is neglected as it represents a permanent displacement that does not produce a detectable signal within the instrument's frequency band. As an example, the lowest frequencies we consider correspond to the minimum sensitivity of LISA, which is approximately $10^{-5}$ Hz.

The frequency signature in $f^{-1}$ is a characteristic that will reappear several times in the modeling of the memory effect. This decay represents the spectral signature of the permanent offset between the early-time and late-time states of the system. It should also be noted that this signature is a consequence inherent in our simplified model, based on a discontinuous function. The decay in $f^{-1}$ is solely the frequency domain representation of the discontinuous jump, and therefore does not reflect a completed modeling of the memory effect, which in reality takes a non-zero time to saturate.

### 2.1.2 Discrete Fourier Transform

In practice, the methods used to obtain the memory effect (`GWMemory` for nonlinear memory or numerical calculations based on simulations for the kilonova) do not yield a continuous and analytical function $x$ that is defined for all times $t$. Instead, we obtain the evolution of a discrete function in a finite time interval.

Hence, the memory signal is a time series $\{x_j = x(t_j)|\ j = 0, \dots N-1\}$ consisting of a finite number of data points $N$, spaced by a uniform time step $\Delta t$ or equivalently a sampling frequency $f_{\mathrm{samp}} = 1/\Delta t$. A time array $\{t_j = t(j)|\ j = 0, \dots, N-1\}$ is linked to the time series with the same time step, such that $t_j = t_0 + j\Delta t$. The number of samples on a timescale $T$ is simply $N = (T f_{\mathrm{samp}})^{-1}$.

The FT of the discrete signal $\tilde{x}(f_j)$ is obtained as follows [93]:

$$\tilde{x}(f_k) = \int_{t_0}^{t_0+T} dt\ x(t) e^{2\pi i f_k t}. \tag{2.2}$$

Under the change of variables $t' = t - t_0$. The expression reads:

$$\begin{aligned} \tilde{x}(f_k) &= e^{2\pi i t_0} \int_0^T dt'\ x(t'+t_0) e^{2\pi i f_k t'} && (2.3) \\ &\approx e^{2\pi i t_0} \Delta t \sum_{j=0}^{N-1} x_j e^{2\pi i \frac{jk}{N}} && (2.4) \\ &= e^{2\pi i t_0} \tilde{x}_k\ . && (2.5) \end{aligned}$$

where the integral has been replaced by the discrete sum, considering the discussion above.

Because the time series is discrete, the expression $\tilde{x}_k = \Delta t \sum_{j=0}^{N-1} x_j e^{2\pi i \frac{jk}{N}}$ is the discrete FT (DFT). The standard and optimized method for computing such an expression is to use the Fast Fourier Transform (FFT) [94]. It is worth noting that this method is valued for its computational speed and assumes that the input signal is periodic.

An oscillatory term is also present in Eq. (2.5). Its origin lies in the change of variable from $t$ to $t' + t_0$, as the time series is shifted by an initial time $t_0$. According to the time-shifting property, this shift results in a phase factor in the FT:

$$\int_{-\infty}^{+\infty} dt\ x(t-t_0) e^{2\pi i f t} = e^{-2\pi i f t_0} \tilde{x}(f)\ . \tag{2.6}$$

However, this additional factor will have no effect on our further discussion, as we will only consider the absolute value of the FT.

### 2.1.3 A major issue: spectral leakage

When working with a discretely sampled signal, two limitations arise in the computation of its FFT.

The first is the *Nyquist-Shannon sampling theorem* [95], which states that a signal sampled at a rate $f_s$ can only faithfully represent frequency components up to the Nyquist frequency $f_{\mathrm{N}} = f_s/2$. Any frequency content present above this threshold is folded back into the $[0, f_{\mathrm{N}}]$ range, corrupting the spectrum in a phenomenon known as aliasing. In the context of GW memory signals, this sets a fundamental upper bound on the accessible frequency range, and the sampling rate must therefore be chosen to adequately resolve the (maximum) frequency band of interest for a given detector. For instance, LISA targets the band $[10^{-4}, 10^{-1}]$ Hz, requiring a sampling rate of at least $f_s = 0.2$ Hz, while ET would operate in the band $[1, 10^3]$ Hz, requiring $f_s \geqslant 2$ kHz.

The second, and more important limitation for our work, is *spectral leakage* [96]. It arises from the finite duration of any signal. Computing the DFT of a signal of finite length $T$ is mathematically equivalent to multiplying an infinitely long signal by a rectangular window, that is, a function that is unity over $[0, T]$ and zero elsewhere. In the frequency domain, this multiplication corresponds to a convolution with the FT of the rectangular window, which takes the form of a sinc-like function with slowly decaying sidelobes. As a result, energy from any given frequency component is spread into neighboring frequency bins rather than being concentrated at a single spectral line. A clear example is provided for two periodic signals in Fig. 2.1, one of which has a frequency that matches the window to which the FFT is applied, while the other does not, resulting in spectral leakage. This is concerning for the GW memory effect. The signal has most of its energy concentrated at very low frequencies, with a spectrum decaying as $f^{-1}$. In this regime, spectral leakage distorts the estimated frequency content. Energy from the dominant low-frequency components leaks into higher frequency bins, artificially inflating the spectral amplitude in a frequency range most relevant for next-generation detectors.

Furthermore, the memory signal is intrinsically non-periodic causing further broadening and distorting the spectral estimate when computing the FFT (which assumes a periodic signal). Two complementary techniques are commonly employed to mitigate this effect, namely the application of padding and tapering.

## 2.2 Padding

Padding the signal simply means adding data points to the time series. There are several advantages to this method [93]:

- It broadens the frequency spectrum by lowering the minimum frequency, making it possible to investigate behavior at lower frequencies.
- The frequency bins are narrower. For example, zero-padding in the time domain corresponds to interpolation using a sinc function in the frequency domain. This does not mean that any new physical information is added to the signal when zero-padding.
- In terms of computational efficiency, it is recommended to pad the signal to a length that is a power of two of the original signal length [93]. This has little impact on our subsequent discussion.

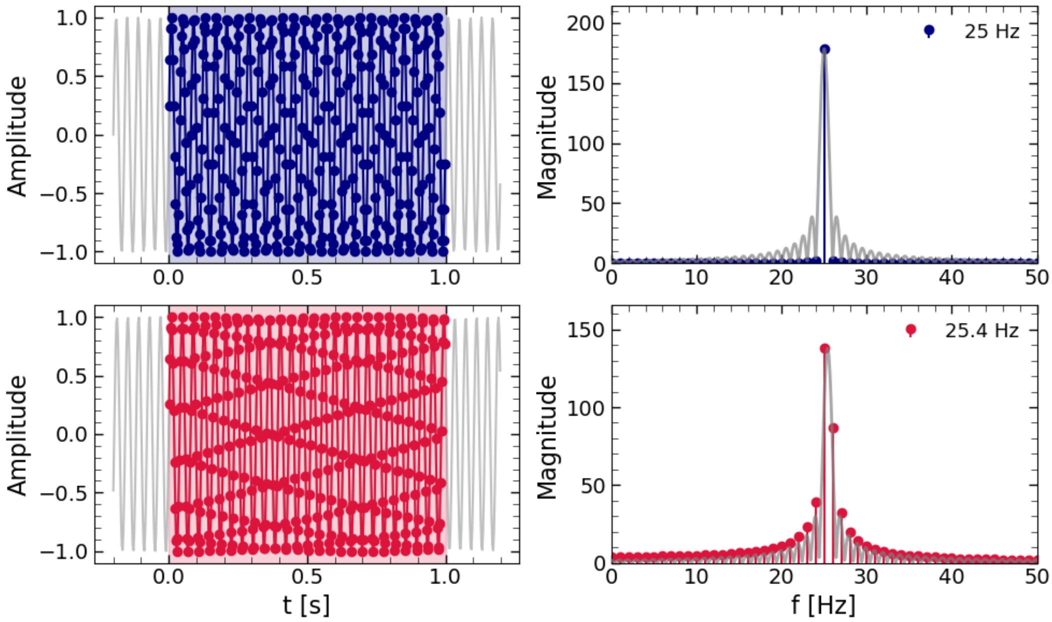


Figure 2.1: Illustration of spectral leakage for two sinusoidal signals at 25 Hz (blue) and 25.4 Hz (red), both sampled at $f_s = 500$ Hz. *Left*: Time domain of the two signal. The FFT is applied over the shaded time window, which contains an integer number of cycles of the 25 Hz signal but not the 25.4 Hz signal. *Right*: FFT of both signals. The 25 Hz component is resolved as a single spectral line, while the 25.4 Hz component exhibits spectral leakage. The grey curve is the sinc envelop from the rectangular window.

In the case of a memory signal, it is more interesting to pad the right part of the signal with the last non-zero value as it makes the signal more realistic (on top of the mentioned advantages). It is clearer to see the effect of padding directly in Fig. 2.2 where the parameter $r$ represents the fraction of the original signal's length used for padding.

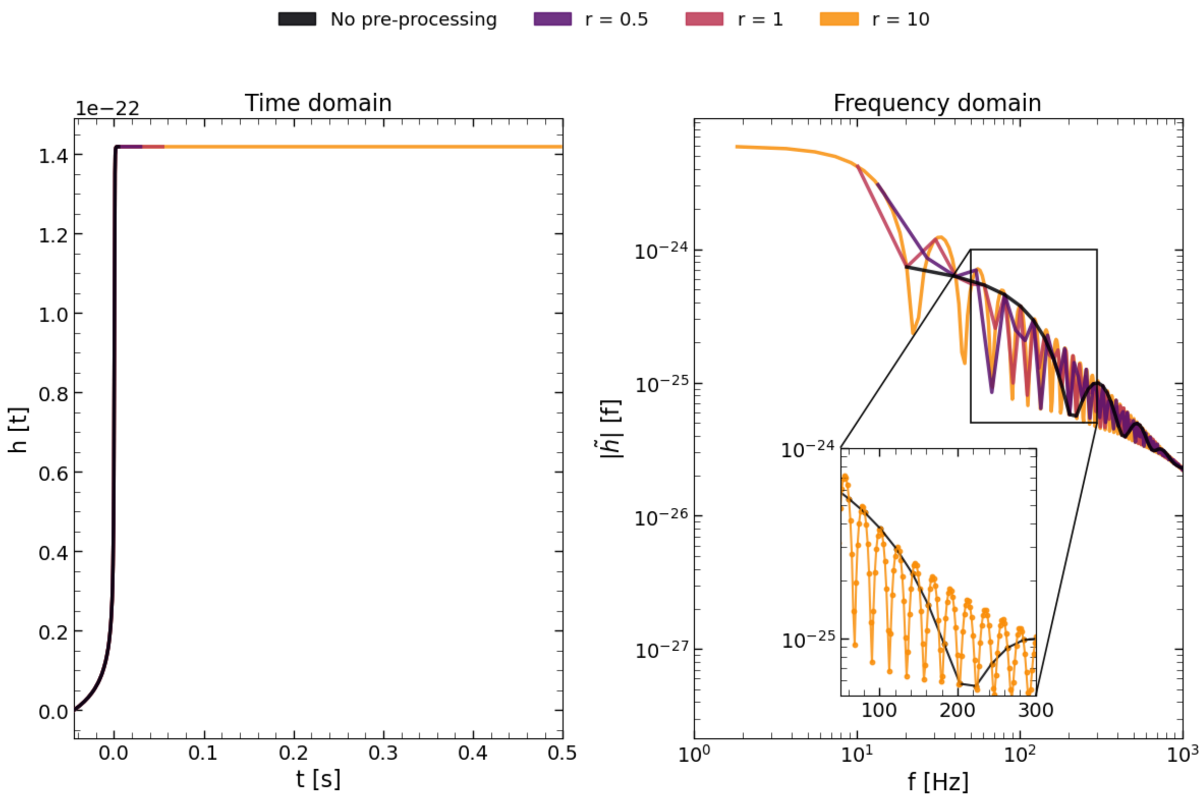


Figure 2.2: Padded memory for a system with equal masses and a total mass of $10M_\odot$ viewed edge-on (generated using `GWMemory` with the NRSur7dq2 approximant). The parameter $r$ represents the fraction of the original signal's length that is used to extend the signal. *Left:* Time domain padded signal. *Right:* FFT of the padded signal. Note that the signal starts at a lower frequency as the padding increases. A zoom-in of the region around 200 Hz is shown, where only the original signal (black) and the padded one (orange case) are displayed. It highlights the effect of padding on the width of the frequency bins as explained in the text.

## 2.3 Tapering

The step-function behavior of the memory effect means that the signal does not behave as assumed by the FFT, yet the method assumes that the signal is periodic. The rise behavior is interpreted as a discontinuity, which results in the appearance of artifacts and spectral leakage in the frequency domain. To reduce these artifacts, the use of a window is standard practice in signal analysis. A window function is simply a function that tapers off smoothly at the edges. By applying a window to the padded portion of the signal, the signal is brought back to zero. Since FFT requires a periodic signal, this method ensures the necessary periodicity for its application.

### 2.3.1 Planck & Tukey windows

Planck and Tukey windows are common taper-functions used for mitigating edge effects in GW signal analysis. An illustration of each of these windows, as well as a rectangular window can be found in Fig. 2.3. The Tukey (reps. Planck) window is parameterized by a shape parameter $\alpha \in [0, 1]$ ($\epsilon \in [0, 0.5]$) which controls the amount of tapering applied to the signal. The smaller the parameter, the faster the transition, and therefore the wider the constant plateau of the window. Concretely, the Tukey window

$\{w_t(j)|\ j = 0, \ldots, N-1\}$ is defined as:

$$w_t(j) = \begin{cases} \frac{1}{2}\left[1 - \cos\left(\frac{\pi}{\Delta(\alpha)} j\right)\right] & 0 \leqslant j \leqslant \Delta(\alpha) \\ 1 & \Delta(\alpha) \leqslant j \leqslant (N-1)/2 \\ w_t((N-1)-j) & (N-1)/2 < j \leqslant N-1 \end{cases} \tag{2.7}$$

where $\Delta(\alpha) = \alpha(N-1)/2$ is the width of the tapered region [93]. From the definition, the Tukey window is a cosine function that tapers the signal at the beginning and end. This window is twice differentiable [93].

The Planck window $\{w_p(j)|\ j = 0, \ldots, N-1\}$ is defined as:

$$w_p(j) = \begin{cases} 0 & j = 0 \\ \left[1 + e^{\left(\frac{\Delta(\epsilon)}{j} - \frac{\Delta(\epsilon)}{\Delta(\epsilon)-j}\right)}\right]^{-1} & 1 \leqslant j \leqslant \Delta(\epsilon) \\ 1 & \Delta(\epsilon) \leqslant j \leqslant (N-1)/2 \\ w_p((N-1)-j) & (N-1)/2 < j \leqslant N-1 \end{cases} \tag{2.8}$$

where $\Delta(\epsilon) = \epsilon(N-1)$ and acts similarly to $\Delta(\alpha)$ but is only defined for $\epsilon \in [0, 0.5]$. Contrary to the Tukey function, the Planck taper is continuously differentiable [93].

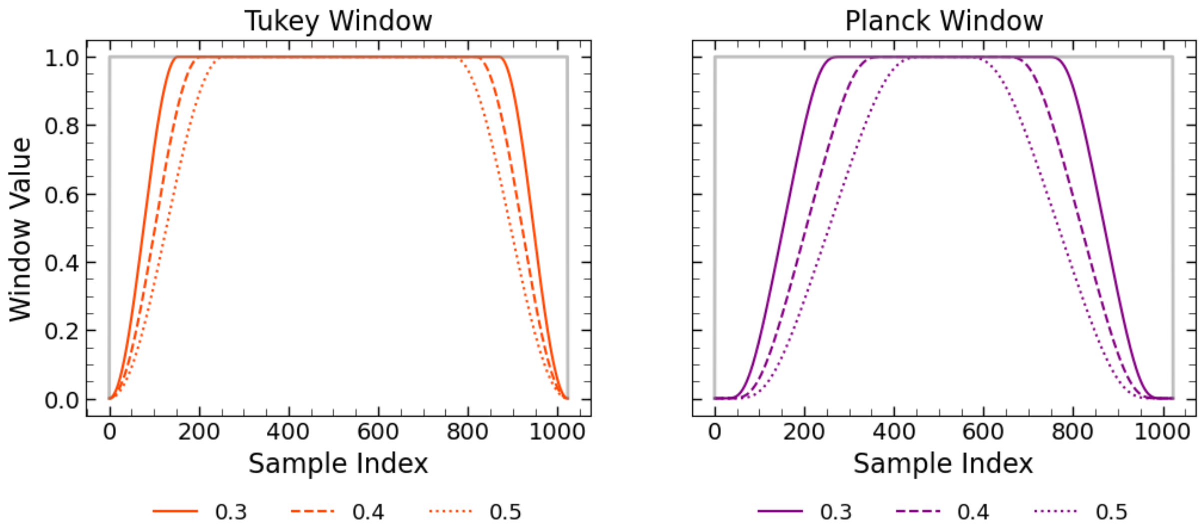


Figure 2.3: Comparison of the Tukey and Planck window for different values of $\alpha$ (orange) and $\epsilon$ (purple) respectively. A rectangular window (grey) is included for reference to highlight the smoothing effect of taper.

### 2.3.2 Impact on the spectral leakage

The frequency response of the Tukey, Planck and rectangular windows[1] is shown in Fig. 2.4, where the $y$-axis is expressed in decibels (dB), defined as:

$$\text{dB} = 20 \times \log_{10}\left(\frac{|A|}{|A_{\text{max}}|}\right) \tag{2.9}$$

[1]The window response can be viewed as the FT of a periodic signal with a frequency of 0 Hz. In this case, the product of the signal and the window is equal to the window itself, with a response centered at 0.

where $A$ is the FFT amplitude and $A_{\max}$ is its maximum amplitude. This normalized logarithmic scale is well suited to reveal the level of spectral leakage introduced by each window.

An ideal window would concentrate all the energy into a single sharp peak at the target frequency (here centered at 0) while completely suppressing the response at all other frequencies. In practice, no finite-duration window achieves this perfectly, there is always a trade-off between frequency resolution and spectral leakage. The rectangular window produces sharp discontinuities that generate strong oscillatory sidelobes in the frequency domain. As a result, energy is broadly spread across all frequency bins, leading to high spectral leakage as shown by the high level of the grey plot away from the peak.

Tapered windows reduce more efficiently the ampltiude of the sidelobes. This comes at the cost of a slightly broader peak compared to the rectangular window which translates into a poorer frequency resolution. However, this moderate loss of frequency resolution is an acceptable trade-off for the major reduction in spectral leakage.

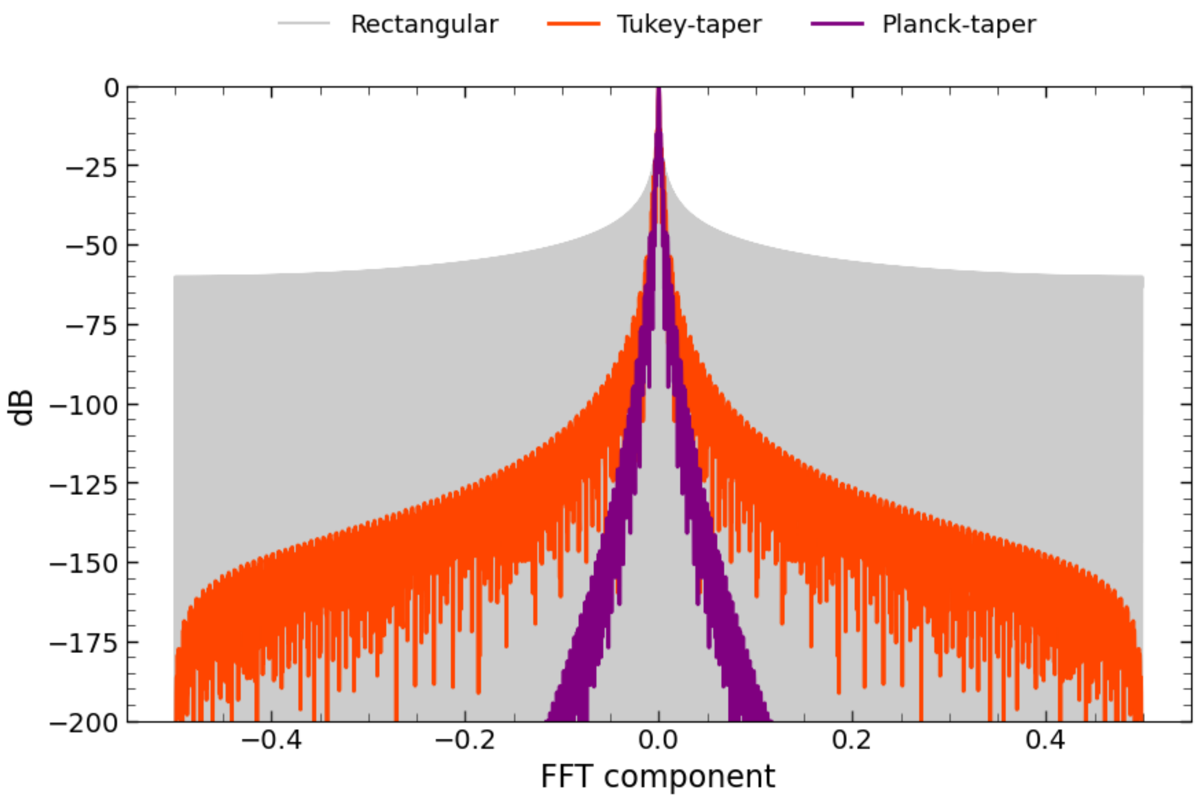


Figure 2.4: Comparison of the frequency responses (in dB) of the rectangular, Tukey-taper ($\alpha = 0.3$) and Planck-taper ($\epsilon = 0.3$) windows. The rectangular has high, slowly decaying side lobes, while the Tukey and the Planck-taper windows provide much stronger suppression of side lobes, reducing spectral leakage. The x-axis covers frequencies between $[-0.5f_s, 0.5f_s]$ or equivalently $[-f_\mathrm{N}, f_\mathrm{N}]$.

## 2.4 Effect on the memory signal

The effect of padding and the Tukey window is illustrated in Fig. 2.5 for a generic memory signal. In this figure and throughout the rest of the explanation, only the Tukey window will be used[2]. The trade-off between information loss and reduced spectral leakage represents the most balanced option.

Without any pre-processing (grey-curve), the spectrum decays slowly and exhibits spectral leakage across the frequency range as mentioned earlier. Applying zero-padding alone (purple) already improves the frequency resolution, though oscillatory sidelobes persist, explaining the oscillatory behavior of the decay. Combining padding with tapering suppresses these oscillations. Already at $\alpha = 0.3$, the sidelobes are reduced and the spectrum follows an expected[3] decay in $f^{-1}$, and a steeper one for high frequencies. The effect of further increasing $\alpha = 0.5$ (green) is shown in the inset with $\alpha = 0.4$ (blue): the two curves become nearly indistinguishable. Beyond a moderate value of $\alpha$, additional tapering yields no differences in terms of leakage reduction.

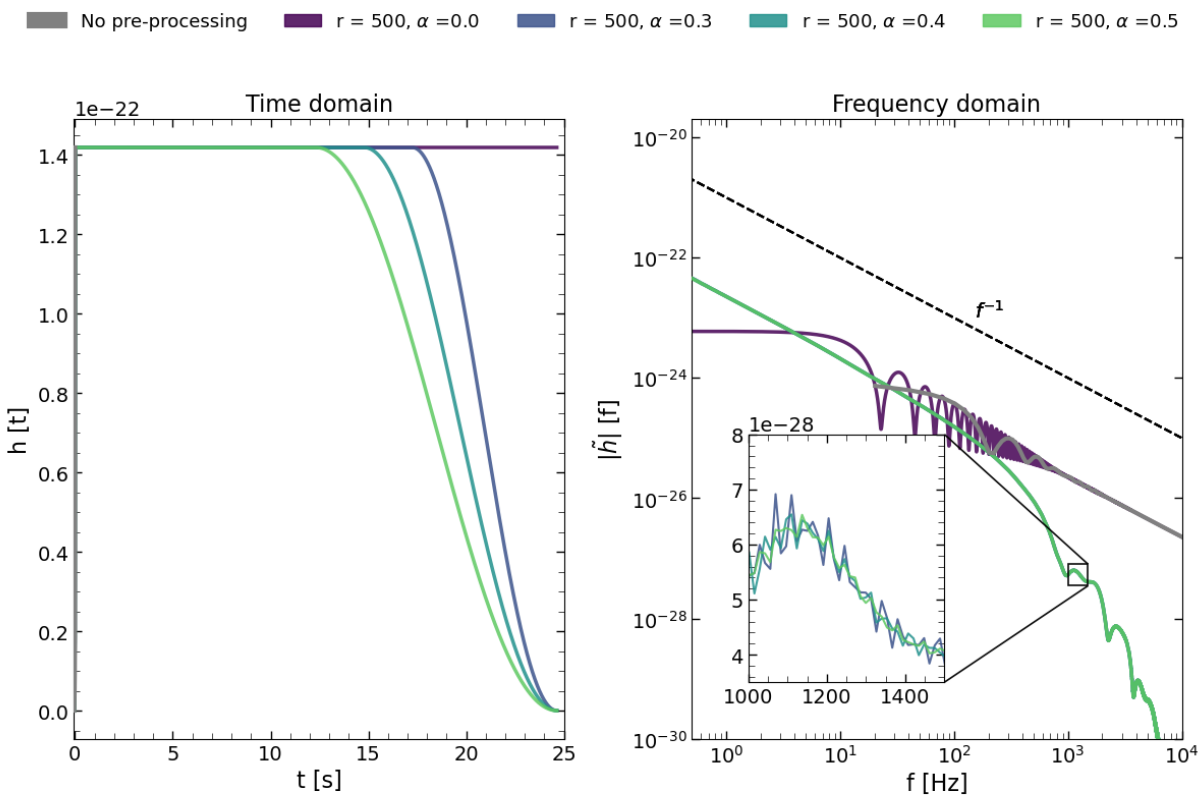


Figure 2.5: Effect of padding ($r = 500$) and Tukey windowing on the time-domain profile (*left*) and frequency-domain spectrum (*right*) of a GW memory with the same parameters as in Fig. 2.2. The inset shows a zoom into the high-frequency region (1000 - 1500 Hz) highlighting the negligible difference between $\alpha = 0.4$ and $\alpha = 0.5$.

[2]The use of the Planck window on a memory signal is displayed in the appendix A.4.
[3]Given the discussion on the FT of the Heaviside function.

## 2.5 Detectability

### 2.5.1 Spectrogram

A practical and visually appealing way to identify a GW is to construct a spectrogram, i.e., a time-frequency plot of the strain. For a CBC, the signal frequency increases and reaches its peak at the moment of merger. The signature on a spectrogram is then a sharply rising curve known as the chirp. Based on the frequency evolution of the signal during the inspiral phase, we can derive information about the source, such as the mass of each progenitor ($m_1$ and $m_2$) through the chirp mass $\mathcal{M}$:

$$\mathcal{M} = \frac{(m_1 m_2)^{3/5}}{(m_1 + m_2)^{1/5}} = \frac{c^3}{G}\left(\frac{5}{96}\pi^{-8/3} f^{-11/3} \dot{f}\right)^{3/5}. \tag{2.10}$$

where the dot refers to the temporal derivative.

However, in this section we are more interested in the nonlinear[4] memory signature embedded in the chirp. The memory will appear at lower frequencies and with a very different frequency response. As the memory begins to rise, the frequency rises as well, and it eventually drops back down if a window is applied to the signal. In a spectrogram, the memory then appears as a rectangle at low frequencies as in Fig. 2.6.

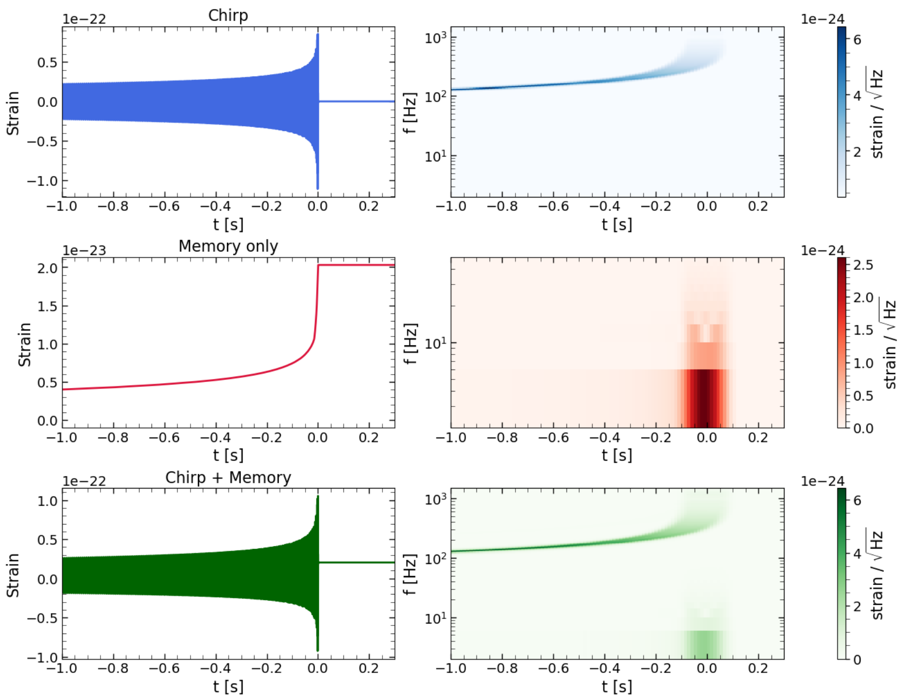


Figure 2.6: Spectrograms showing a CBC signal without memory effect (blue), a memory-only signal (red) generated with the approximant NRHybSur3dq8 of `GWMemory`, and a combination of the two (green). The system has a total mass of $3M_\odot$ and a mass ratio $q = 1$, observed edge-on at a distance of 100 Mpc. *Left:* Time-domain or each signal. *Right:* Spectrograms obtained with scipy_spectrogram method where the signal is first padded and then tapered with a Tukey window ($\alpha = 0.6$).

[4]The temporal evolution of nonlinear memory is correlated with the inspiral and merger phases, making its spectrogram signature "predictable" and identifiable. The linear memory, by contrast, is more source-dependent in both amplitude and timing, and is subdominant for CBC sources, making it less suited to the simplified analysis presented here.

Based on the spectrogram, we can develop a simple method to identify the memory effect. Suppose we have an oscillatory signal reconstructed using an approximant that does not contain the memory effect, which is the case for nearly all available approximations[5]. By subtracting this spectrogram from the one containing the oscillatory signal and memory (computed separately), we should obtain an artifact caused by the presence of memory around the merger. Such a result is shown in Fig. 2.7 where spectral leakage corrupts the left panel. On the right panel, three regions of interest are highlighted:

- Late inspiral accumulation: The region reflects the monotonic accumulation of the nonlinear memory during the inspiral phase. The memory build-up is faint, appearing as a diffuse low-frequency excess in the residual.
- Merger/ringdown: The most prominent feature appears concentrated near the merger. It corresponds to the rapid rise of the nonlinear memory, where the bulk of the nonlinear memory is produced.
- Chirp discrepancy: This feature is an artifact rather than a memory signature. It happens from a slight mismatch between the two spectrograms in the chirp region, likely due to the windowing or spectral leakage. The small mismatch results in these bands located at high frequency compared to the memory.

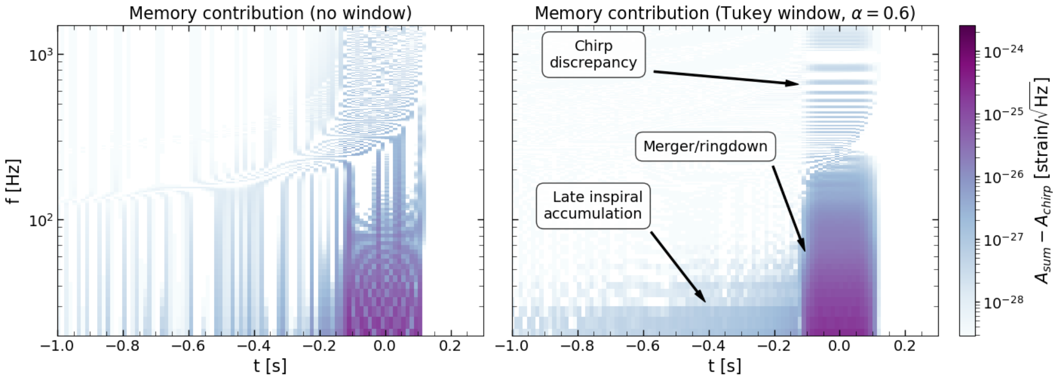


Figure 2.7: Residual spectrogram of a waveform with ($A_{\text{sum}}$) and without ($A_{\text{chrip}}$) nonlinear memory for the same parameters as in Fig. 2.6. *Left:* Spectrogram without tapering. The frequency content is widely spread in frequency due to spectral leakage. *Right:* Same spectrogram with the application of a Tukey window, reducing the numerical artifact. Three residual regions are identified and explained in the text above.

However, this approach remains a purely illustrative exercise performed on noise-free theoretical signals. A more robust strategy would consist of using an approximant that incorporates the memory memory effect (such as NRHybSur3dq8_CCE [91]) to generate the full waveform, and comparing the source parameters recovered by this approximant with those obtained from a memory-free one. The difference in the reconstructed parameters would then serve as an indirect probe of the memory contribution. An analysis via a $\chi^2$ or a Bayesian parameter estimation framework would provide more rigorous implementation of this idea. This analysis represents a perspective for subsequent work.

The subtraction method can also be approached from another perspective. Consider a spectrogram of a realistic detector output, contaminated by instrumental noise and other disturbances, from which the theoretical waveform of the same signal without a memory

[5]Except for NRHybSur3dq8_CCE but it is still relatively recent (2023) [91].

contribution is subtracted. If the residual spectrogram exhibits features consistent with a memory signature, the effect has been effectively isolated. This remains, however, a highly idealized scenario. In current detectors, the memory signal is buried beneath the noise floor and is far below the detection threshold.

### 2.5.2 Signal-to-noise ratio

Obtaining the correct frequency response of the memory effect is a first step toward detectability. In particular, we can quantify how the memory signal stands out from the noise by computing the signal-to-noise ratio (SNR). This SNR varies from detector to detector, as each has a different sensitivity and specific characteristics at certain frequencies. The SNR for a detector is defined as [5]:

**Memory SNR**

$$\mathrm{SNR} = \left[\int_0^{+\infty} \mathrm{d}\ln \mathrm{f}\ \frac{\mathrm{h_c^2(f)}}{\mathrm{h_n^2(f)}}\right]^{1/2}, \tag{2.11}$$

where:

- $h_c$ is the characteristic strain of the signal defined as $h_c = 2f|\tilde{h}|$.
- $h_n$ represents the sky-average rms noise amplitude for a detector with noise spectral density $S_n(f)$, defined as $h_n = \sqrt{f S_n(f)}$.

The detectability of a signal is visually assessed by comparing the characteristic strain with the detector sensitivity curve on a log-log plot. A signal whose characteristic strain lies above the sensitivity curve (over a broad frequency range) will accumulate a higher SNR and thus be more readily detectable. Conversely, a signal whose $h_c$ remains below the sensitivity curve at all frequencies will be undetectable compared to the expected noise level in the detector.

For memory detection from BBH mergers, SNR thresholds have been estimated for LISA [97]: $\mathrm{SNR_{mem}} > 3$ represents the minimum threshold for claiming detection of the memory, while $\mathrm{SNR_{mem}} > 5$ ensures a more robust detectability regardless of noise realization. For ET, a detection requires an SNR threshold larger than 8.

Unlike BBH mergers, which may individually exceed these SNR thresholds, BNS systems suffer from lower masses that reduce the memory amplitude. However, the mass ejection process and the (possible) GRB formation in BNS introduce supplementary memory contributions that may increase the total signal amplitude, potentially enhancing the resulting SNR. Consequently, a prerequisite study dedicated to the modeling of the (linear) memory of BNS counterpart is first conducted in the next chapter. It provides the necessary basics to investigate, in our last chapter, whether these memory signatures allow individual events to reach SNR thresholds, while identifying the optimal BNS configurations for detection by LISA and ET.

Chapter 3

# On the linear memory effect in BNS events

The pre-processing methods discussed in the previous chapter are essential when working with numerically generated signals. However, when starting from analytical models for the linear memory, this issue does not occur. The frequency response is obtained by directly computing the FT of the model function, bypassing any numerical artifact. The chapter exploits the analytical tractability to characterize the linear memory from ejecta components of a BNS merger, namely the dynamical and post-merger (wind-driven) ejecta, the GRB and the kilonova emission. Only pre-processing methods will be used for the kilonova case, as its memory effect will be determined based on a simulation of AT2017gfo. The evolution of the memory signal will be illustrated in the temporal and frequency domains, with particular emphasis on the frequency representation as it allows for direct comparison with detector sensitivity and thus detectability.

## 3.1 Toy model of the linear memory

In this part, we consider the contributions from dynamical and disk wind ejecta, as well as the emission from GRBs, including both the prompt and afterglow phases in order to compute the linear memory according to Eq. (1.62).

Furthermore, we do not want to use a Heaviside function that contains no physical information about the rising phase. The complexity involved in tracking these parameters for realistic ejecta distributions can be avoided by employing a toy-model that captures the essential physics while remaining computationally tractable. The model is thus a simplified representation of the expected signal, nevertheless the frequency response exhibits the characteristic $f^{-1}$ decay demonstrated in the previous chapter.

### 3.1.1 Temporal profile

In this approach, the temporal evolution of the memory is governed by a step function $s(t, \tau)$ that describes how the memory signal rises from zero to its saturated value $\Delta h$ as material becomes unbound. This evolution begins at $t = t_{\text{start}}$, the time when ejecta acceleration begins[1]. Before this $t_{\text{start}}$, no mass has been ejected yet, and the linear memory amplitude is identically zero.

[1]Throughout this work, the merger time defines our temporal reference frame, set at $t = 0$.

The model is characterized by a rise time $\tau$, which represents the typical timescale over which the memory signal increases from its initial value to its asymptotic plateau. Physically, $\tau$ corresponds to the duration of the ejection and acceleration phase. Once $t > \tau$, all ejecta have reached their terminal velocities and the memory has saturated at its maximum amplitude $\Delta h$.

The angular dependence of the signal is encoded in the function $\Theta(\theta)$, which accounts for the observer's viewing angle $\theta$ relative to the ejecta symmetry axis. This function modulates the memory amplitude according to the anisotropy of the mass-energy ejection. We discuss its specific form in a further section.

Combining these elements, we define our phenomenological model for the linear memory effect as:

**Phenomenological model**

$$h(t,r,\theta) = \begin{cases} 0 & t \leqslant t_{\text{start}} \\ \Delta h(r)\,\Theta(\theta)\,s(t,\tau) & t_{\text{start}} < t \leqslant \tau \\ \Delta h(r)\,\Theta(\theta) & t > \tau \end{cases} \tag{3.1}$$

where $\Delta h(r)$ encodes the distance-dependent amplitude, $\Theta(\theta)$ captures the angular observing pattern, and $s(t,\tau)$ describes the temporal rise profile.

Several definitions for the step function $s(t,\tau)$ exist, whose general behaviors are similar, differing only in the mathematical modeling of the jump. We adopt the following ones, illustrated in the left panel of Fig. 3.1:

$$s(t,\tau) = \begin{cases} 2\left[\left(1 + e^{-t/\tau}\right)^{-1} - \dfrac{1}{2}\right] & : \text{ exponential [77]} \\ \dfrac{t}{\tau} & : \text{ uniform [98]} \end{cases} \tag{3.2}$$

### 3.1.2 Frequency profile

The frequency evolution of the memory signal is obtained by taking the FT of the signal $\tilde{h}$ defined as

$$\tilde{h}(f) = \int_{-\infty}^{+\infty} h(t) e^{2\pi i f t}\, dt. \tag{3.3}$$

Given the temporal dependence of $h(t,r,\theta)$, it is equivalent to calculating the FT of $s(t,\tau)$. If we neglect the Dirac delta at $f = 0$, we find the analytical expression of the FT of each model:

$$\tilde{s}(f) = \begin{cases} \dfrac{\pi\tau}{2i\sinh(\pi f \tau)} & : \text{ exponential [77]} \\ \dfrac{1}{2\sqrt{2}\pi f^2 \tau}\left[1 - \cos(2\pi f\tau)\right]^{1/2} & : \text{ uniform [98]} \end{cases} \tag{3.4}$$

Note that $|\tilde{h}| = \Delta h |\tilde{s}| \sim f^{-1}$ for $f \ll 1/\tau$ for both models. The low-frequency behavior is then similar to the FT of a Heaviside function, which is not surprising given that these frequencies probe the evolution over time intervals longer than the rising phase. Rather

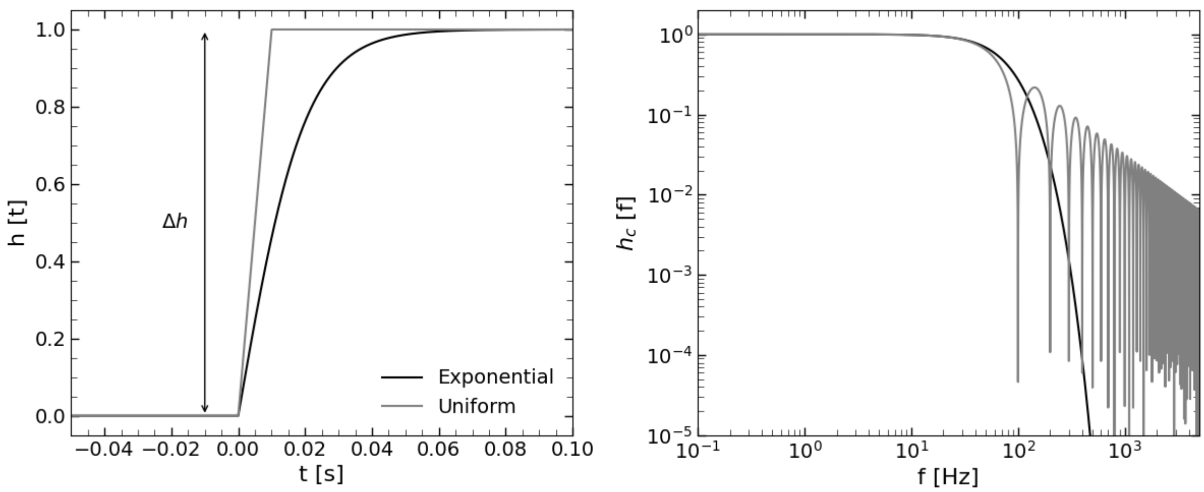


Figure 3.1: Comparison of time-domain and frequency-domain memory models for $\tau = 0.01s$, $\Delta h = 1$ and $\Theta(\theta) = 1$. *Left*: Time evolution of the memory signal for exponential (black) and uniform (grey) rise models. *Right*: Corresponding characteristic strain $h_c(f)$ in the frequency domain.

than $|\tilde{h}(f)|$, it is more convenient to compute the characteristic strain $h_c = 2f|\tilde{h}|$, which allows direct comparison with the sensitivity curve and the SNR of a detector [98]. A representation of each model is shown in the right panel of Fig. 3.1.

A noticeable difference between the two models in the frequency domain is the appearance of minima during the decay of the uniform model. These arise from the factor $1 - \cos(2\pi f \tau)$ which cancels out for values of $f = k/\tau$, for any integer $k$. Physically, the terms are attributed to the two sharp corners in the time domain, at the onset and end of the rise phase, the last of which act as the source of oscillatory contributions in frequency space. The resulting spectrum manifests a decaying envelope modulated by these periodic oscillations. By contrast, the exponential model exhibits a smooth, continuously differentiable temporal rise, yielding a featureless and monotonically decaying spectrum.

In Fig. 3.2, the impact of the inverse of the characteristic time is illustrated. The frequency behavior of the characteristic strain can be divided into two regimes. First a constant part for $f \lesssim f_\tau = 1/\tau$, followed by a decrease as $f^{-1}$ for $f \gtrsim f_\tau$. Hence, the inverse of the characteristic time acts as an indication of the maximum frequency at which the memory signal is potentially detectable. For example, an ejecta with a rise time $\tau \lesssim 10^{-2}$s will be within LIGO's sensitive band around a frequency of 100 Hz.

## 3.2 Angular factor

The magnitude of the memory effect depends on the observer's location through the angular structure of the transverse-traceless projection in Eq. (1.62):

$$\Delta h_{ij}^{\mathrm{TT}}(t,r) = \frac{4}{r}\Delta \sum_{A=1}^{N} \left[ \frac{m_A}{\sqrt{1-v_A^2}} \left( \frac{v_A^i v_A^j}{1-\mathbf{n}\cdot\mathbf{v}_A} \right) \right]^{\mathrm{TT}} . \tag{3.5}$$

For ejecta moving radially outward with velocity $\mathbf{v}_A = v_A \hat{n}_A$ (where $\hat{n}_A$ is the ejection

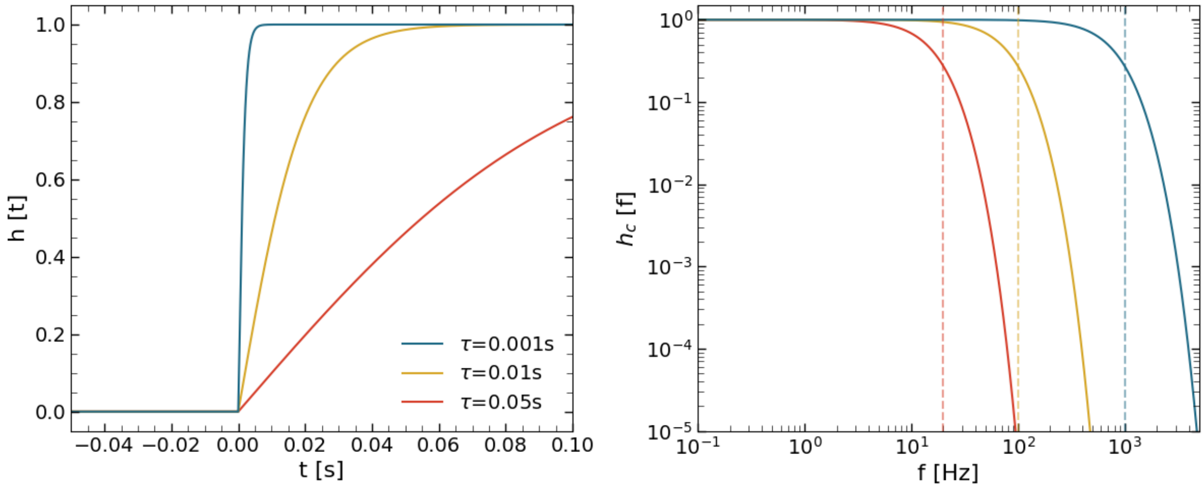


Figure 3.2: Impact of timescale $\tau$ on memory waveforms and characteristic strain $h_c$ for the exponential toy model with $\Delta h = 1$, $\Theta(\theta) = 1$ and $t_{\text{start}} = 0$. *Left:* Temporal evolution of the linear memory effect. *Right:* Characteristic strain of the associated linear memory. The dotted lines refers to the inverse of the characteristic times, highlighting where the frequency starts to drop.

direction), this simplifies to:

$$\Delta h_{ij}^{\text{TT}}(t,r) = \frac{4}{r}\Delta \sum_{A=1}^{N} \frac{m_A v_A^2}{\sqrt{1-v_A^2}} \frac{[n_A^i n_A^j]^{\text{TT}}}{1-\beta_A \cos\theta_A} \;, \tag{3.6}$$

where $\beta_A = v_A/c$ and $\theta_A$ is the angle between the ejecta direction $\hat{n}_A$ and the line of sight to the observer $\hat{n}$.

The key quantity to evaluate is the TT projection $[n_A^i n_A^j]^{\text{TT}}$, which encodes a first angular dependence of the memory signal, the other being the term $(1 - \beta_A \cos\theta_A)^{-1}$. To compute this projection analytically, we adopt the coordinate system illustrated in Fig. 3.3.

### 3.2.1 Computation of TT amplitude

#### Coordinate system and unit vectors

To evaluate the angular dependence of the memory effect from a given ejecta, we must compute the TT projection of the tensor $n^i n^j$. To do so, we follow the approach of [99], working in the coordinate system illustrated in Fig. 3.3. The unit vectors pointing toward the ejecta element and toward the observer are defined as:

$$\hat{n} = \frac{\vec{x}'}{|\vec{x}'|} \;, \tag{3.7}$$

$$\hat{n}' = \frac{\vec{x} - \vec{x}'}{|\vec{x} - \vec{x}'|} \;, \tag{3.8}$$

In the $(X, Y, Z)$ frame, these vectors have components:

$$\hat{n}: \quad n_x = \sin\theta\cos\phi, \quad n_y = \sin\theta\sin\phi, \quad n_z = \cos\theta, \tag{3.9}$$

$$\hat{n}': \quad n'_x = -\sin\psi\cos\phi, \quad n'_y = -\sin\psi\sin\phi, \quad n'_z = \cos\psi. \tag{3.10}$$

Notably, we obtain the scalar product:

$$\hat{n}\cdot\hat{n}' = \cos(\theta+\psi). \tag{3.11}$$

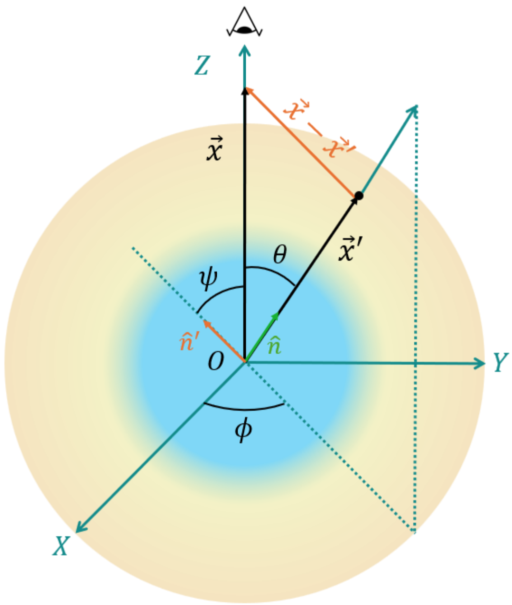


Figure 3.3: Geometric configuration for the angular effect calculation. The coordinate system $(X, Y, Z)$ (teal) is centered at the merger location $O$, with the $Z$-axis aligned with the orbital angular momentum. The observer is located at large distance along direction $Z$ and position $\vec{x}$. An ejecta element at position $\vec{x}'$ is described by angles $\theta$, $\phi$ and $\psi$ relative to the coordinate axes. The normal vectors $\hat{n}$ (green) and $\hat{n}'$ (orange) denote the orientation of the ejecta and the relative position $\vec{x}-\vec{x}'$(compared to the observer one) respectively. Inspired by Figure 10 of [99].

### TT projection

Next, we need to calculate the TT gauge contribution. We must therefore determine the expression of the projector $P_{ij}$ (defined in Eq. (1.35)) and the TT projector $\Lambda_{ij,kl}$ (Eq. (1.36)) constructed with $\hat{n}'$. We need to compute the expression:

$$[n^i n^j]^{\mathrm{TT}} \equiv \Lambda_{ij,kl}(n^k n^l) = \left(P^i_k P^j_l - \frac{1}{2}P^{ij}P_{kl}\right) n^k n^l = P^i_k n^k n^l P^j_l - \frac{1}{2}P^{ij}P_{kl}n^k n^l \ . \quad (3.12)$$

We demonstrate the calculation explicitly for the $xx$ component, the other components follow analogously. We compute each term in Eq. (3.12) separately.

1. The first term $P^x_k n^k$ reads:

$$P^x_k n^k = (\delta^x_k - n'^x n'_k)n^k = n^x - n'^x \cos(\theta+\psi) \quad (3.13)$$
$$= \sin\theta\cos\phi + \sin\psi\cos\phi\cos(\theta+\psi) \quad (3.14)$$
$$\iff P^x_k n^k = \cos\psi\cos\phi\sin(\theta+\psi). \quad (3.15)$$

2. We then obtain the following expressions for $P_{kl}n^k n^l$:

$$P_{kl}n^k n^l = (\delta_{kl} - n'_k n'_l)n^k n^l = 1 - \cos^2(\theta+\psi) \quad (3.16)$$
$$\iff P_{kl}n^k n^l = \sin^2(\theta+\psi). \quad (3.17)$$

3. Finally, we also need $P^{xx}$:

$$P^{xx} = (\delta^{xx} - n'^x n'^x) = 1 - \sin^2\psi\cos^2\phi. \quad (3.18)$$

All the terms needed to calculate $(n^x n^x)^{\mathrm{TT}}$ are now available in Eq. (3.15), Eq. (3.17) and Eq. (3.18). Inserting the previous expressions in Eq. (3.12), we obtain [99]:

$$[n^x n^x]^{\mathrm{TT}} = \frac{1}{2}\sin^2(\psi+\theta)\left[\cos^2\phi\,(1+\cos^2\psi)-1\right]. \tag{3.19}$$

For an observer at infinity ($r \to \infty$), the angle $\psi \to 0$, corresponding to the ejecta and observer directions becoming parallel in the transverse plane [99]. Setting $\psi = 0$:

$$[n^x n^x]^{\mathrm{TT}} = \frac{1}{2}\sin^2\theta\,(2\cos^2\phi - 1) = \frac{1}{2}\sin^2\theta\cos 2\phi. \tag{3.20}$$

By an analogous calculation for the off-diagonal component [99]:

$$[n^x n^y]^{\mathrm{TT}} = \frac{1}{2}\sin^2\theta\sin 2\phi. \tag{3.21}$$

These expressions define the TT factor for the components $h_+$ and $h_\times$, respectively, as $h_{xx}^{\mathrm{TT}} = h_+^{TT}$ and $h_{xy}^{\mathrm{TT}} = h_\times^{TT}$ [99].

### 3.2.2 General and asymptotic behavior

Consider a more general case where the observer is off-axis with an inclination $\iota$ relative to the Pole. In this case, the angle $\theta$ must be replaced by the relative angle between the observer and the ejecta, $\theta_{\mathrm{ej}}$. If $\theta$ refers as before to the angle between the North Pole and the ejecta, then $\theta_{\mathrm{ej}} = \theta - \iota$. The same applies to $\phi$. From the derivation above and the linear memory formula Eq. (1.62), we finally find the complete angular factors:

$$\Theta(\theta_{\mathrm{ej}}, \phi_{\mathrm{ej}}) = \begin{cases} \Theta_+(\theta_{\mathrm{ej}}, \phi_{\mathrm{ej}}) = \dfrac{\sin^2\theta_{\mathrm{ej}}}{1-\beta\cos\theta_{\mathrm{ej}}}\ \cos 2\phi_{\mathrm{ej}} \\ \Theta_\times(\theta_{\mathrm{ej}}, \phi_{\mathrm{ej}}) = \dfrac{\sin^2\theta_{\mathrm{ej}}}{1-\beta\cos\theta_{\mathrm{ej}}}\ \sin 2\phi_{\mathrm{ej}} \end{cases} \tag{3.22}$$

where $\Theta_{+,\times}$ denotes the angular factor for the $+$, $\times$ polarization modes.

We assume henceforth that each ejecta component can be modeled as emission within a non-precessing axisymmetric cone, with the symmetry axis perpendicular to the $xy$-plane in which the azimuthal angle is defined. Under this assumption, the azimuthal dependence averages to zero when integrated over the source, and the amplitude for both polarizations reduces to:

$$\Theta(\theta_{\mathrm{ej}}) = \frac{\sin^2\theta_{\mathrm{ej}}}{1-\beta\cos\theta_{\mathrm{ej}}}\ . \tag{3.23}$$

The angular dependence encoded in $\Theta(\theta_{\mathrm{ej}})$ reveals how the memory signal varies with viewing geometry and velocity of the source (Fig. 3.4). For non-relativistic sources ($\beta \ll 1$), the memory amplitude peaks in edge-on configuration. As the source velocity increases, however, this maximum shifts toward smaller angles, approaching a face-on geometry. This behavior reflects relativistic beaming: radiation becomes increasingly concentrated along the direction of motion within a characteristic opening angle $\Gamma^{-1} = \sqrt{1-\beta^2}$ where $\Gamma$ denotes the Lorentz factor.

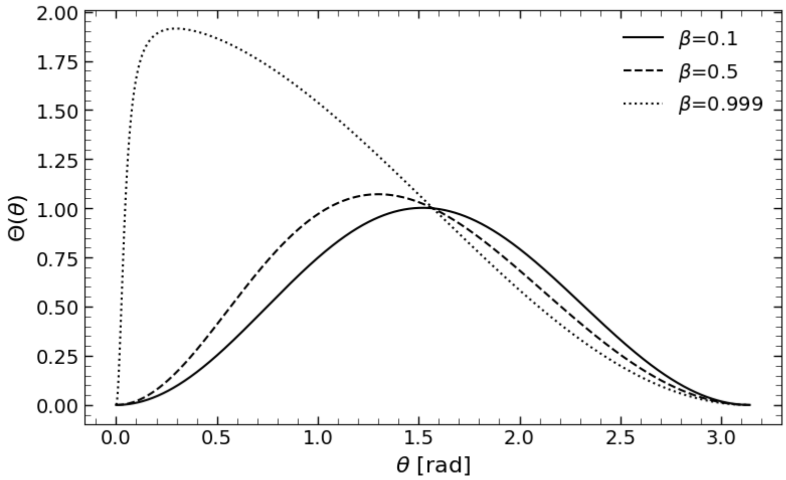


Figure 3.4: Behavior of the angular factor $\Theta(\theta_{\rm ej})$ for different values of $\beta = v_{\rm ej}/c$.

To understand this effect quantitatively, we examine the asymptotic behavior of $\Theta(\theta_{\rm ej})$ in the ultra-relativistic limit ($\Gamma \gg 1$, $\theta_{\rm ej} \ll 1$) [14]. Expanding the numerator and denominator in $\theta_{\rm ej}$ yields:

$$\sin^2\theta_{\rm ej} \simeq \theta_{\rm ej}^2, \tag{3.24}$$

$$1-\beta\cos\theta_{\rm ej} \simeq 1-\beta\left(1-\frac{\theta_{\rm ej}^2}{2}\right) = (1-\beta)+\frac{\beta\theta_{\rm ej}^2}{2}. \tag{3.25}$$

For ultra-relativistic velocities ($\beta \sim 1, \Gamma \gg 1$), the relation between the Lorentz factor and $\beta$ simplifies to:

$$\beta = \sqrt{1-\Gamma^{-2}} \simeq 1-\frac{1}{2\Gamma^2}, \tag{3.26}$$

such that $1-\beta \simeq \Gamma^{-2}/2$. Substituting into $\Theta(\theta)$ Eq. (3.23), we obtain the asymptotic form:

$$\Theta(\theta_{\rm ej}) = \frac{\sin^2\theta_{\rm ej}}{1-\beta\cos\theta_{\rm ej}} \simeq \frac{2\theta_{\rm ej}^2}{\Gamma^{-2}+\theta_{\rm ej}^2}. \tag{3.27}$$

This expression, plotted in the left panel of Fig. 3.5, shows that the signal peaks at $\theta_{\rm ej} \sim \Gamma^{-1}$ and decreases for smaller angles ($\theta \ll \Gamma^{-1}$). Moreover, for $\theta_{\rm ej} \gg \Gamma^{-1}$, the expression reduces to:

$$\Theta(\theta_{\rm ej}) \simeq 1+\cos\theta_{\rm ej}\ , \tag{3.28}$$

and the memory also decreases in the case of larger angles.

This angular effect is called the *anti-beaming effect* [99]. Memory is maximum edge-on and, in the case of relativistic beaming, it is suppressed within a very narrow cone (of aperture $\Gamma^{-1}$) around the axis, and is maximum just outside the edge of the cone, then the amplitude decreases for larger viewing angles. This behavior is illustrated below in Fig. 3.5.

Finally, for the sake of clarity we will no longer use the notation $\Theta(\theta_{\rm ej})$ anymore but rather $\Theta(\theta)$ where the argument is still the relative angle between the ejecta and the observer. Since we are in good company, the argument $\theta$ will be either this relative angle or the polar angle, depending on the context in which it is used.

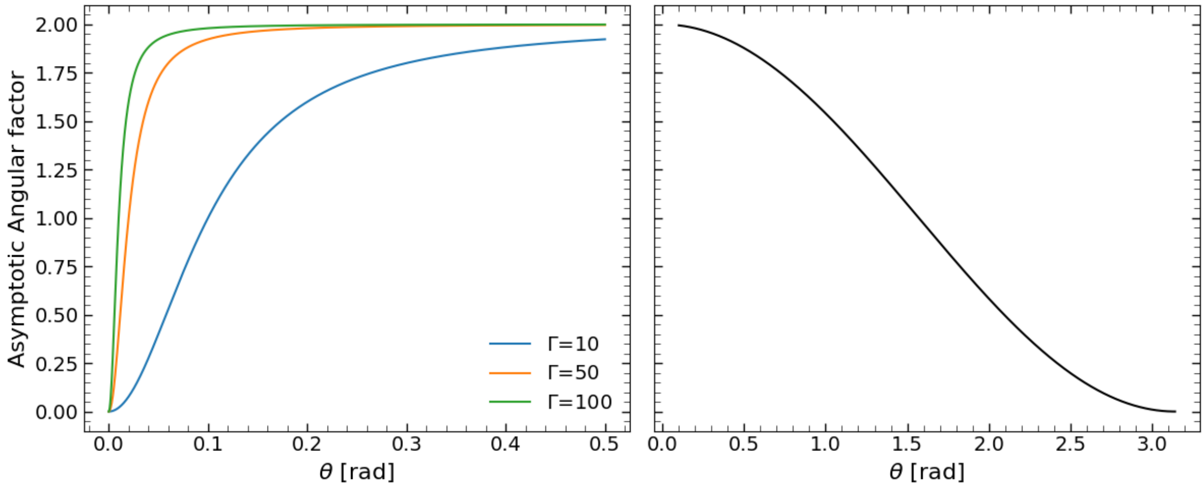


Figure 3.5: Asymptotic values of the angular function $\Theta(\theta_{\rm ej})$ for $\theta_{\rm ej} \ll \Gamma^{-1}$ (left) and for $\theta_{\rm ej} \gg \Gamma^{-1}$ (right). For the right panel, only the function $\Theta(\theta_{\rm ej}) = 1 + \cos\theta_{\rm ej}$ is plotted as it does not dependent on $\Gamma$.

## 3.3 Dynamical and Wind ejecta

The merger of NSs expels a large amount of matter at a speed of around 10% of the speed of light. This ejected matter is labeled as dynamical ejecta or wind ejecta depending on its source, as described in the introduction. Since the material is unbound and ejected anisotropically at high velocities, it produces a linear memory effect. To give an order of magnitude for the main properties of these ejecta, Table 3.1 contains the minimum and maximum values based on magnetohydrodynamics simulations. Moreover, the start time for the dynamical component is arbitrarily defined as the moment when the signal reaches half its saturated value at merger[2]. As the matter is tidally stripped during the late inspiral (few ms before the merger), the precise onset is not well constrained, hence our estimate.

Table 3.1: Properties of the ejecta components in a standard BNS [100]

| | Dynamical | | Disk wind | |
|---|---|---|---|---|
| Property | Value | Unit | Value | Unit |
| Mass | $(0.01\text{–}1) \times 10^{-2}$ | $M_\odot$ | $10^{-3}\text{–}10^{-2}$ | $M_\odot$ |
| Velocity | 0.1–0.4 | $c$ | 0.1–0.2 | $c$ |
| Rise time ($\tau$) | $10^{-2}$ | s | 1–10 | s |
| Start time | $-\tau \times \ln 3$ | ms | $10^{-2}$ | s |
| Geometry | Equatorial | | Polar ($\lvert\theta\rvert \lesssim 30^\circ$) | |

**Note:** The merger defines the start time (t=0).

The amplitude of the signal $\Delta h$ is approximated from the general formula Eq. (1.62) by assuming a radially ejected point mass $M_{\rm ej}$ with velocity $v_{\rm ej}$ and $\beta = v_{\rm ej}/c$, and is given by[3]:

$$\Delta h_{\rm dyn/wind} = \frac{2M_{\rm ej}v_{\rm ej}^2}{r}\,\Theta(\theta) \tag{3.29}$$

[2]For the exponential model, the memory is at half its maximum value at $t = 0$ if it starts at time $-\tau \times \ln 3$.

[3]The first factor is the maximum memory amplitude from Eq. (12) of [77], which is defined by neglecting the angular dependence.

The first factor is the maximum amplitude of the memory effect, while the second is an angular factor that takes into account the angle between the direction of the ejection velocity and the direction toward the observer. This angular factor is obtained in the case of an observer at infinity and in a reference system centered on the remnant.

From Eq. (3.29), an order-of-magnitude estimate for the peak memory effect yields [77]:

$$\Delta h_{\mathrm{dyn/wind}} = 3.8 \times 10^{-25} \left(\frac{\mathrm{M_{ej}}}{0.01 M_{\odot}}\right) \left(\frac{\mathrm{v_{ej}}}{0.2\ \mathrm{c}}\right)^{2} \left(\frac{\mathrm{r}}{100\ \mathrm{Mpc}}\right)^{-1}. \tag{3.30}$$

This value can be compared with the minimum and maximum values for dynamical and disk wind ejecta for the same distance of 100 Mpc. Based on the exponential model [100], the strain amplitude $\Delta h$ for the dynamical ejecta lies in the interval $[9.57 \times 10^{-28}, 1.53 \times 10^{-24}]$, while the disk wind ejecta lies in the interval $[9.57 \times 10^{-27}, 3.83 \times 10^{-25}]$. The values found are consistent with the order of magnitude mentioned above. Finally, the temporal and frequency behavior is also illustrated in Fig. 3.6 and Fig. 3.7 for the dynamical and wind ejecta, respectively.

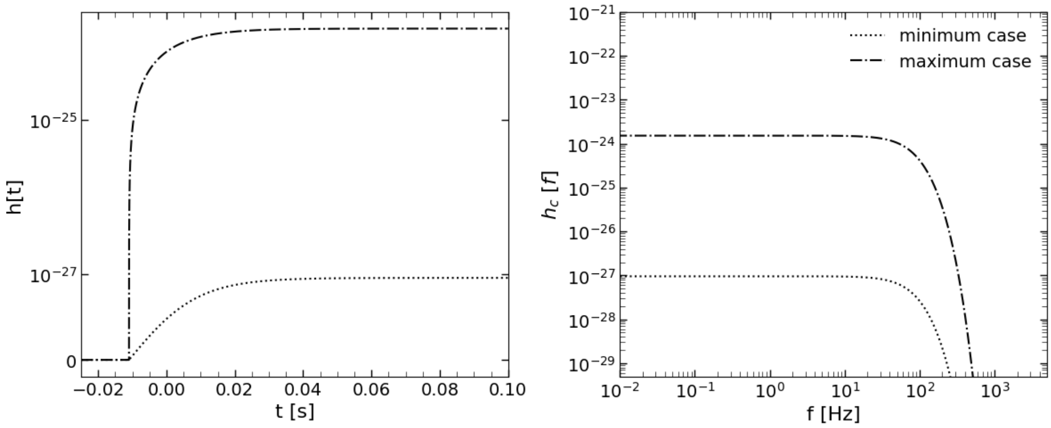


Figure 3.6: Temporal and frequency evolution of minimum and maximum values for dynamical ejecta. The exponential model is used for a distance of 100 Mpc and the parameters included in Table 3.1. The memory of the dynamical ejecta start to grow before the merger because matter is ejected due to tidal effects.

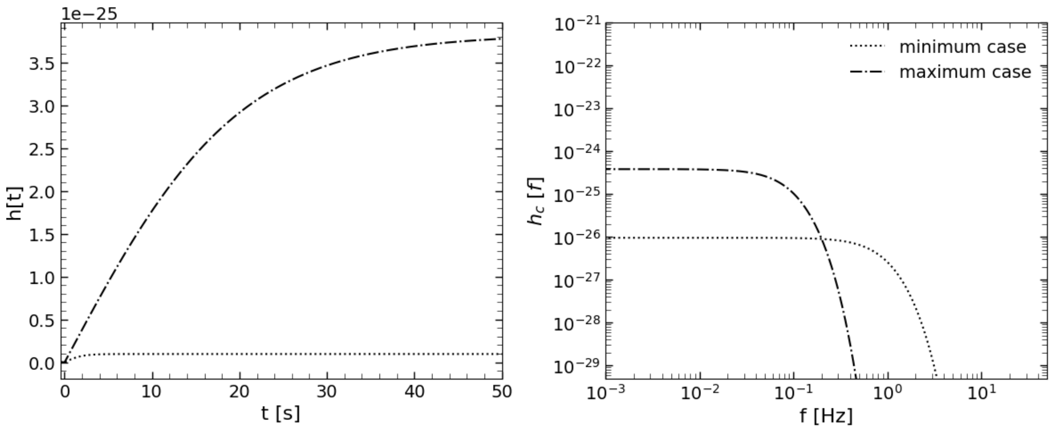


Figure 3.7: Temporal and frequency evolution of minimum and maximum values for disk wind ejecta. The exponential model is used for a distance of 100 Mpc and the parameters included in Table 3.1.

Lastly, Fig. 3.8 investigates the influence of the characteristic times, $\tau_{\rm dyn}$ and $\tau_{\rm wind}$, on the memory signal.

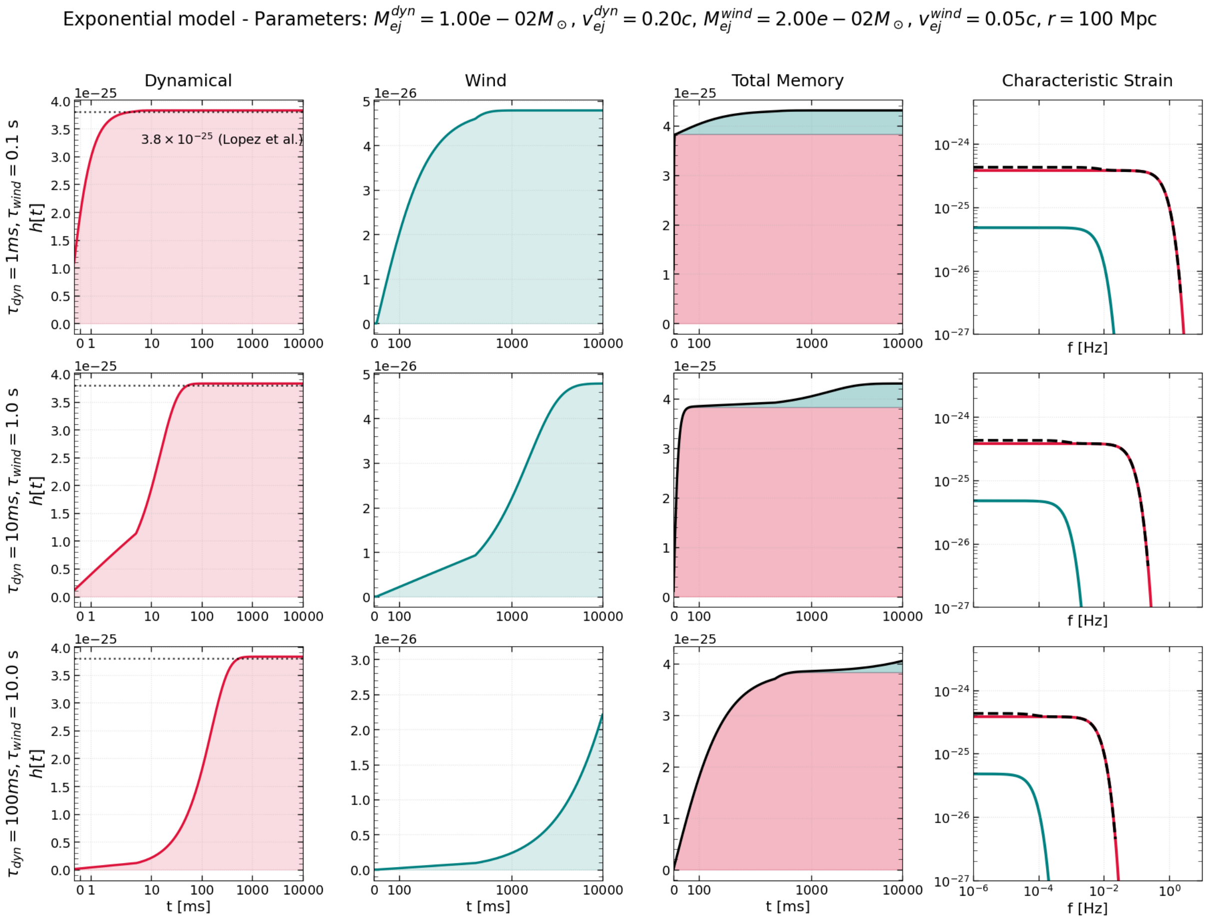


Figure 3.8: Evolution of the memory for the dynamical (red) and disk wind (blue) ejecta with parameters mentioned in the title and using the exponential model. Increasing the characteristic times $\tau_{\rm dyn}$ and $\tau_{\rm wind}$ (from top to bottom) delays the signal saturation, smooths the total memory curve and shifts the characteristic strain decay toward lower frequencies. The dotted line in the first column indicates the reference amplitude from [77] ($\Delta h_{\rm dyn} = 3.8 \times 10^{-25}$) for the dynamical ejecta. The dashed line in the last column is the summed characteristic strain of both ejecta.

The plots demonstrate that increasing the characteristic time shifts the point at which the saturation is reached to a later time. In the frequency domain, this evolution alters the characteristic strain $h_c(f)$, causing the signal to decay at lower frequencies as the rise time increases. The temporal and frequency content is also dominated by the dynamical ejecta, while the wind ejecta only provides a correction that is (at best) one order of magnitude lower.

Furthermore, a typical value from [77] is included as a reference to compare our results with the expected memory amplitude formed by the dynamical ejecta. Our calculated $h(t)$ reaches the same plateau as the reference. For the disk wind ejecta, the amplitude is lower due to the lower velocity ($v = 0.25c$). A generic distance of 100 Mpc has been used in Eq. (3.30), same as in the work of Lopez et al [77], in order to compare.

## 3.4 GRB memory

Due to their highly energetic and violent nature, GRBs are sources of GWs and should contain a memory effect [98]. In this section, we will first distinguish the memory effect caused by the prompt emission of the GRB and that caused by the afterglow and then proposed a joint model.

### 3.4.1 Prompt emission memory

GRBs typically launch multiple jets over the prompt burst duration due to internal variability in the central engine [14]. Each jet ejection corresponds to a discrete energy release episode, producing the observed variability in the prompt gamma-ray emission. The memory signal, arising from the sudden acceleration of these jets, therefore exhibits a multi-step structure due to the additive perturbations.

The multi-step structure is characterized by three timescales [14]: the individual jet rise time $\Delta T_{\rm rise}$ (set by jet acceleration), the inter-jet separation $\Delta T_{\rm sep} \sim 0.1$ s (reflecting central engine variability), and the total prompt duration of the GRB $\Delta T$ [14]. Since $\Delta T_{\rm rise} \ll \Delta T_{\rm sep} \ll \Delta T$, the waveform exhibits numerous steps, each corresponding to a single jet ejection event [14]. The final memory amplitude reflects the total ejected energy, reached after $\Delta T$, with characteristic frequency $f_\tau \sim 1/\Delta T$ [14].

To illustrate easily the broad picture, we analyze the contribution of a single *point-particle* (rather than an extended jet[4]) undergoing an instantaneous acceleration from 0 to $\beta$ and associated to the prompt duration and energy of the burst with amplitude $\Delta h_{\rm GRB}$ [14, 77, 98]. The change in the metric reads [14, 77, 98]:

$$\Delta h_{\rm GRB} = \frac{2E_j\beta^2}{r}\,\Theta(\theta), \tag{3.31}$$

where $E_j$ is the jet energy, $\beta = v/c \sim 1$ the jet velocity, $r$ the source distance, and $\theta$ the viewing angle from the jet axis. In this work, we set $E_j = E_{\rm GRB,\ iso}$, the isotropic equivalent energy of the prompt energy, defined as the energy that would be emitted if the radiation was distributed uniformly over the full sphere. We acknowledge that this model is further simplified, it neglects the acceleration time[5] and reduces the jet to a point. Since the jet is in reality collimated within a half-opening angle $\theta_j$, the latter assumption overestimates the true jet energy by a factor $1/(1-\cos\theta_j)$, and therefore yields an upper bound on $\Delta h_{\rm GRB}$.

An order-of-magnitude estimate for the change in amplitude with an isotropic equivalent energy of $E_{\rm GRB,\ iso} = 10^{52}$ erg gives:

$$\Delta h_{\rm GRB} = 5.35\times 10^{-24}\left(\frac{E_{\rm GRB,\ iso}}{10^{52}\ {\rm erg}}\right)\left(\frac{r}{100\ {\rm Mpc}}\right)^{-1}. \tag{3.32}$$

Since $\Delta h \propto E_{\rm GRB,\ iso}$, the prompt energy directly controls the signal amplitude and so its detectability.

[4] A more realistic description of the geometry of the GRB jet is provided in the appendix A.5.

[5] Estimates give a acceleration done on a timescale of 0.1 ms [77], but in this model we assume that the rise time is dictated by the prompt duration and this dynamic is therefore neglected.

### 3.4.2 Afterglow memory

Following the prompt emission, the decelerating jet interacts with the circumburst medium, producing the GRB afterglow through synchrotron radiation of shock-accelerated electrons. By analogy with the GRB case, this energy release also gives rise to a memory effect, whose amplitude scales with the energy dissipated during the afterglow phase. This energy is commonly characterized by its isotropic equivalent, $E_{\text{aft, iso}}$ and for the case of long GRBs, an order of magnitude of the energy of the afterglow is $E_{\text{aft}} \sim 10^{51}$ erg [69]. Analogous to Eq. (3.31), the afterglow memory amplitude can be estimated as:

$$\Delta h_{\text{aft}} = \frac{2\,E_{\text{aft}}\,\beta^2}{r}\;\Theta(\theta). \tag{3.33}$$

As the formula is similar to that of the GRB, the memory amplitude follows the same trend.

In addition to the forward-shock emission from the fireball model, a distinct mechanism modify the afterglow emission. The central engine can inject some of its energy into the blast wave and thus alter the afterglow light curve by producing a bump[6]. The formula we could use to compute the memory effect produced by the energy injection of the jet to the afterglow is given by [101]:

$$\Delta h_{\text{aft, inj}} = \frac{P_{\text{in}}\,T_{\text{end}}\,\beta^2}{r}\;\Theta(\theta)\;(1-\cos(\theta_j)), \tag{3.34}$$

where $P_{\text{in}}$ is the power injected into the circumburst medium by the central engine, $T_{\text{end}}$ is the duration of the injection mechanism as seen by an on-axis observer, $\theta$ the viewing angle, and $\theta_j$ the jet half-opening angle [98]. The extra term $(1-\cos(\theta_j)$ accounts for the geometry of the jet, with a larger amplitude for more opened GRB jet. An estimate of the memory signal amplitude for GRB injecting energy during a period $T_{\text{end}}$ is:

$$\Delta h_{\text{aft, inj}} = 5\times 10^{-26}\left(\frac{\mathrm{P_{in}}}{10^{50}\ \mathrm{erg\ s^{-1}}}\right)\left(\frac{\mathrm{T_{end}}}{200\ \mathrm{s}}\right)\left(\frac{\mathrm{r}}{100\ \mathrm{Mpc}}\right)^{-1}. \tag{3.35}$$

However, both the amplitude and temporal evolution of $P_{\text{in}}$ are poorly constrained, and the underlying physical mechanism remains actively debated. We therefore introduce this formula solely for completeness and neglect the energy injection contribution in the chapter about detectability.

### 3.4.3 Global picture of GRB memory

Since a GRB is a two-phase event: the prompt emission and the afterglow, it is convenient to define a slightly modified version of $h(t)$. The model must include a first part relating to the prompt emission and another part for the afterglow. For the prompt GRB emission, its duration, given by the $T_{90}$ statistic, is used as the characteristic rise time for the prompt emission and so its memory effect. For the afterglow, two characteristic timescales are used to express the onset and end of the phase: the deceleration time $t_{\text{dec}}$ and the jet break time $t_{\text{break}}$.

[6] A more detailed description was provided in the introduction . We refer the interested reader to the relevant references.

The deceleration time marks the moment at which the relativistic ejecta have swept enough of the surrounding ISM to begin decelerating. It is given by [102]:

$$t_{\rm dec} = (1+z)\,\left(\frac{3\,E_{\rm aft,\ iso}}{32\pi\,n\,m_p\,c^5\,\Gamma_0^8}\right)^{1/3}, \tag{3.36}$$

where $E_{\rm aft,\ iso}$ is the isotropic energy of the afterglow, $n$ the ISM number density, $m_p$ the mass of the proton, $\Gamma_0$ the initial Lorentz factor at the moment the jet is launched, and $z$ the redshift of the source. For typical GRB parameters, $t_{\rm dec}$ is of the order of 100 s. It is worth noting that $t_{\rm dec}$ can be shorter than $T_{90}$, particularly for long GRBs, meaning the afterglow shock can begin while the prompt emission is still ongoing.

In the early afterglow phase, when $\Gamma \sim 100$ to 1000, the observer only sees the relativistic beaming cone of angular size $1/\Gamma \ll \theta_j$, making the emission appear isotropic regardless of the jet geometry. As the blast wave propagates through the ISM, it sweeps increasing amounts of material, causing the Lorentz factor $\Gamma$ to decrease over time. When $\Gamma$ drops sufficiently, the assumption of a highly relativistic outflow is no longer valid, and the relativistic beaming effect weakens accordingly. As $\Gamma$ decreases and approaches $\theta_j^{-1}$, the beaming cone widens until the observer starts to see the edge of the jet and causes the flow to decrease sharply. This transition defines the jet break time $t_{\rm jet}$, the moment when the finite opening angle of the jet becomes observable when $\Gamma \sim \theta_j^{-1}$. The afterglow light curve transition from a shallower power-law decay (with a spectral index $\sim 1$) to a steeper power-law (with a new spectral index $\sim 2$) [103]. The break in the light curve seems to appear between 0.1-10 days after the detection of the GRB [104]. In a constant-density medium, the break time $t_{\rm break}$ reads [105]:

$$t_{\rm break} = 6.2\ (1+z)\left(\frac{\theta_j}{0.1\ \rm rad}\right)^{8/3}\left(\frac{E_{\rm aft,\ iso}}{10^{52}\,\rm erg}\right)^{1/3}\left(\frac{n}{0.1\,\rm cm^{-3}}\right)^{-1/3}\ \rm hr, \tag{3.37}$$

where $\theta_j$ is the half-opening angle of the jet and $n$ the ISM number density.

This makes $t_{\rm break}$ an appropriate endpoint for the afterglow memory rise, as it marks the onset of the stepper decay phase. Based on the definition above, the jet break is a wavelength-independent feature, this is another reason why we prefer to use this quantity rather than the total duration of the afterglow, which depends on the wavelength. Note that this time is shorter than the actual duration of the afterglow. However, for the purposes of computing the memory, we assume that the less isotropic emission produced after this time is negligible, and therefore the memory after the break time is likewise negligible.

The total memory signal $h(t)$ is built as the sum of two components, each rising linearly over its own characteristic timescale. The GRB component rises over $T_{90}$, while the afterglow component begins at $t_{\rm dec}$ and saturates at $t_{\rm break}$:

$$\Delta h_{\rm GRB}(t) = \begin{cases} 0 & t < 0 \\ \Delta h_{\rm GRB}\left(\dfrac{t}{T_{90}}\right) & 0 \leqslant t < T_{90} \\ \Delta h_{\rm GRB} & t \geqslant T_{90} \end{cases} \tag{3.38}$$

$$\Delta h_{\rm aft}(t) = \begin{cases} 0 & t < t_{\rm dec} \\ \Delta h_{\rm aft}\left(\dfrac{t - t_{\rm dec}}{t_{\rm break} - t_{\rm dec}}\right) & t_{\rm dec} \leqslant t < t_{\rm break} \\ \Delta h_{\rm aft} & t \geqslant t_{\rm break} \end{cases}$$

Thus, the total memory reads $h(t) = \Delta h_{\mathrm{GRB}}(t) + \Delta h_{\mathrm{aft}}(t)$.

The FT of each component can be computed analytically following the approach of [98], adapted here to the timescales $T_{90}$ and $t_{\mathrm{jet}} - t_{\mathrm{dec}}$. The power spectrum of each component reads:

$$|\tilde{h}_{\mathrm{GRB}}(f)|^2 = 4\, a_{\mathrm{GRB}}^2 \sin^4(\pi f T_{90})\,, \tag{3.39}$$

$$|\tilde{h}_{\mathrm{aft}}(f)|^2 = 4\, a_{\mathrm{aft}}^2 \sin^4(\pi f (t_{\mathrm{break}} - t_{\mathrm{dec}}))\,, \tag{3.40}$$

with $a_{\mathrm{GRB}} = \Delta h_{\mathrm{GRB}}/(4\pi^2 f^2 T_{90})$ and $a_{\mathrm{aft}} = \Delta h_{\mathrm{aft}}/(4\pi^2 f^2 (t_{\mathrm{break}} - t_{\mathrm{dec}}))$. The total amplitude then takes the form:

$$|\tilde{h}(f)|^2 = |\tilde{h}_{\mathrm{GRB}}(f)|^2 + |\tilde{h}_{\mathrm{aft}}(f)|^2. \tag{3.41}$$

The characteristic timescales $T_{90}$ and $(t_{\mathrm{break}} - t_{\mathrm{dec}})$ directly set the break frequencies in the spectrum, as each linear rise produces an $f^{-1}$ decay above the corresponding inverse timescale. Longer timescales shift the spectral break toward lower frequencies, causing the $f^{-1}$ decay to begin earlier, as illustrated in Fig. 3.9. As for the previous cases, the effect of increasing the amplitude of the memory is to raise the frequency content and the increase of the rising phase shift the distribution to the left.

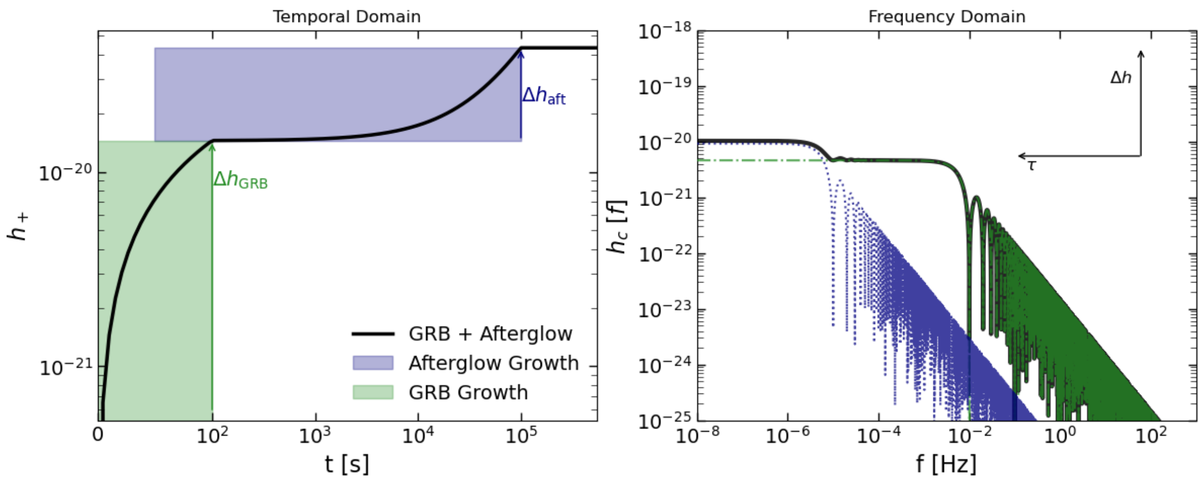


Figure 3.9: Memory signal for the prompt-afterglow model with $T_{90} = 100$ s, $t_{\mathrm{dec}} = 50$ s and $t_{\mathrm{jet}} = 10^5$ s, for $E_{\mathrm{GRB,\ iso}} = 5 \times 10^{53}$ erg and $E_{\mathrm{aft,\ iso}} = 10^{54}$ erg at 1 Mpc. The prompt and afterglow components are shown in green (dotted) and blue, respectively. The arrows in the top right corner represent the effect of increasing the amplitude $\Delta h$ or the rise time $\tau$ in the frequency domain.

## 3.5 Kilonova memory

### 3.5.1 Derivation of the photonic linear memory

The kilonova generates anisotropic EM radiation over timescales of 1 to 10 days post-merger. This asymmetric photon emission produces a net momentum flux that induces a linear memory effect, due to the anisotropic expulsion of massless particles. To determine the kilonova memory, we adapt the formula provided in [99] in the context of neutrino memory. Neutrinos also constitute a source of linear memory, but since no neutrinos were detected for the GW170817 event, we neglect their impact. Recent simulations [106] taking neutrinos into account have been performed and estimate their impact to be negligible at the time of the merger, introducing only a small correction starting around 25 ms after the merger (see Fig.3 of [106]).

The photon's contribution can be derived by adapting Eq. (1.62). Each photon labeled $A$ with energy $E_A$ emitted in direction $\mathbf{n}_A$ carries momentum $E_A/c$, making an angle $\theta_A$ between the velocity vector and $\mathbf{n}_A$, and contributes to the memory signal. To determine the formula from the kilonova emission, we start from the linear memory formula expressed as:

$$\Delta h_{ij}^{\mathrm{TT}} = \frac{4}{r}\Delta\left[\sum_{A=1}^{N}\frac{M_A}{\sqrt{1-v_A^2}}\left(\frac{v_A^i v_A^j}{1-v_A\cos(\theta_A)}\right)\right]^{\mathrm{TT}}. \tag{3.42}$$

In the case of a photon flux, we replace the relativistic energy and the velocity by:

$$\frac{M_A}{\sqrt{1-v_A^2}} \rightarrow E_A, \tag{3.43}$$

$$v_A^k \rightarrow cn_A^k = n_A^k, \tag{3.44}$$

where we set $c = 1$ in the natural system units. Moreover, if we assume a continuous emission of photons over a solid angle $\Omega$, the expression of the energy distribution takes the form:

$$\sum_{A=1}^{N} E_A \rightarrow \int_{4\pi}\frac{dE}{d\Omega}d\Omega. \tag{3.45}$$

Under these adaptations, the instantaneous linear memory effect produced by a flux of photons over a solid angle is as follows:

$$\Delta h_{ij}^{\mathrm{TT}} = \frac{4}{r}\int_{4\pi}\frac{dE}{d\Omega}\left[\frac{n^i n^j}{1-\cos(\theta)}\right]^{\mathrm{TT}} d\Omega. \tag{3.46}$$

Since the memory effect is hereditary, temporal dependence is obtained by integrating from early times up to the retarded time $t_r = t - r/c$, thus

$$\Delta h_{ij}^{\mathrm{TT}}(t) = \frac{4}{r}\int_{-\infty}^{t_r} dt' \int_{4\pi}\frac{dE(\Omega,t')}{dt'd\Omega}\left[\frac{n^i n^j}{1-\cos(\theta)}\right]^{\mathrm{TT}} d\Omega. \tag{3.47}$$

If we define the luminosity produced by the emitted particles as $dL = dE/dt'$, the result is reduced to a similar formula given in [99]:

$$\Delta h_{ij}^{\mathrm{TT}}(t) = \frac{4}{r}\int_{-\infty}^{t_r} dt' \int_{4\pi}\frac{dL(\Omega,t')}{d\Omega}\left[\frac{n^i n^j}{1-\cos(\theta)}\right]^{\mathrm{TT}} d\Omega. \tag{3.48}$$

In particular, the plus polarization is denoted as $h_{xx}^{TT} = h_{+}^{TT}$.

The main result of this rewriting of linear memory is that the energy of each particle has been replaced by the temporally integrated photonic luminosity. Thus, the variable of interest for calculating the memory effect becomes the luminosity of the kilonova. Finally, we can provide an order of magnitude associated with this memory if we consider an emission that occurs on a daily timescale with a brightness of around $10^{45}$ erg/s:

$$\Delta h_{\mathrm{kilonova}} = 9.25\times 10^{-25}\left(\frac{\mathrm{L}}{10^{45}\ \mathrm{erg/s}}\right)\left(\frac{\mathrm{t}}{1\ \mathrm{day}}\right)\left(\frac{\mathrm{r}}{100\ \mathrm{Mpc}}\right)^{-1} \tag{3.49}$$

It is noteworthy to mention that the estimated amplitude is close to that for dynamical ejecta and wind. This reinforces the importance of not neglecting the impact of kilonova-induced memory compared to other ejecta.

### 3.5.2 Results from a kilonova simulation

In the following section, we will determine the linear memory effect produced by a kilonova, thanks to a numerical simulation. The 3D simulation was generated based on the radiative transfer solution for a kilonova with parameters similar to those of AT2017gfo, using the `POSSIS` model [107]. In this model, the ejecta producing the kilonova emission is divided into a dynamical component and a disk-wind component. The dynamical ejecta is further split into two distinct regions with velocities ranging from $v_{\rm min}^{\rm dyn} = 0.08c$ to $v_{\rm max}^{\rm dyn} = 0.3c$: a lanthanide-free polar component, and a lanthanide-rich tidal (equatorial) component [108]. The disk-wind ejecta is modeled as a spherical outflow released by the accretion disk and the post-merger remnant [47], characterized by slower velocities ranging from $v_{\rm min}^{\rm wind} = 0.025c$ to $v_{\rm max}^{\rm wind} = 0.08c$ [108].

Based on this physical framework, the simulation outputs the energy and frequency of each pixel forming the kilonova. The time array covers a span starting 0.08 days after the merger and ending 9.8 days later, and is uniformly sampled at a frequency of $9.89 \times 10^{-4}$ Hz.

#### Energy evolution

The simulation reveals three distinct evolutionary phases in the energy emission. During the first instants, emission is intense ($\sim 10^{46}$ erg s$^{-1}$) and strongly polar-concentrated. The intermediate phase exhibits a more isotropic angular distribution with reduced luminosity ($\sim 10^{44}$ erg s$^{-1}$). At late times ($t \gtrsim 5$ days), emission shows comparable contributions from both polar and equatorial regions. This temporal evolution is depicted in Fig. 3.10. Notably, the integrated emission exhibits hemispheric asymmetry: the southern hemisphere radiates approximately 19% more energy than the northern hemisphere. This global anisotropy ensures a non-vanishing total linear memory contribution.

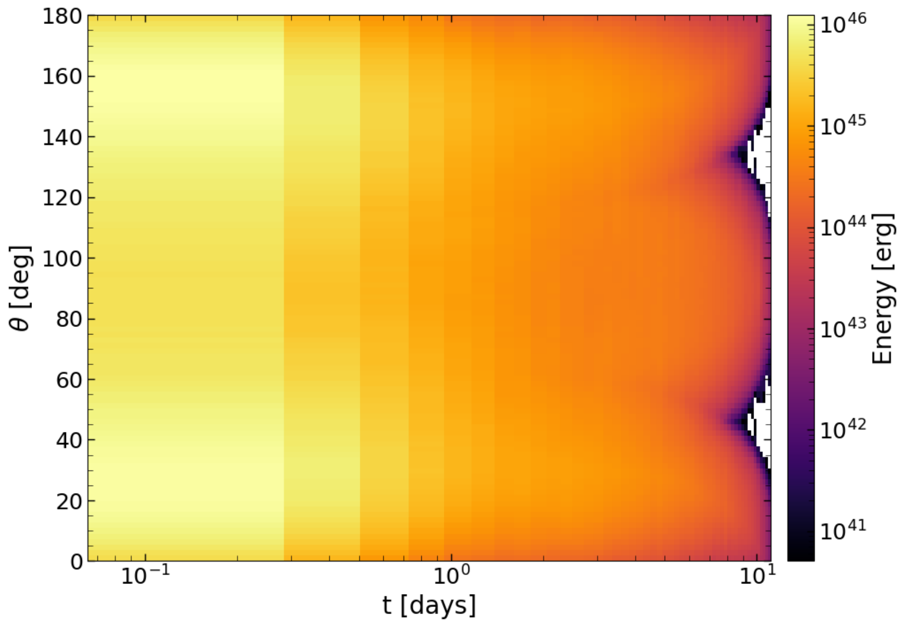


Figure 3.10: Energy distribution as a function of time and viewing angle, using 100 angular bins, 50 temporal bins, and integrated into a cone opening angle 0.5 radians around the polar angle $\theta$.

In addition, the energy spectrum also evolves over time in a similar manner to energy.

We also note that the emission transitions from short wavelengths ($\sim 500$ nm) to longer wavelengths ($\sim 1500$ nm). This is in fact the transition from a blue kilonova to a red kilonova as observed in Fig. 3.11.

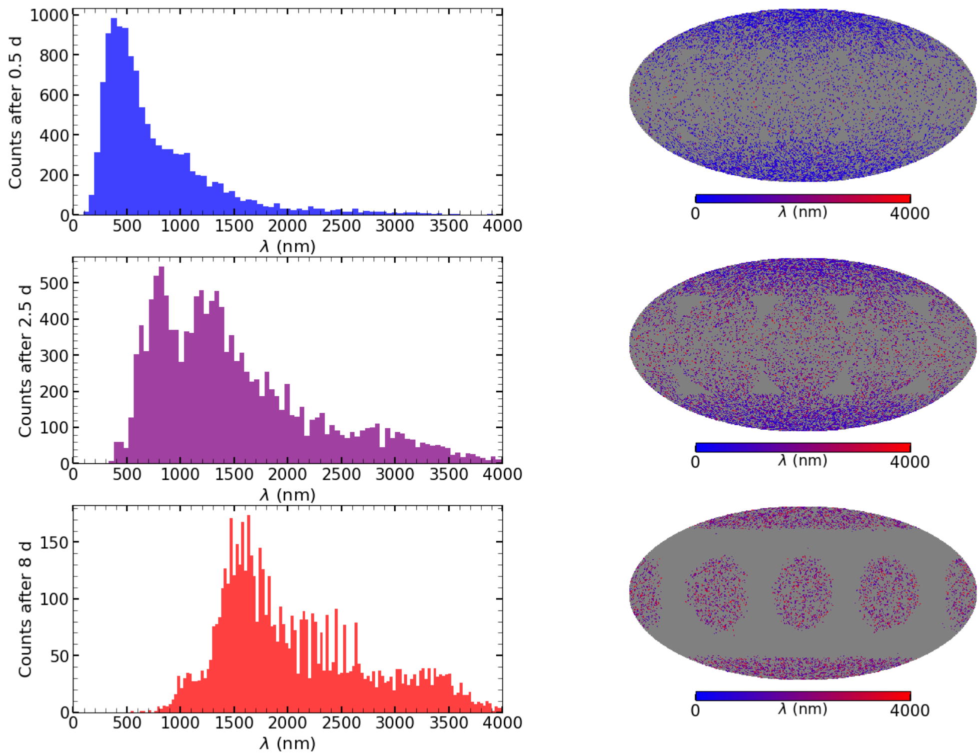


Figure 3.11: *Left:* Emission spectrum different times (day(s) after the merger). The emission transitions from blue (early, high-energy) to red (late, lower-energy). *Right:* Healpy maps of the energy distribution at selected times, illustrating the shift in dominant emission regions and corresponding changes in wavelength, from shorter (blue) to longer (red), as the simulation evolves. The angular distribution first broadens and then becomes more peaked at late times, similarly to Fig. 3.10.

Based on these initial observations, we can already indicate that the memory will evolve over a timescale of up to approximately 10 days, given the evolution of energy. This is already a major difference compared to the characteristic timescales of the previously discussed ejecta components.

### Time domain

After implementing the formula Eq. (3.48), we have obtained results that make it possible to discuss the variation in the memory resulting from the simulated kilonova as a function of time and the viewing angle $\theta$.

Numerically, the accumulated memory is obtained by summing the contributions of each pixel at every time step until the end of the simulation. Each pixel contributes according to two factors: its brightness and an angular factor relative to the observer. More energetic pixels contribute more strongly, directly scaling the memory amplitude. The kilonova's energy distribution and geometry are thus imprinted in this contribution. Meanwhile, the geometric dependence relative to the observer's line of sight is explicitly captured by the following angular factor:

$$\left[\frac{n^i n^j}{1-\cos(\theta)}\right]^{\mathrm{TT}}, \tag{3.50}$$

from Eq. (3.48).

To compute this term, we did not use the simplified Eq. (3.28) because there is a priori no symmetry associated with this emission. However, in order to simplify our discussion, we will consider a coordinate system where the observer lies at an azimuthal angle $\phi = 0$. In this configuration, the polarization $\times$ vanishes, and only $h_+$ is evaluated[7]. To determine this polarization, the TT projector Eq. (1.36) is first calculated, and the argument was projected to obtain an estimate of the angular factor for each pixel. Then, to isolate the remaining non-zero degree of freedom, we construct an orthonormal basis in the plane transverse to the line of sight, onto which we project the TT element. Let $\mathbf{z} = (0, 0, 1)$ be the unit vector pointing along the positive z-axis of a Cartesian reference coordinate system centered on the remnant. If $\mathbf{n}$ denotes the unit vector pointing from the source to the observer, we set $\mathbf{e}_1 = \mathbf{n} \times \mathbf{z}$. By construction, this vector $\mathbf{e}_1$ is orthogonal to $\mathbf{n}$. To complete the basis, we set $\mathbf{e}_2 = \mathbf{n} \times \mathbf{e}_1$. By construction, $\mathbf{e}_2$ is orthogonal to $\mathbf{n}$ and to $\mathbf{e}_1$, and forms with $\mathbf{e}_1$ an orthonormal basis in the transverse plane. We extract the polarizations by projecting the $h^{\mathrm{TT}}$ on the basis described in Eq. (1.44) and we obtain:

$$h_+ = e_1^i e_1^j h_{ij}^{\mathrm{TT}}\ , \quad h_\times = e_1^i e_2^j h_{ij}^{\mathrm{TT}} = 0 \ \text{ if } \phi = 0. \tag{3.51}$$

A Mollweide projection showing the brightness per pixel and the angular factor (+ component) for an angle $\theta = 32^\circ$ is shown in Fig. 3.12. It is clear that the polar regions have the highest brightness per pixel, and it is therefore these regions that will have the largest effect on the memory's amplitude. In the right-hand plot illustrating the angular factor pattern for + polarization, we observe that it has both positive and negative regions. This is because we are considering only the + polarization, which can cause the test masses to move closer together (negative value) or farther apart (positive value). Note that there are as many positive pixels as negative ones, regardless of the angle.

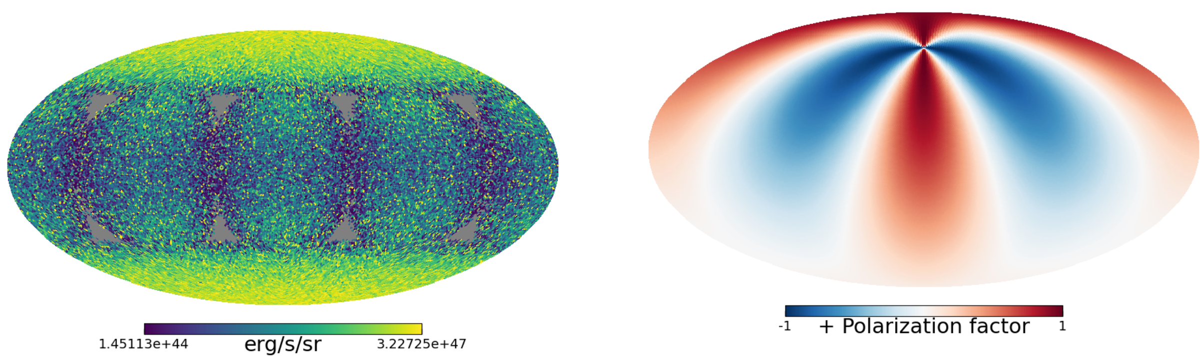


Figure 3.12: Comparison of luminosity (*left*) and angular factor (*right*) maps. The grey patches in the luminosity map are data points with no value from the simulation.

Based on the definition of the kilonova memory, the resulting signal can be factored into the product of these two maps: one representing the intrinsic memory amplitude and the other representing the geometric angular factor. This means that if the kilonova's

[7] As $h_+ \propto \cos(2\phi)$ and $h_\times \propto \sin 2\phi$. Similarly, this angular dependence is also found in Eq. (3.22).

emission is isotropic, then the positive and negative pixels cancel each other out one by one, and the resulting memory is zero. Therefore an anisotropic emission is the only way to produce a non-zero linear memory effect.

For an observer angle at $\theta = 32°$, consistent with the value deduced for GW170817 [49], Fig. 3.13 shows the accumulated kilonova memory signal in that direction, reaching a final value of $1.6 \times 10^{-25}$. A pixel-by-pixel map of these contributions at the final step is provided in Fig. 3.14. The kilonova memory differs notably from the phenomenological step-function models discussed previously. Rather than being characterized by a single rise timescale, the memory evolution directly mimics the luminosity, and hence the energy of the kilonova over time. Moreover, the timescale up to which the memory saturates is much longer than in the preceding cases. We can already infer that the characteristic strain will take on high values at frequencies lower than those mentioned in the other cases. One can also note that the signal does not exhibit a clear final plateau, even though it appears to saturate at the end of the simulation. This is because the simulation provides information on the emitted energy only over a period of approximately 10 days. The trend of the kilonova emission at longer times would be a decrease in brightness (as the ejecta cool down), which results in a slight rise followed by a late plateau as the transient event ends. Since we only have the simulation available, we assume that the late-time emission is negligible.

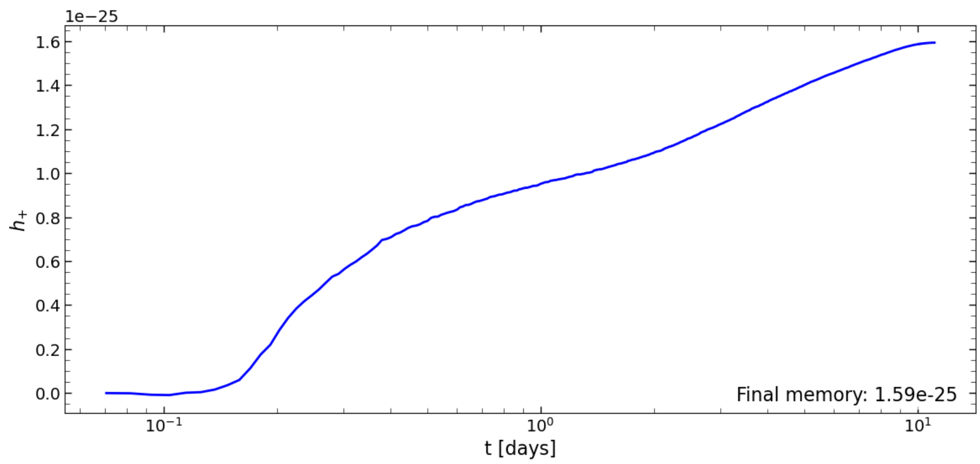


Figure 3.13: Time-domain evolution of the kilonova memory ($h_+$) for an observer at 40 Mpc at an angle $\theta = 32°$ away of the North Pole and $\phi = 0$.

### Frequency domain

By applying padding (2.2) and tapering (2.3) methods, the time series has been converted to the frequency domain using FFT method. FTs for different angles are displayed in Fig. 3.15 while the characteristic strain is shown in Fig. 3.16. The case where the observation angle is that of GW170817 is marked in green.

Both hemispheres share several common features. First, since the simulation's sampling frequency is $\sim 10^{-3}$ Hz, Nyquist's theorem limits the maximum achievable frequency to $0.5 \times 10^{-3}$ Hz. One straightforward way to increase the limit is to interpolate additional data points, thereby increasing the effective sampling frequency. However, this comes at the cost of more computational demand. Separately, since the memory is known to decay as $f^{-1}$ at low frequencies, the signal can also be extrapolated following this trend, which

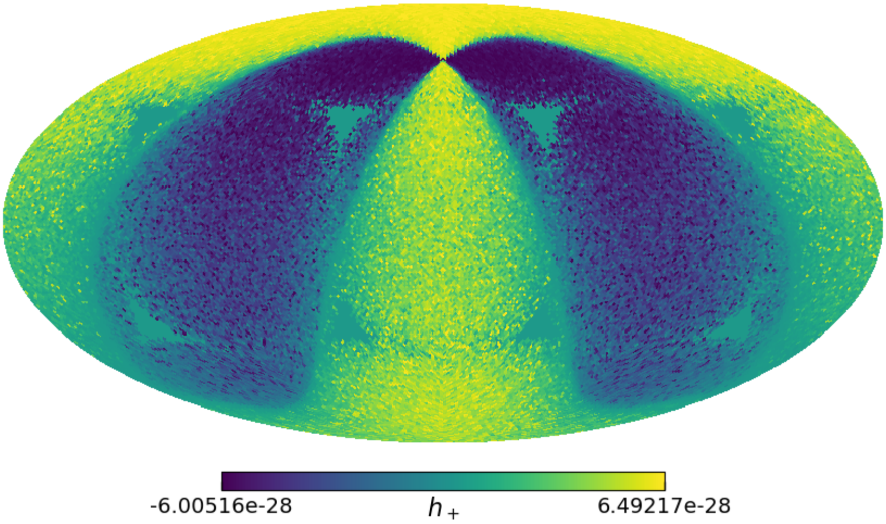


Figure 3.14: Memory map snapshot at the end of the simulation ($8.54 \times 10^5$ s or 9.89 days) for an observer at an angle $\theta = 32^\circ$ away of the North Pole and $\phi = 0$. The eight cyan triangular regions symmetric about the equator are zero because the simulation contains no data at these points.

serves as an upper bound given that the signal falls off more steeply at higher frequencies. Going forward, both methods will be used in combination in the detectability analysis.

The second common feature is the angular dependence. At low frequencies, the spectral amplitude is smallest at the poles and grows toward the equator. This can be understood by revisiting the two key contributions to the kilonova's memory: the luminosity distribution, which is concentrated at the poles, and the angular factor, which tends to suppress the transverse component. At the poles, the angular factor of the + strain suppresses the transverse emission most strongly precisely where the luminosity is the highest, leading to a weakened memory for a polar observer. For an equatorial observer, the suppression instead acts primarily on the equatorial plane, where the luminosity is low, leaving the bright polar emission largely unattenuated and thus producing a stronger net memory[8]. The pronounced variability of the FFT near the poles is also attributable to the angular factor. At these viewing angles, the memory depends sensitively on the angular pattern of the + polarization, with some sky pixels contributing positively and others negatively, leading to a nearly zero memory that can vary sharply. This results in fluctuations at low frequencies. Finally, the convergence of the spectral content across all angles in the zoomed-in region of both figures reflects the attenuation introduced by the windowing function.

Looking solely at the FFT evolution, the low-frequency behavior scaling as $f^{-1}$ is reassuring, as it is consistent with other known memory effects. Likewise, the constant evolution of the characteristic strain is equally reassuring. For viewing angles far from the poles, the values of $h_c$ saturates at best at $10^{-25}$. At first glance, this may appear encouraging, as the other linear memory effects exhibit the same order of magnitude under similar configurations. However, the frequency evolution of the kilonova memory occurs at much lower frequencies, where it correspondingly decreases. Consequently, we expect the kilonova memory to be weaker at the optimal frequencies of next-generation detectors.

[8] An illustration of the angular factor projected on the + basis is displayed in A.6 for different viewing angles.

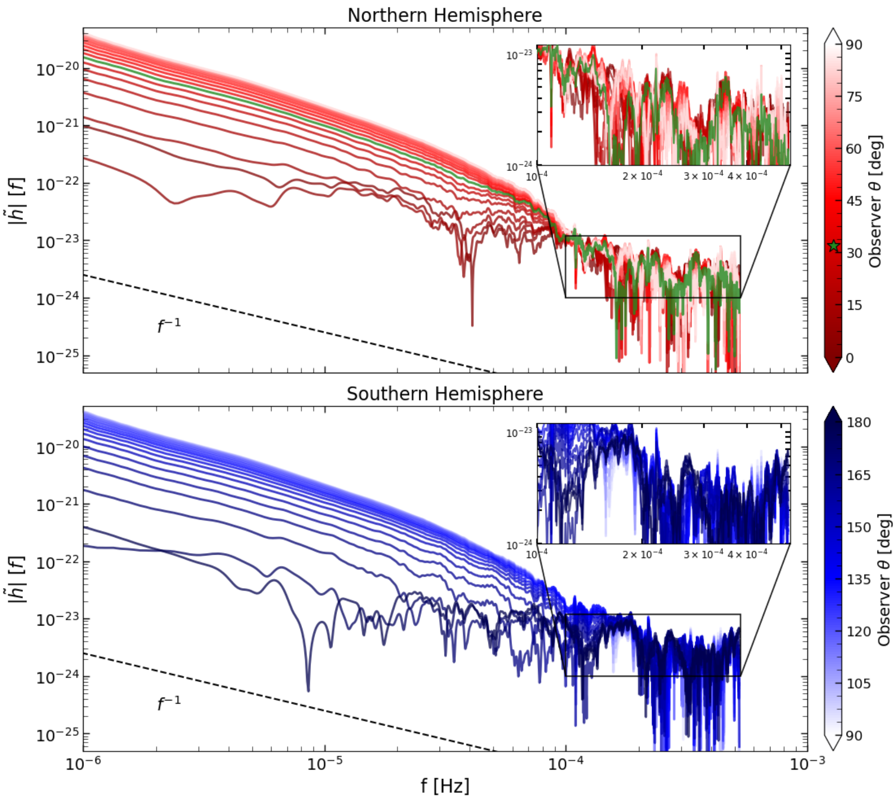


Figure 3.15: FFT of the kilonova memory for a range of observer angle from Northern to Southern hemispheres with $\phi = 0$. The case of GW170817 detection at $\theta = 32^\circ$ is highlighted in green. The signal was first processed using padding of length $r = 10$ and a Tukey window with $\alpha = 0.4$.

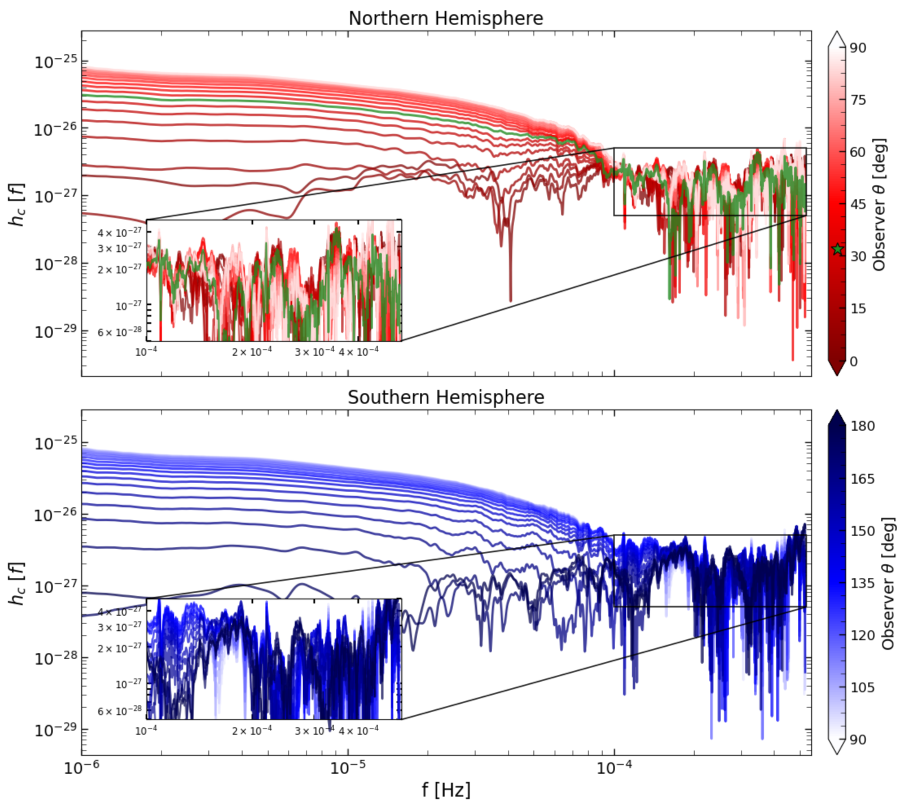


Figure 3.16: Characteristic strain $h_c$ of the kilonova memory computed from Fig. 3.15.

Chapter 4

# Detectability with ET and LISA

After having introduced models of nonlinear and linear memory effects, this chapter focuses on the application of such models to the detectability of memory. First, we will examine the ejecta from GW170817. In this framework, all the memory effect presented in the thesis will be computed in order to infer the SNR at ET. In addition, particular attention will be devoted to GRBs and their afterglows. For certain configurations, it is possible that LISA could detect the memory of these phenomena.

## 4.1 GW170817 framework

The ideal context for studying various memory effects and their additive contribution is, of course, GW170817. We model the linear memory based on phenomenological models for the dynamical, wind, GRB, and afterglow ejecta, employing the values listed in Table 4.1.

The linear memory of the dynamical ejecta and the disk wind is assumed to depend on an angular factor $\Theta(\theta)$, yet in this section we consider that the entire emission is made at the angle $\theta$. In a more realistic framework, the phenomenological model should take into account the density and velocity distribution of each ejecta. Estimates of these distributions exist [52], but they only indicate the trends in the evolution. We would then need to assume a total mass and a dynamic time, which, for a first approximation, is too arbitrary. We therefore restrict ourselves to ejecta where the angular factor is neglected. This implies that we are overestimating the memory of the dynamical and the wind ejecta.

The nonlinear memory effect was generated using `GWMemory` with all modes of the NRSur7dq2 approximant. The signal was padded with $r = 50000$ and a Tukey window ($\alpha = 0.4$) was applied. For the kilonova simulation, the signal was padded to ten times its original length and tapered using a Tukey window ($\alpha = 0.4$). Since we are interested in a frequency range of 100 Hz for ET, further padding is unnecessary. We have extrapolated the signal to a trend of $f^{-1}$ at high frequencies. As mentioned in the previous chapter, applying this method amounts to placing an upper limit on the signal. This extrapolation is reflected as a constant straight line when computing the characteristic strain. Each component of the memory effect for a GW170817-like event is displayed in Fig. 4.1.

Table 4.1: Parameters of the GW170817 event used for memory computation

| Component | Parameter name | Symbol | Value |
|---|---|---|---|
| Binary system | Primary mass | $m_1$ | $1.46\,M_\odot$ |
| | Secondary mass | $m_2$ | $1.27\,M_\odot$ |
| | Mass ratio | $q$ | 1.185 |
| | Total mass | $M$ | $2.73\,M_\odot$ |
| | Distance | $d$ | 40 Mpc |
| | Inclination | $\theta_{\rm ej}$ | 32° |
| | Azimuthal angle | $\phi_{\rm ej}$ | 0.0° |
| Dynamical ejecta | Ejecta mass | $M_{\rm ej,dyn}$ | $0.005\,M_\odot$ |
| | Ejecta velocity | $v_{\rm ej,dyn}$ | $0.25\,c$ |
| | Characteristic timescale | $\tau_{\rm dyn}$ | $10^{-3}$ s |
| | Start time | $t_{\rm start,dyn}$ | $-10^{-3}$ s |
| Wind ejecta | Ejecta mass | $M_{\rm ej,wind}$ | $0.01\,M_\odot$ |
| | Ejecta velocity | $v_{\rm ej,wind}$ | $0.05\,c$ |
| | Characteristic timescale | $\tau_{\rm wind}$ | 10.0 s |
| | Start time | $t_{\rm start,wind}$ | 0.01 s |
| Prompt GRB | Isotropic energy | $E_{\rm GRB}$ | $3 \times 10^{46}$ erg |
| | Prompt duration | $T_{90}$ | 2.0 s |
| Afterglow | Isotropic energy | $E_{\rm aft}$ | $10^{52.2}$ erg |
| | Deceleration time | $t_{\rm dec}$ | 50 s |
| | Break time | $t_{\rm break}$ | 1 day |

### 4.1.1 Detectability with ET

The SNR has been computed using Eq. 2.11 with configuration ET-D[1]. Using the exponential models for the dynamical and the wind ejecta, an SNR of 12.59 was found by restricting the analysis to frequencies between 1 Hz and $10^4$ Hz, where the sensitivity curve of ET is defined. Fig. 4.2 shows the contribution of each memory effect, which can be ranked in two groups according to their significance. Among the dominant contributors, the nonlinear memory leads, as expected, followed by the dynamical ejecta. The dynamical ejecta memory owes its significance to two factors: it scales with the square of the ejection velocity and a privileged angular dependence that comes from the geometric approximations used to derive the memory amplitude. The remaining contributions (wind, GRB and kilonova) form a second group of negligible terms. Their weakness stems from a low wind velocity and a decay starting around $10^{-1}$ Hz, a weak prompt emission energy and a rapid decay of the afterglow. All of which render their SNR subdominant in ET.

[1]The 'D' refers to the naming convention of the triangular configuration of ET. Alternative configurations such as ET-B or ET-C which did not feature the triangular form, are still considered as final configuration of the project.

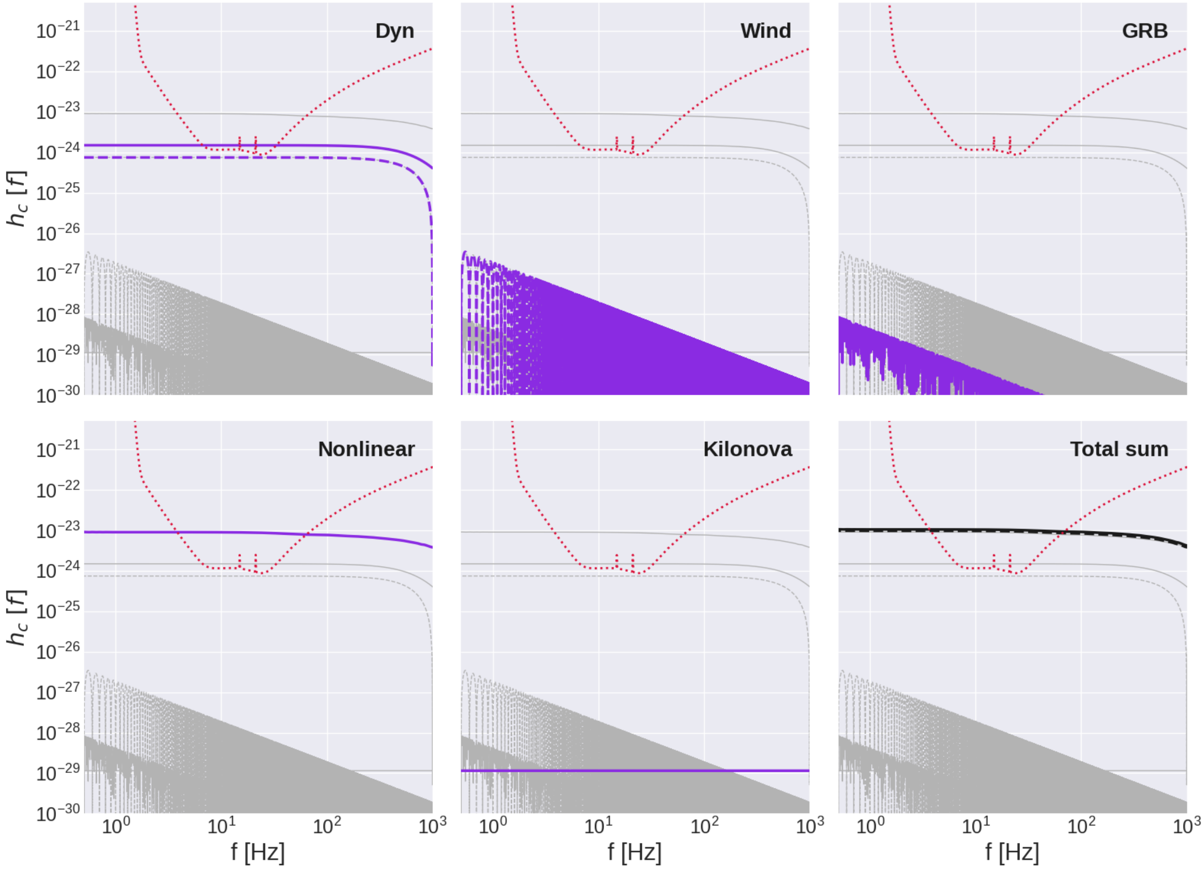


Figure 4.1: Components of the memory effect for GW170817, linear memory from dynamical ejecta, wind, GRB, and the kilonova, and the nonlinear memory. Each component is highlighted in purple and ET sensitivity curve in red. For the dynamical and wind ejecta, dotted and solid lines represent uniform and exponential models, respectively. The final panel shows the total signal, where nonlinear memory is the dominant component.

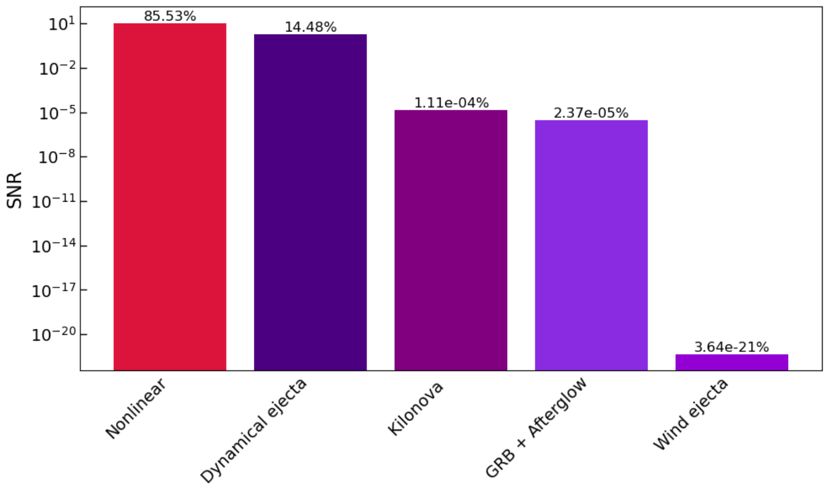


Figure 4.2: Individual contributions of the respective memory effects to the total SNR for an event similar to 170817. Percentages (top of bars) denote relative contribution per effect.

The effect of nonlinear memory on detectability is displayed in Fig. 4.3. Removing the nonlinear memory results in a drop of the SNR to 1.82 for a distance comparable to that of GW170817. Its impact is smaller at long distances because all memory effects decay like a Coulomb potential.

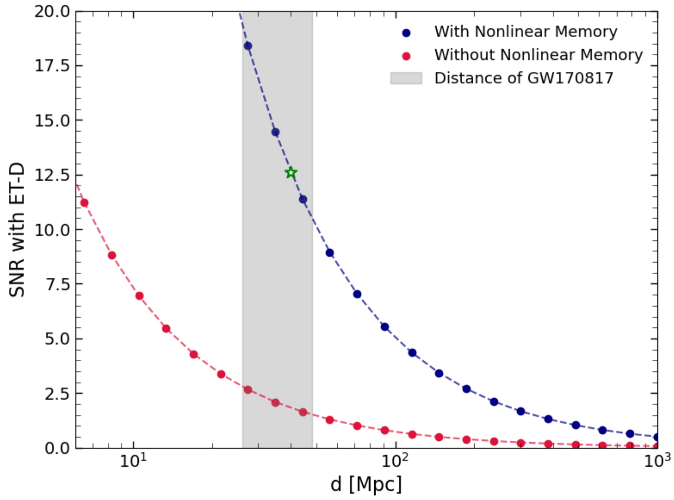


Figure 4.3: SNR values for a GW170817-like event including (blue) or not (red) the nonlinear memory. The grey region is the incertainty on the luminosity distance of GW170817, where the green star refers to a distance of 40 Mpc used in this work.

### 4.1.2 Parameter dependence of the SNR

One finding from the previous section is that the dynamical ejecta accounts for 15% of the total memory if geometry and the viewing angle are simplified, while the other ejecta are negligible. In this section, we examine the effect of modifying the properties of the dynamical ejecta on the SNR, still under these assumptions. To illustrate these results, we have generated SNR heatmaps for two different cases. The first uses parameter values within the theoretically expected range where the other memory contributions (ordinary and null) are summed, and the second examines only the memory contribution of the studied element to the SNR.

These SNR plots for the dynamical ejecta are shown in Fig. 4.4. It is not surprising to see that the memory increases for more massive and faster ejecta given Eq. (3.29). In the right-handed panel, the parameters used for 170817 (green star) indicate that the dynamical component's contribution to the SNR is higher than one. In a more optimistic scenario, the contribution of the dynamical ejecta could, in theory, increase to a SNR of 5 for $M_{\mathrm{ej,dyn}} = 10^{-2} M_{\odot}$ and $v_{\mathrm{ej,dyn}} = 0.4c$.

In a second step, we can revisit the memory of the GRB. As mentioned earlier, the low isotropic energy of the prompt is the primary reason for its low amplitude. Using heatmaps, we can investigate the effect of a more energetic GRB on the SNR. Based on the last two panels of Fig. 4.5, a minimum energy of $E_{\mathrm{GRB}} \sim 10^{52}$ erg would increase the SNR, as its individual contribution would be of the same order of magnitude as that of the nonlinear memory. Furthermore, the duration of the prompt phase directly affects detectability with ET. For a fixed energy, a longer GRB shifts the memory signal to lower peak frequencies, away from ET's optimal sensitivity around $10^2$ Hz. GRBs with durations between 1 and 100 s are thus more targeted by low-frequency detectors such as LISA.

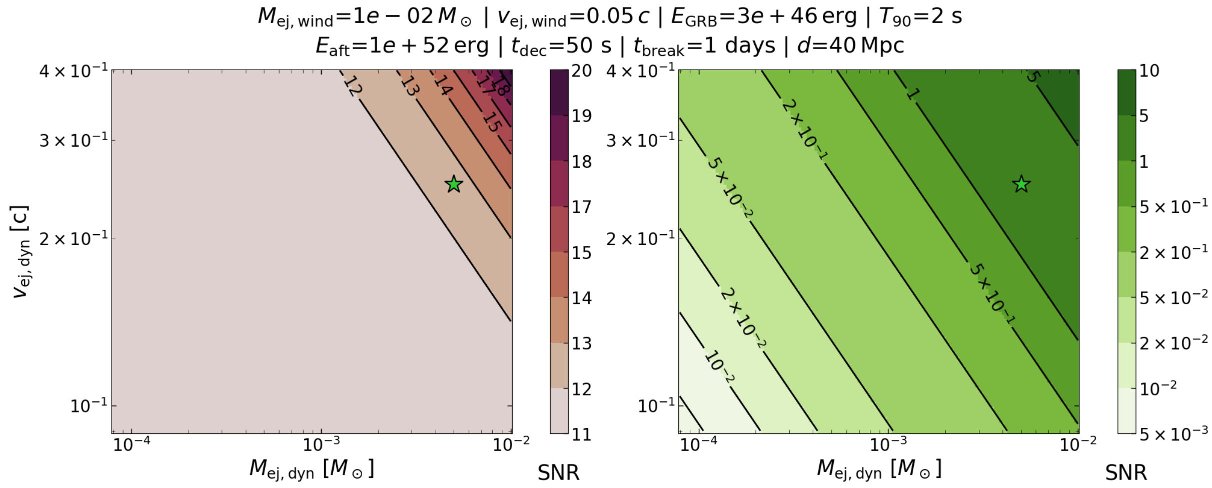


Figure 4.4: SNR heatmaps for the dynamical ejecta memory as a function of the ejected mass and its velocity, showing the cumulative SNR from all ejecta components (*left*) and the contribution from the dynamical ejecta alone (*right*). The remaining parameters are fixed to the values indicated in the title. The green star marks the parameter space of GW170817 and its color does not reflect its actual SNR value.

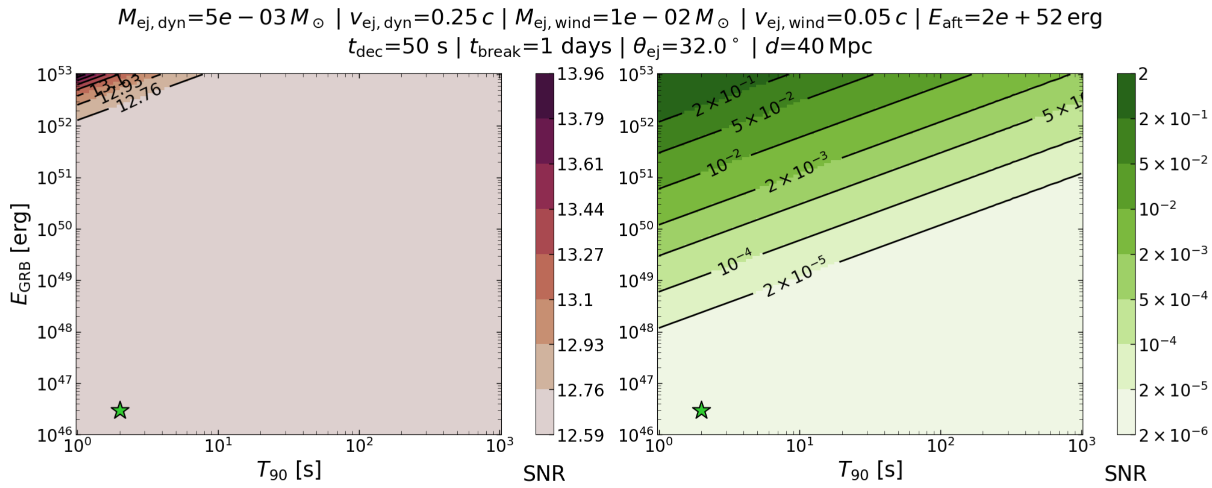


Figure 4.5: SNR heatmaps for the GRB memory as a function of the isotropic energy of the prompt emission and its duration, showing the cumulative SNR from all ejecta components (*left*) and the contribution from the prompt GRB alone (*right*). The remaining parameters are fixed to the values indicated in the title. The green star marks the case of GW170817.

## 4.2 GRB Population Framework with ET and LISA

This second part of the chapter investigates the detectability of memory effects sourced by GRBs and their afterglows. To probe the accessible parameter space of GRB sources, we consider four events whose properties are summarized in Table 4.2. Two of them have already been introduced: GRB 170817A and the BOAT [109, 110], the latter being presented in the introduction as the GRB with the highest known prompt emission energy recorded. The third event, GRB 250702B [111, 112], is the longest GRB detected, with a prompt duration of approximately seven hours spread over three distinct emission episodes. GRB 980425 [113, 114], associated with the supernova SN 1998bw, is included as the closest GRB ever observed. Finally, GRB 211211A [115] has been added because it is a GRB detection associated with a kilonova candidate, a case similar to GRB 170817A, but here no GW counterpart was found.

Table 4.2: Properties of selected GRBs

| Parameter | BOAT | GRB 250702B | GRB 980425 | GRB 170817A | GRB 211211A |
|---|---|---|---|---|---|
| Distance [Mpc] | 724 | 7093 | 36.9 | 40 | 350 |
| $E_{\rm GRB}$ [erg] | $1 \times 10^{55}$ | $2.2 \times 10^{54}$ | $6 \times 10^{47}$ | $3 \times 10^{46}$ | $7.6 \times 10^{51}$ |
| $E_{\rm aft}$ [erg] | $3 \times 10^{54}$ | $8 \times 10^{54}$ | $1 \times 10^{49}$ | $10^{52.2}$ | $5 \times 10^{52}$ |
| $T_{90}$ [s] | 600 | 25 000* | 30 | 2 | 51.37 |
| $\theta_{\rm ej}$ [°] | 0.2* | 65* | 29.5* | 32 | 30* |
| $\Delta h_{\rm GRB}$ | $8.5 \times 10^{-25}$ | $1.4 \times 10^{-23}$ | $1.5 \times 10^{-27}$ | $6.9 \times 10^{-29}$ | $2.00 \times 10^{-24}$ |
| $\Delta h_{\rm aft}$ | $2.5 \times 10^{-25}$ | $8.3 \times 10^{-23}$ | $2.5 \times 10^{-26}$ | $3.64 \times 10^{-23}$ | $1.31 \times 10^{-23}$ |
| SNR LISA | $7 \times 10^{-3}$ | $3.6 \times 10^{-5}$ | $6.8 \times 10^{-7}$ | $1.2 \times 10^{-5}$ | $8.1 \times 10^{-4}$ |
| SNR ET | $1.97 \times 10^{-3}$ | $3.33 \times 10^{-5}$ | $2.20 \times 10^{-6}$ | $2.10 \times 10^{-2}$ | $1.18 \times 10^{-3}$ |

**Notes**: Values marked with an asterisk (*) represent the average values found in papers. The distance of GRB 250702B has been converted from redshift ($z = 1.036$) using $H_0 = 67.66$ km s$^{-1}$ Mpc$^{-1}$ (`Planck18` of `Astropy` [116]). For all GRBs, we set $\Gamma = 100$ ($\beta \simeq 0.99995$).

The values of $t_{\rm dec}$ and $t_{\rm break}$ are not well constrained, and the uncertainty surrounding $\gamma_0$ and the density of the medium means it is not possible to specify a precise duration for the afterglow used to compute the memory. However, it is estimated that $t_{\rm break}$ could occur around one day after the start of the prompt emission [104]. Thus, we will use an afterglow duration of one day. It will become clear later why this value does not affect much the SNR value (especially with LISA) for a realistic afterglow.

The SNR values reported in Table 4.2 were computed using the LISA sensitivity curve for frequencies between $5 \times 10^{-5}$ Hz and 1 Hz. The lower bound is critical because, for configurations with characteristic times larger than $2 \times 10^4$ s (which is equivalent to $\sim 0.22$ days), their memory will decline before the minimum frequency required for SNR computation is reached. For ET, minimum and maximum frequencies are 1 Hz and $10^4$ Hz, respectively.

Although the GRBs listed in Table 4.2 are extreme cases in terms of energy, duration or distance, their SNR remains very low. As illustrated in Fig. 4.6, which shows both the temporal evolution and the frequency-domain representation overlaid on the LISA and ET sensitivity curves, all four GRBs lie far below the sensitivity threshold, consistently with the low SNR values obtained. However, this estimate for LISA remains approximate. A complete treatment should account for the position of the LISA constellation compared to the wave propagation, the duration of the observation window, and the projection of the signal onto each arm of the detector. These effects can either increase or decrease the effective SNR depending on the source configuration, and dedicated pipelines exist to handle them properly [117]. Here, we acknowledge that these factors are neglected, and a more rigorous SNR computation represents a direction for improving our current analysis.

Moreover, Fig. 4.6 shows that the frequency evolution is set by the component with the largest amplitude at each frequency. The afterglow decay (grey line) occurs at $\sim 10^{-5}$ Hz for a one day duration, while the GRB decay (coloured lines) falls around LISA's sensitivity. In the frequency range between the two vertical lines, we observe three regimes:

- Afterglow-dominated (GRB 170817A): the afterglow drives the whole evolution,
- Mixed (GRB 250702B): both components contribute comparably,
- GRB-dominated (BOAT, GRB 980425, GRB 211211A): the GRB alone drives the evolution, hence producing a plateau up to $1/T_{90}$ Hz.

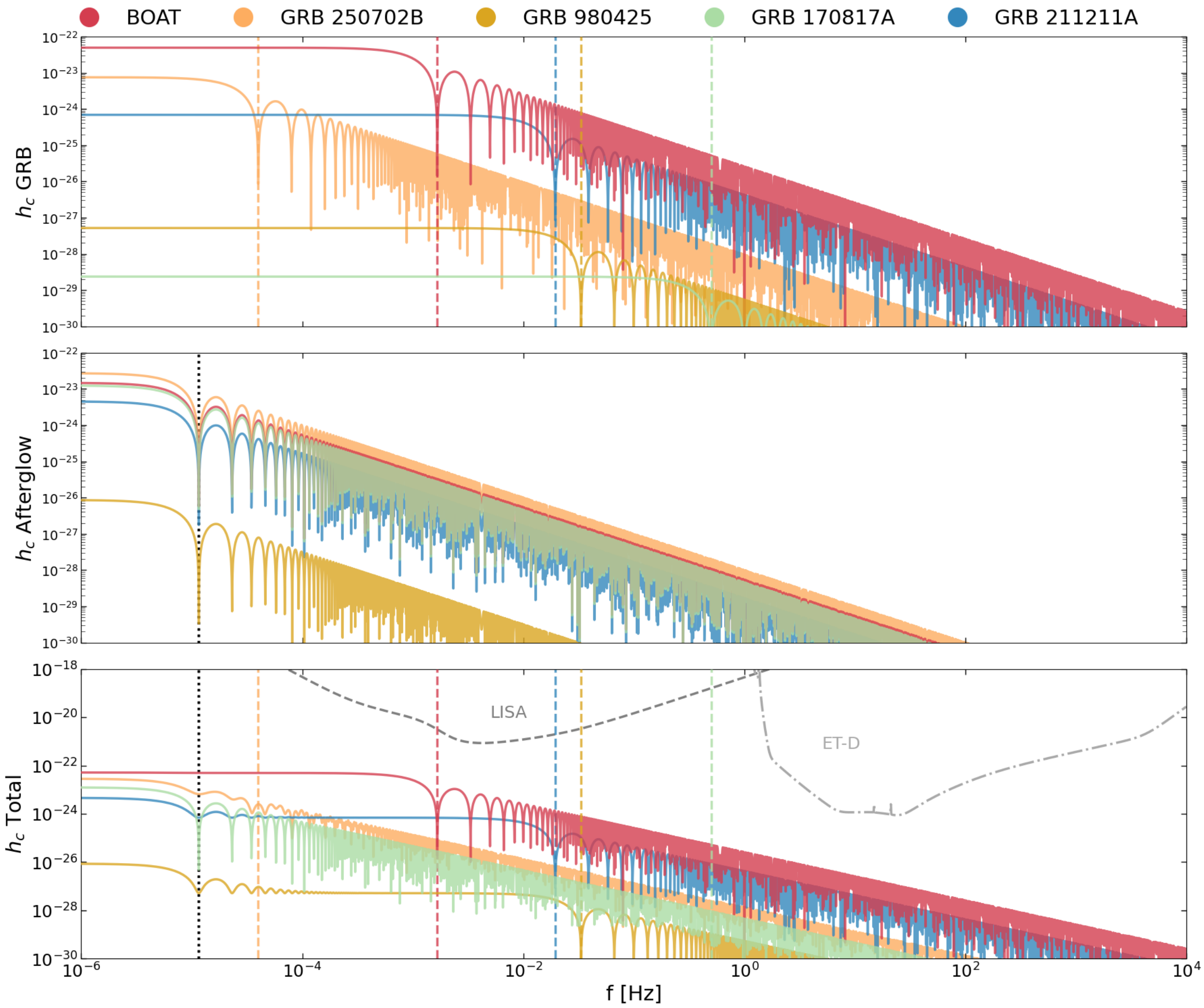


Figure 4.6: Characteristic strain for the prompt (*top*), the afterglow (*middle*) and the combined emission (*bottom*) of the selected GRBs presented in Table 4.2 for a generic afterglow duration of 1 day and $\Gamma = 100$. The colored vertical lines refers to the inverse of $T_{90}$ of each GRB and the grey one to the inverse of the afterglow duration. For the last plot, sensitivity curves of LISA and ET-D are displayed in grey.

### 4.2.1 Synthetic population

As in the first part of this chapter, we can consider configurations that would produce a GRB and afterglow memory and investigate their SNR. In this section, we will delve deeper by producing SNR heatmaps and overlaying a "realistic" population of GRBs. The point is to check directly on the heatmaps whether there are any potential configurations that the interferometer might be able to detect. A survey of BNS and associated ejecta was not conducted in the previous section because there was only a single observation of such a system. For GRBs and their afterglows, numerous detections have been made, which explains our different approach. Although it is possible to generate populations of GRBs based on theoretical models, there is currently no single model that can unambiguously describe all the population of detected GRBs and their afterglows, simply because we do not yet have a sufficiently clear and complete understanding of the physics behind these phenomena[2].

To ensure that our population is as realistic as possible, we will base it on the detected GRBs, and in particular on the four extreme cases mentioned above. For the isotropic energy and the distance, a lognormal distribution has been employed with minimum and maximum allowed values from Table 4.2. The distribution of prompt duration is described as a bimodal lognormal accounting for both short and long GRBs and based on a recent review (2020) of the fourth *Fermi*/GBM gamma-ray burst catalog [118]. Our duration of the afterglow, $t_{\rm dec}$ and $t_{\rm break}$, follow a lognormal center on 100 s and 1 day respectively. The observing angle $\theta_{\rm ej}$ and the velocity of the jet $\beta$ are taken from an uniform distribution between $[0, \pi/2]$ and $[0.9, 1]$ respectively. A sample of 10 000 points has been drawn from each distribution to form our synthetic population, with the characteristic resumed in Table 4.3.

Table 4.3: Optimistic population parameters for GRBs and afterglows

| Parameter | Distribution | Mean | Std | Min | Max |
|---|---|---|---|---|---|
| $E_{\rm GRB}$ [erg] | Lognormal | $1.06 \times 10^{53}$ | $4.49 \times 10^{53}$ | $2.37 \times 10^{47}$ | $9.47 \times 10^{54}$ |
| $T_{90}$ [s] | Bimodal lognormal | $3.73 \times 10^{1}$ | $5.18 \times 10^{1}$ | $1.00 \times 10^{-1}$ | $4.96 \times 10^{2}$ |
| $E_{\rm aft}$ [erg] | Lognormal | $1.32 \times 10^{53}$ | $9.34 \times 10^{53}$ | $1.00 \times 10^{50}$ | $5.08 \times 10^{55}$ |
| $t_{\rm dec}$ [s] | Lognormal | $1.60 \times 10^{2}$ | $2.20 \times 10^{2}$ | $3.67 \times 10^{-2}$ | $1.00 \times 10^{3}$ |
| $t_{\rm break}$ [s] | Lognormal | $1.73 \times 10^{5}$ | $1.99 \times 10^{5}$ | $8.64 \times 10^{3}$ | $8.63 \times 10^{5}$ |
| $d$ [pc] | Lognormal | $1.79 \times 10^{9}$ | $2.24 \times 10^{9}$ | $4.00 \times 10^{7}$ | $1.00 \times 10^{10}$ |
| $\theta_{\rm ej}$ [deg] | Uniform | $7.85 \times 10^{-1}$ | $4.54 \times 10^{-1}$ | $3.21 \times 10^{-5}$ | 1.57 |
| $\beta$ | Uniform | 0.95 | $2.89 \times 10^{-2}$ | 0.9 | 1 |

**Note:** $T_{90}$ follows a bimodal lognormal distribution to represent a population comprising short and long GRBs (short: $\log T_{90} \sim \mathcal{N}(0.0208, 0.367)$, long: $\log T_{90} \sim \mathcal{N}(1.476, 0.189)$) [118].

### 4.2.2 Parameter dependence of the SNR with LISA

In this part, we examine the SNR heatmaps across different parameter pairs for the LISA detector. We omit the ET heatmaps for clarity, as they exhibit qualitatively similar behavior. Moreover, focusing on LISA is more illustrative for our purposes, given its enhanced relevance for detecting the low-frequency afterglow component.

[2]For instance, long and short GRBs originate from entirely different progenitors and their prompt emission, jet structure, and circumburst environments differ so fundamentally that no unified population model can be straightforwardly applied to both classes simultaneously.

Before discussing the results, we briefly explain how the data is displayed in the next figures. The black contour lines represent SNR isovalues, with the red line marking the SNR = 1 isovalue, where the signal is no longer completely overwhelmed by noise. The GRB population is represented by the white contours, with the outer line encompassing 99% of the population. For clarity, the GRB prompt emission and afterglow contributions are investigated separately, as this allows the effect of each component on the SNR to be more readily identified in the heatmaps.

### Prompt case

First, we investigate the prompt emission for a constant afterglow (with the fixed parameters in the title). Fig. 4.7 depicts how the SNR varies with different prompt energies as a function of distance or the $T_{90}$ time. Only nearby and highly energetic GRBs produce a SNR close to one. A closer examination for our population yields a distance between 30 and 100 Mpc, a maximum duration of 70 seconds, and an energy of $2.5 \times 10^{54}$ erg that approach SNR = 1. For ET and under the same conditions, achieving an SNR of one requires a prompt energy one order of magnitude lower.

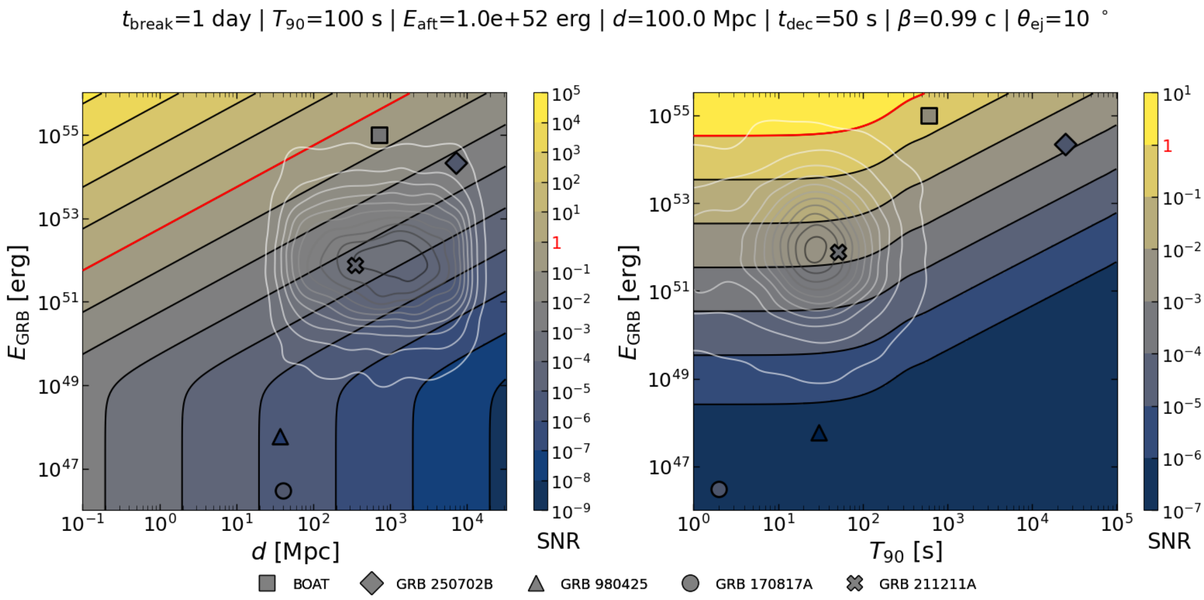


Figure 4.7: SNR heatmaps for the GRB case for a variation of the isotropic energy as a function of distance (*left*) and prompt duration (*right*). Black contour lines represent SNR isovalues with the red contour marks SNR = 1. White contours show the GRB population distribution, with the outermost contour enclosing 99% of the population.

The dependence of the SNR on energy and distance can be understood from the definition of the GRB memory amplitude ($\Delta h_{\mathrm{GRB}} \propto E/d$). Regarding the prompt duration, we observe that for $T_{90} \gtrsim 200$ s, the SNR decreases for a constant $E_{\mathrm{GRB}}$. This can be explained by the fact that at longer characteristic times, the frequency decay occurs before the typical LISA frequency around $10^{-2}$ Hz. To compensate for this decrease in SNR, a larger 'height' in $h_c$ is required, and thus a larger energy $E_{\mathrm{GRB}}$, which explains the appearance of a positive slope at large values of $T_{90}$.

### Afterglow case

Now we focus on the afterglow phase with fixed parameters for prompt phase. If we choose to examine parameter pairs similar to those in the previous heatmap, specifically distance and jet-break[3] time, we obtain the heatmaps shown in Fig 4.8.

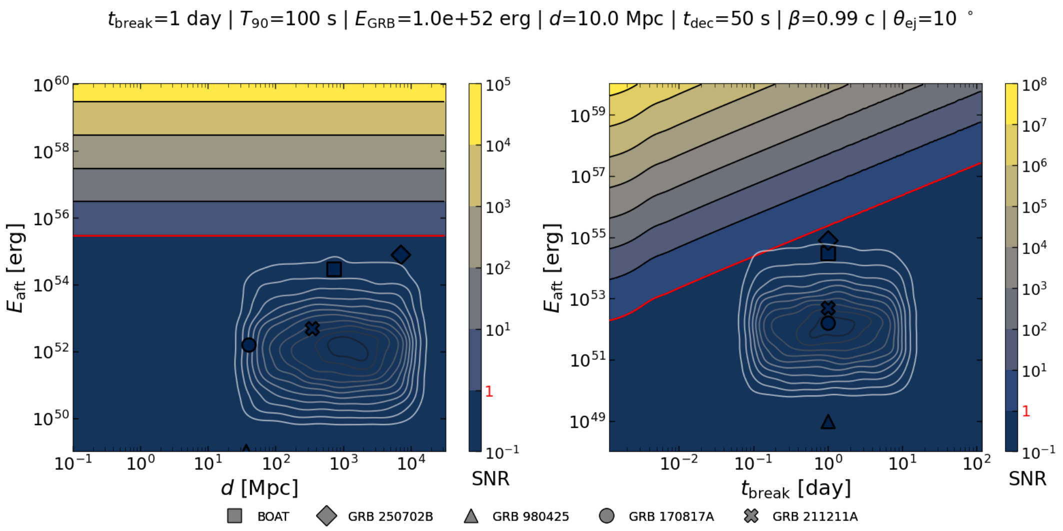


Figure 4.8: SNR heatmaps for a variation of the isotropic energy of the afterglow as a function of distance (*left*) and afterglow duration (*right*) with a fixed $t_{\rm dec} = 50$ s. From the perspective of the population (white lines), the SNR varies slightly with the properties of the afterglow.

The trend with distance differs from that observed in GRBs. The heatmap is horizontally stratified, indicating that the energy of the afterglow does not affect detectability. This is because the duration of the afterglow for the left frame is fixed at one day, so the portion within LISA's frequency range corresponds to the decay of the memory effect. If we increase the height of the rise by increasing $E_{\rm aft}$, then the slope becomes steeper, which explains the shape of the heatmap.

In the right-hand panel, the duration of the afterglow is varied. We can see that the horizontal plateau observed in Fig. 4.7 is no longer present. The SNR gradient points toward the upper-left corner, indicating more energetic and shorter afterglows have higher SNR. We also note that assuming an optimistic afterglow duration of one day was not a poor approximation. For longer durations and afterglow energies similar to the population, the SNR varies slightly, meaning that $t_{\rm break}$ remains a valid approximation in our model for calculating the SNR in LISA. If we were dealing with a lower-frequency detector, this approximation would no longer be valid.

Fig. 4.9 provides a clearer picture of the trend in LISA's SNR as a function of afterglow duration. The heatmap shows only values of $t_{\rm dec} < t_{\rm break}$ to ensure that the start of the afterglow does not occur before its end. The orange curves indicate afterglow durations $(t_{\rm break} - t_{\rm dec})$ for characteristic values of one minute, one hour, and one day. It can be seen that for durations exceeding one hour, the SNR decreases sharply because, once again, the characteristic strain drops at a frequency lower than LISA's sensitivity band.

[3]For a fixed decelerating time $t_{\rm dec}$, the quantity $t_{\rm break} - t_{\rm dec}$ is the analogous of $T_{90}$ for the afterglow memory.

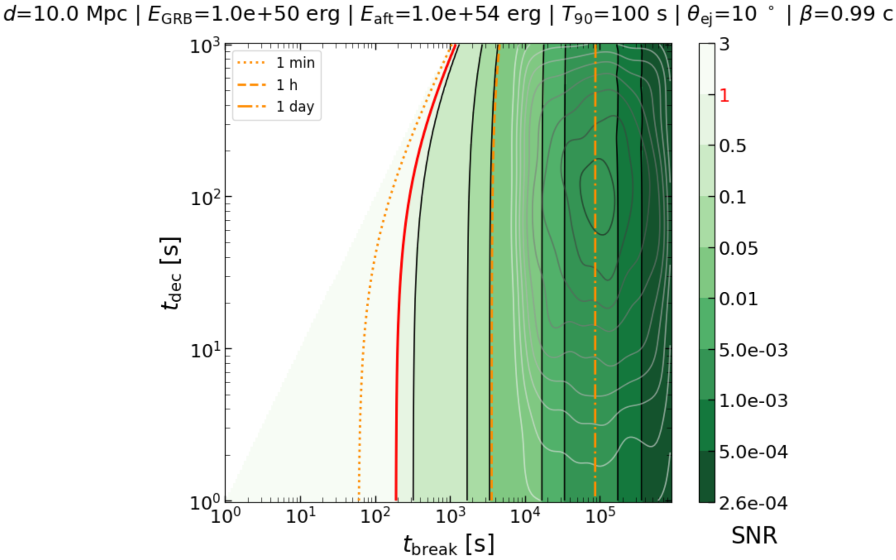


Figure 4.9: SNR heatmap for the duration of the afterglow for LISA. The orange lines represent durations of one minute, one hour, and one day, with the latter corresponding to the average duration of the generated population.

### Anti-beaming influence

Finally, Fig. 4.10 shows the effect of anti-beaming on the SNR. When $\beta \sim 0.75$, the SNR is maximized at a viewing angle of 65°. As $\beta$ decreases, this angle also decreases. Note that for $\beta = 0.99$, the minimum angle optimizing the SNR is around 10 degrees, whereas for $\beta = 1$, it is maximized for face-on observation. The disappearance of the anti-beaming effect is explained by the behavior of $\Theta(\theta)$ for $\beta = 1$, which takes the form:

$$\Theta(\theta) = \frac{\sin^2\theta}{1-\cos\theta} = 1 + \cos(\theta) \;, \tag{4.1}$$

which is maximized at $\theta = 0$.

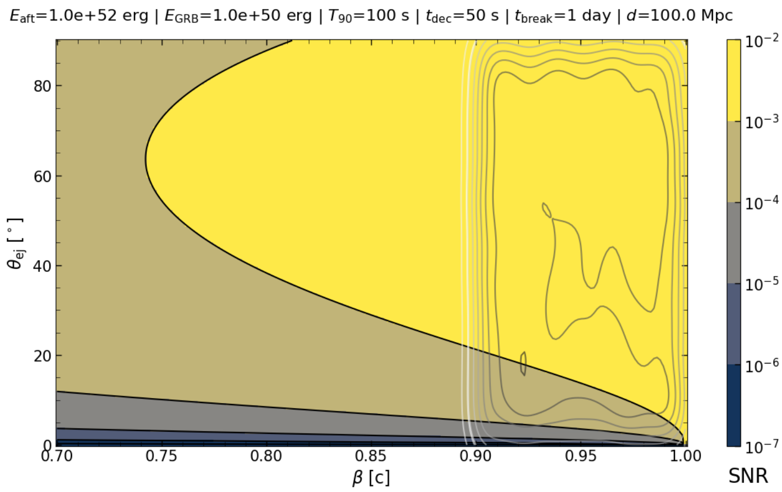


Figure 4.10: SNR heatmap indicating the SNR dependence with respect to the viewing angle and the jet velocity $\beta$ for LISA. For small values of $\beta$, the emission is primarily edge-on, whereas as $\beta \to 1$, configurations close to face-on maximize the SNR. This trend is the anti-beaming effect mentioned in the section 3.2. Note that the SNR is maximized at $\theta = 0$ only when $\beta = 1$, as discussed above.

## 4.3 SNR analysis of the synthetic GRB population

In this last section, we focus on potential prompt/afterglow configurations within the population that could produce a large SNR in ET and LISA. To do this, we generate a new population of $10^4$ samples by drawing from the original parameter distributions. Since we have eight randomized parameters, it is likely that certain regions of the parameter space will not be covered by a traditional sampling method. One way to avoid this curse of dimensionality is to use the Quasi-Monte Carlo (QMC) method to generate our configurations. Unlike traditional Monte Carlo methods that rely on independent, identically distributed points, QMC utilizes a deterministic framework where the placement of each point is mathematically linked to the others. This inherent lack of independence allows the algorithm to better fill the gaps in the parameter space.

After computing the SNR for both detectors, we obtain its distribution displayed in Fig. 4.11. To determine the influence of each parameter on the SNR across the synthetic population, the Spearman correlation coefficient $\rho$ was computed. Unlike the Pearson coefficient, which only captures linear relationships, this metric accounts for any monotonic dependence between the variable and the SNR, making it more adapted for our memory model.

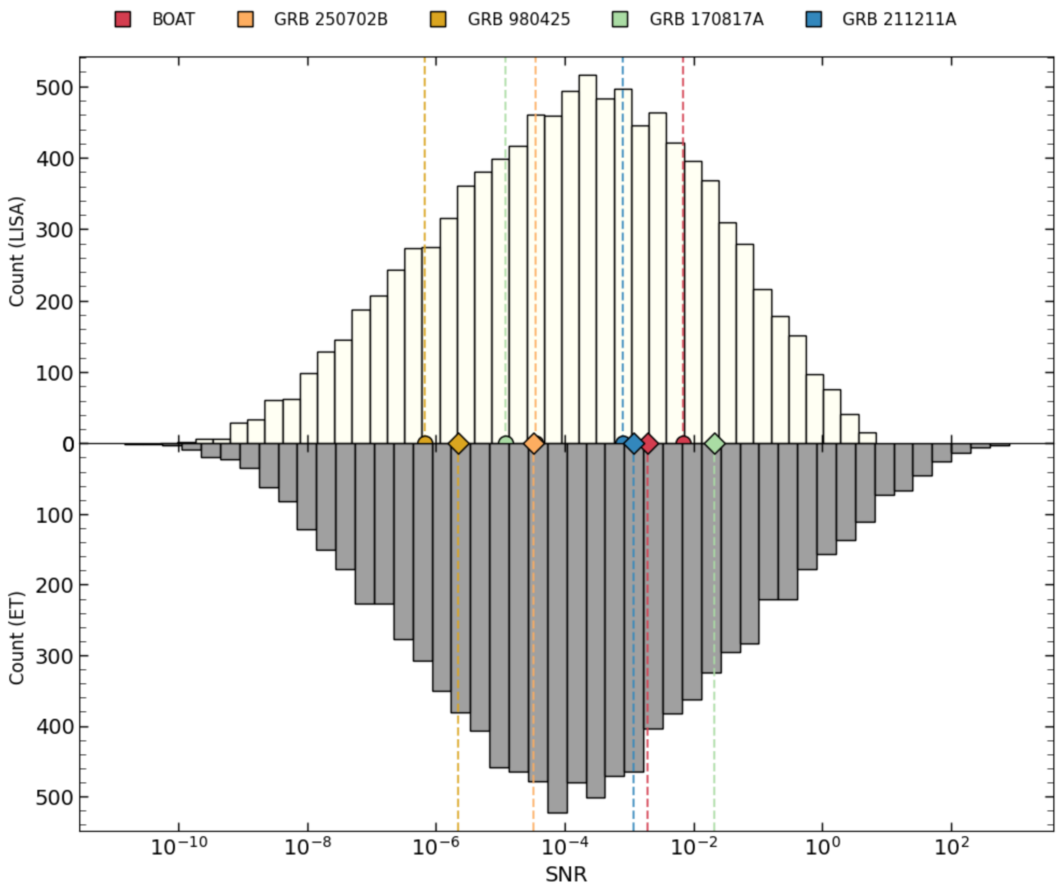


Figure 4.11: Histogram of the SNR in LISA (*top*) and ET (*bottom*) for the randomized population, with the specific detected GRBs. Note that ET achieves higher SNR configurations for the same population compared to LISA.

For LISA, 147 configurations have an SNR larger than one and the top five are listed in the Table 4.4. The prompt energy $E_{\text{GRB}}$ exhibits the strongest positive correlation, which explains why the highest SNR configurations tend to have prompt energies close to the population maximum of $10^{55}$ erg. Distance, as expected, shows a negative correlation. Additionally, the afterglow energy demonstrates a non-negligible positive correlation. Physically, this happens because the afterglow phase impacts the low-frequency regions, directly influencing the signal detectability near LISA's sensitivity band. Beyond these mains drivers, the remaining parameters are only weakly correlated with the SNR, suggesting that the detectability (based on the synthetic population) is primarily driven by the prompt and afterglow energies and proximity. Notably, the correlation coefficient associated with the afterglow duration is near zero and negative. This is consistent with the fact that the population was restricted to durations of at least 0.1 days, a lower bound that prevents the afterglow memory from being effectively shifted into LISA's sensitivity band, thereby limiting the range of this parameter and its leverage on the SNR.

Table 4.4: GRB parameters for the 5 best sampled configurations for LISA

| Parameter | $\mathcal{C}_1$ | $\mathcal{C}_2$ | $\mathcal{C}_3$ | $\mathcal{C}_4$ | $\mathcal{C}_5$ | $\rho$ |
|---|---|---|---|---|---|---|
| $E_{54,\mathrm{GRB}}$ [erg] | 9.84 | 9.48 | 8.93 | 7.42 | 8.17 | 0.7352 |
| $T_{90}$ [s] | 3.278 | 0.109 | 1.978 | 0.291 | 5.996 | -0.0433 |
| $E_{\mathrm{aft}}$ [erg] | $6.99 \times 10^{50}$ | $3.14 \times 10^{55}$ | $1.29 \times 10^{52}$ | $2.10 \times 10^{51}$ | $1.62 \times 10^{53}$ | 0.3606 |
| $T_{\mathrm{aft}}$ [days] | 0.377 | 0.230 | 1.317 | 3.709 | 0.673 | -0.1223 |
| $d$ [Mpc] | 41.35 | 47.57 | 48.62 | 43.11 | 42.19 | -0.3268 |
| $\theta_{\mathrm{ej}}$ [deg] | 79.08 | 57.50 | 68.34 | 60.47 | 71.38 | -0.0220 |
| $\beta$ | 0.984 | 0.914 | 0.941 | 0.937 | 0.917 | 0.0146 |
| SNR | 6.75 | 5.75 | 5.33 | 5.27 | 5.09 | / |

**Note:** $E_{54,\mathrm{GRB}} = E_{\mathrm{GRB}} \times 10^{-54}$ and $T_{\mathrm{aft}} = t_{\mathrm{break}} - t_{\mathrm{dec}}$.

For ET, 582 configurations yield an SNR larger than one, generally exhibiting higher values than those obtained for LISA. The five most detectable GRBs in ET are listed in Table 4.5. Notably, configurations $\mathcal{C}_2$ and $\mathcal{C}_4$ from the LISA analysis are also present in the ET top five, but with larger SNRs, a contrast partially driven by ET's higher sensitivity. Furthermore, the prompt duration is just as important as the distance for ET detectability, with both parameters showing similar correlation coefficients ($\rho \approx -0.28$). Indeed, the prompt durations for all five of the best configurations are less than one second[4]. Physically, this is expected: since ET is highly sensitive to frequencies above 10 Hz, emissions occurring on timescales shorter than 0.1 s fall within its optimal band.

Table 4.5: GRB parameters for the 5 best sampled configurations for ET

| Parameter | $\mathcal{C}_1$ | $\mathcal{C}_2$ | $\mathcal{C}_3$ | $\mathcal{C}_4$ | $\mathcal{C}_5$ | $\rho$ |
|---|---|---|---|---|---|---|
| $E_{54,\mathrm{GRB}}$ [erg] | 9.48 | 7.55 | 4.95 | 9.07 | 7.42 | 0.7846 |
| $T_{90}$ [s] | 0.109 | 0.129 | 0.134 | 0.196 | 0.291 | -0.2830 |
| $E_{\mathrm{aft}}$ [erg] | $3.14 \times 10^{55}$ | $1.65 \times 10^{50}$ | $3.62 \times 10^{52}$ | $7.66 \times 10^{53}$ | $2.10 \times 10^{51}$ | 0.2444 |
| $T_{\mathrm{aft}}$ [days] | 0.230 | 3.156 | 7.344 | 1.771 | 3.709 | -0.0854 |
| $d$ [Mpc] | 47.57 | 61.53 | 50.16 | 56.53 | 43.11 | -0.2867 |
| $\theta_{\mathrm{ej}}$ [deg] | 57.50 | 61.29 | 73.68 | 86.88 | 60.47 | -0.0182 |
| $\beta$ | 0.914 | 0.936 | 0.990 | 0.963 | 0.937 | 0.0126 |
| SNR | 797.48 | 411.67 | 326.89 | 318.93 | 280.99 | / |

**Note:** $E_{54,\mathrm{GRB}} = E_{\mathrm{GRB}} \times 10^{-54}$ and $T_{\mathrm{aft}} = t_{\mathrm{break}} - t_{\mathrm{dec}}$. Although $\mathcal{C}_4$ has a larger prompt energy than $\mathcal{C}_2$ and $\mathcal{C}_3$, its longer prompt duration (and larger distance relative to $\mathcal{C}_3$) results in a smaller SNR.

[4] Note that a GRB with duration as short as 0.1 s has already been detected [119].

Additionally, these high SNRs are strongly dependent on the chosen rising phase model. For the prompt and afterglow memory, we adopted a uniform model for the step function $s(t, \tau) = t/\tau$. This produces a gradual decay at frequencies $f \gtrsim 1/\tau$, meaning the signal maintains a sufficient amplitude to contribute to the total SNR at high frequencies (as illustrated in Fig. 4.12). If an exponential decay model were used instead, the high-frequency decay would be much steeper within ET's sensitive band, resulting in a lower SNR. It should be emphasized that our current framework relies on toy-models and more rigorous waveform modeling would be required to precisely quantify these uncertainties. Finally, as shown in Table 4.5, while the prompt energy remains a primary driver of detectability, the afterglow energy plays a smaller role for ET than for LISA, as ET's high-frequency sensitivity band is less sensitive to the low-frequency afterglow component.

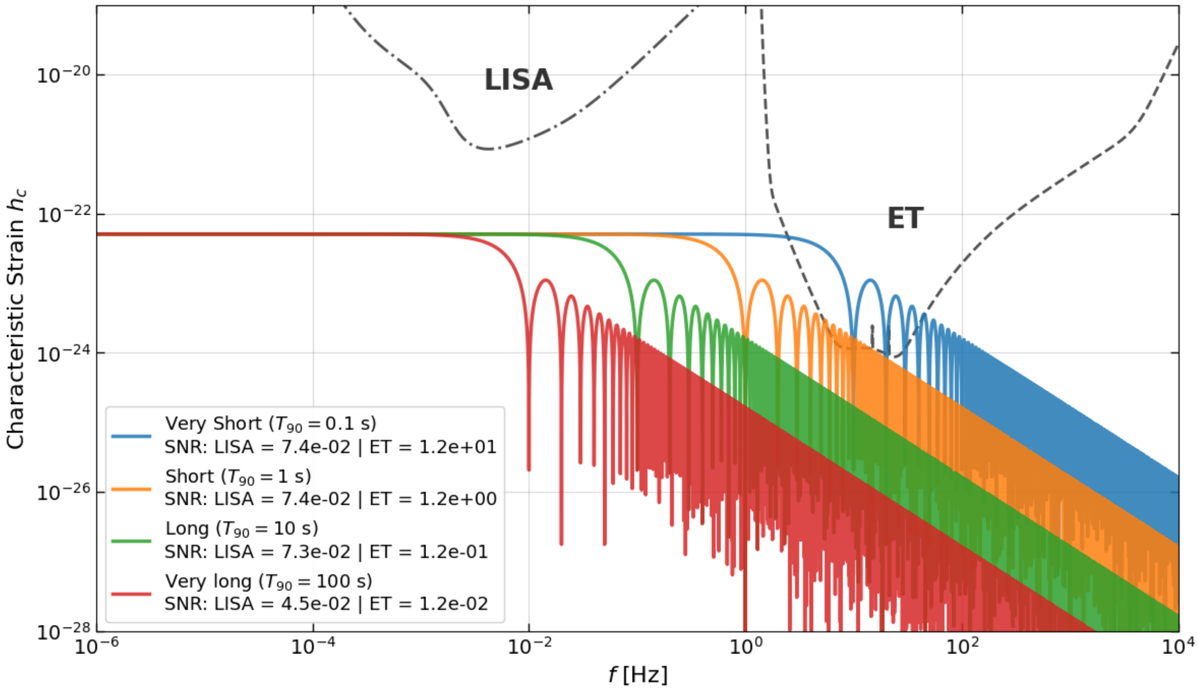


Figure 4.12: Comparison of the ET and LISA SNR for a GRB with $E_{\mathrm{GRB}} = 10^{55}$ erg, assuming no afterglow component, across varying prompt durations ($T_{90}$). In the uniform emission model ($s(t, \tau) = t/\tau$), the signal decay occurs at frequencies below ET's optimal sensitivity band, yet still contributes to the total SNR. An exponential model would produce a steeper cutoff, resulting in a lower overall SNR. The SNR in ET also exhibits a stronger dependence on the prompt duration than in LISA.

The results presented here indicate that memory from GRBs would be detectable by ET and LISA only for sources with extreme joint properties. The prompt energy must approach that of the BOAT, and the source distance must be comparable to that of GRB 170817A. For ET in particular, very short prompt durations ($\sim 0.1$ s) further enhance detectability. While GRBs with individually extreme parameters have been observed, no event combining all such characteristics simultaneously has been detected yet.

# Conclusion

Through this work, we have investigated how the memory effect arises and alters the GW of a BNS. Following appropriate numerical processing, it was possible to estimate, based on detector sensitivity curves, whether the memory signal would be detectable in future ET and LISA interferometers. In particular, we found that in a case similar to GW170817, only the nonlinear memory and the dynamical ejecta contribute in the SNR of ET. Subsequently, the memory produced by the GRB and its afterglow counterpart has been investigated with a toy-model model for the first time. Based on an optimistic population study, we found that nearby GRBs (at distances of 10 to 100 Mpc) with an isotropic prompt energy larger than $2.5 \times 10^{54}$ erg and lasting less than 100 s would fall within LISA's optimal sensitivity range. For ET, detectability requires lower prompt energies, approximately one order of magnitude below those needed for LISA. These configurations yield an SNR of up to 6 for LISA, above the detection threshold of SNR $\sim 3$. An equivalent analysis conducted for ET revealed configurations with higher SNRs, surpassing the threshold of SNR $\sim 8$ needed to claim a detection. Furthermore, ET should be particularly sensitive to very short GRBs, typically lasting from less than 0.1 up to 1 s. While this suggests short GRBs could be detected by ET, we emphasize that this prospect remains highly dependent on the adopted model. Finally, regarding the extended emissions, the kilonova and afterglow signals evolve over timescales that are too long to be effectively detected by LISA.

These first results are encouraging, though approximations have been used. For example, one path for improvement would be to move away from the point-particle approximation for dynamical ejecta, wind and the GRB. For the former two, modeling the density and velocity fields would be more realistic. For the GRB, we implemented two realistic GRB geometries (top-hat and structured) at a late stage of the work. It would be worth comparing their modeling on the resulting SNR. Furthermore, tidal effects between NSs have been neglected. A study of the impact of matter effects is presented in [77] for the nonlinear memory solely, and demonstrates that more deformable systems have a lower peak memory amplitude. A case study incorporating tidal effects for nonlinear and the ordinary memory on the dynamical ejecta would be a further avenue to explore. Finally, we have seen that only one approximant (NRHybSur3dq8_CCE) accounts for the nonlinear memory effect in the modeled waveform. While this has not been explored in the master's thesis, it is worth noting that the primary purpose of theoretical approximants is to match data from which CBC parameters are inferred. Developing an approximant that incorporates both the nonlinear memory and relevant linear contributions, such as those from a joint GRB detection, would provide a means to assess whether such a model better reproduces the detected GWs. In this regard, multi-wavelength observations play a crucial role, as they independently constrain source parameters such as the jet geometry and viewing angle, which directly inform memory modeling.

Looking ahead, the next generation of GW detectors is expected to become operational around 2030, opening a realistic window for the first direct detection of the memory effect.

Appendix A

# Supplementary material

## A.1 Derivation of the linearized EFE

The linearized Einstein equations for the gothic metric can be derived as follows, starting from the Christoffel symbols and the Riemann tensor at first neglecting terms of the order of $\mathcal{O}(h^2)$ :

$$\Gamma_{\mu\nu\lambda} = \frac{1}{2}\left(\partial_\nu g_{\lambda\mu} + \partial_\lambda g_{\nu\mu} - \partial_\mu g_{\nu\lambda}\right) \tag{A.1}$$

$$\Rightarrow R_{\mu\nu\rho\sigma} = \partial_\sigma \Gamma_{\mu\nu\rho} - \partial_\rho \Gamma_{\mu\nu\sigma} = -\frac{1}{2}\left(\partial_\rho\partial_\nu h_{\mu\sigma} + \partial_\sigma\partial_\mu h_{\nu\rho} - \partial_\sigma\partial_\nu h_{\mu\rho} - \partial_\rho\partial_\mu h_{\nu\sigma}\right) \tag{A.2}$$

The Ricci tensor and scalar can be computed

$$\begin{cases} R_{\mu\nu} = -\frac{1}{2}(\Box h_{\mu\nu} + \partial_\mu\partial_\nu h - \partial_\mu\partial_\rho h^\rho_\nu - \partial_\rho\partial_\nu h^\rho_\mu) \\ R = -\Box h + \partial_\mu\partial_\nu h^{\mu\nu} \end{cases} \tag{A.3}$$

Based on these two factors, the tensor $G_\mu\nu$ can be calculated and reads:

$$\begin{aligned} G_{\mu\nu} &= R_{\mu\nu} - \frac{1}{2}\eta_{\mu\nu} R \\ &= -\frac{1}{2}(\Box h_{\mu\nu} + \partial_\mu\partial_\nu h - \partial_\mu\partial_\rho h^\rho_\nu - \partial_\rho\partial_\nu h^\rho_\mu) - \frac{1}{2}\eta_{\mu\nu}(-\Box h + \partial_\alpha\partial_\beta h^{\alpha\beta}) \end{aligned} \tag{A.4}$$

Now using the definition of the trace-reversed metric $\bar{h}$ from Eq. (1.23), the relation is transformed into

$$\begin{aligned} -2G_{\mu\nu} &= \Box\bar{h}_{\mu\nu} + \partial_\mu\partial_\nu\bar{h} - \partial_\mu\partial_\rho\bar{h}^\rho_\nu - \partial_\rho\partial_\nu\bar{h}_\mu^{\ \rho} - \eta_{\mu\nu}\Box\bar{h} + \eta_{\mu\nu}\partial_\alpha\partial_\beta\bar{h}^{\alpha\beta} \\ &\quad + \frac{1}{2}\eta_{\mu\nu}\Box\bar{h} + \frac{1}{2}\eta^\rho_\nu\partial_\mu\partial_\rho\bar{h} + \frac{1}{2}\eta_\mu^{\ \rho}\partial_\rho\partial_\nu\bar{h} + \eta_{\mu\nu}\eta^{\alpha\beta}\partial_\alpha\partial_\beta\bar{h} \\ &= \Box\bar{h}_{\mu\nu} - \partial_\mu\partial_\rho\bar{h}^\rho{}_\nu - \partial_\rho\partial_\nu\bar{h}_\mu^{\ \rho} + \eta_{\mu\nu}\partial_\alpha\partial_\beta\bar{h}^{\alpha\beta} \end{aligned} \tag{A.5}$$

which yields Eq. (1.31).

## A.2 Landau-Lifshitz pseudotensor

The Landau-Lifshitz pseudotensor $\tau^{ik}$ in terms of the Christoffel symbols and the metric takes the form [75]

$$
\begin{aligned}
\tau^{ik} = \frac{c^4}{16\pi G}\Big\{ & \left[2\Gamma^n_{lm}\Gamma^p_{np} - \Gamma^n_{lp}\Gamma^p_{mn} - \Gamma^n_{ln}\Gamma^p_{mp}\right](g^{il}g^{km} - g^{ik}g^{lm}) \\
& + g^{il}g^{mn}\left(\Gamma^k_{lp}\Gamma^p_{mn} + \Gamma^k_{mn}\Gamma^p_{lp} - \Gamma^k_{lp}\Gamma^p_{lm} - \Gamma^k_{lm}\Gamma^p_{np}\right) \\
& + g^{kl}g^{mn}\left(\Gamma^i_{lp}\Gamma^p_{mn} + \Gamma^i_{mn}\Gamma^p_{lp} - \Gamma^i_{lp}\Gamma^p_{lm} - \Gamma^i_{lm}\Gamma^p_{np}\right) \\
& + g^{lm}g^{np}\left(\Gamma^i_{ln}\Gamma^k_{mp} - \Gamma^i_{lm}\Gamma^k_{np}\right)\Big\}.
\end{aligned}
\tag{A.6}
$$

Or, in terms of derivatives of the components of the metric tensor,

$$
\begin{aligned}
(-g)\tau^{ik} = \frac{c^4}{16\pi G}\Bigg\{ & g^{ik}\frac{\partial g^{lm}}{\partial x^l}\frac{\partial g^{np}}{\partial x^n} - g^{il}g^{km}\frac{\partial g^{np}}{\partial x^l}\frac{\partial g_{mp}}{\partial x^n} + \frac{1}{2}g^{ik}g^{lm}\frac{\partial g^{np}}{\partial x^l}\frac{\partial g_{mp}}{\partial x^n} \\
& - \left[g^{il}g^{mn}\frac{\partial g^{kp}}{\partial x^l}\frac{\partial g_{mp}}{\partial x^n} + g^{kl}g^{mn}\frac{\partial g^{ip}}{\partial x^l}\frac{\partial g_{mp}}{\partial x^n}\right] \\
& + g^{lm}g^{np}g^{ik}g^{rs}\frac{\partial g_{ms}}{\partial x^q}\frac{\partial g_{pr}}{\partial x^n}g^{rs} \\
& + \frac{1}{8}\left(2g^{il}g^{km} - g^{ik}g^{jm}\right)\left(2g_{np}g_{qr} - g_{pq}g_{nr}\right)\frac{\partial g^{nr}}{\partial x^l}\frac{\partial g^{pq}}{\partial x^m}\Bigg\}
\end{aligned}
$$

where the indices $\in \{0, 1, 2, 3\}$.

## A.3 Spin-Weighted Spherical Harmonics

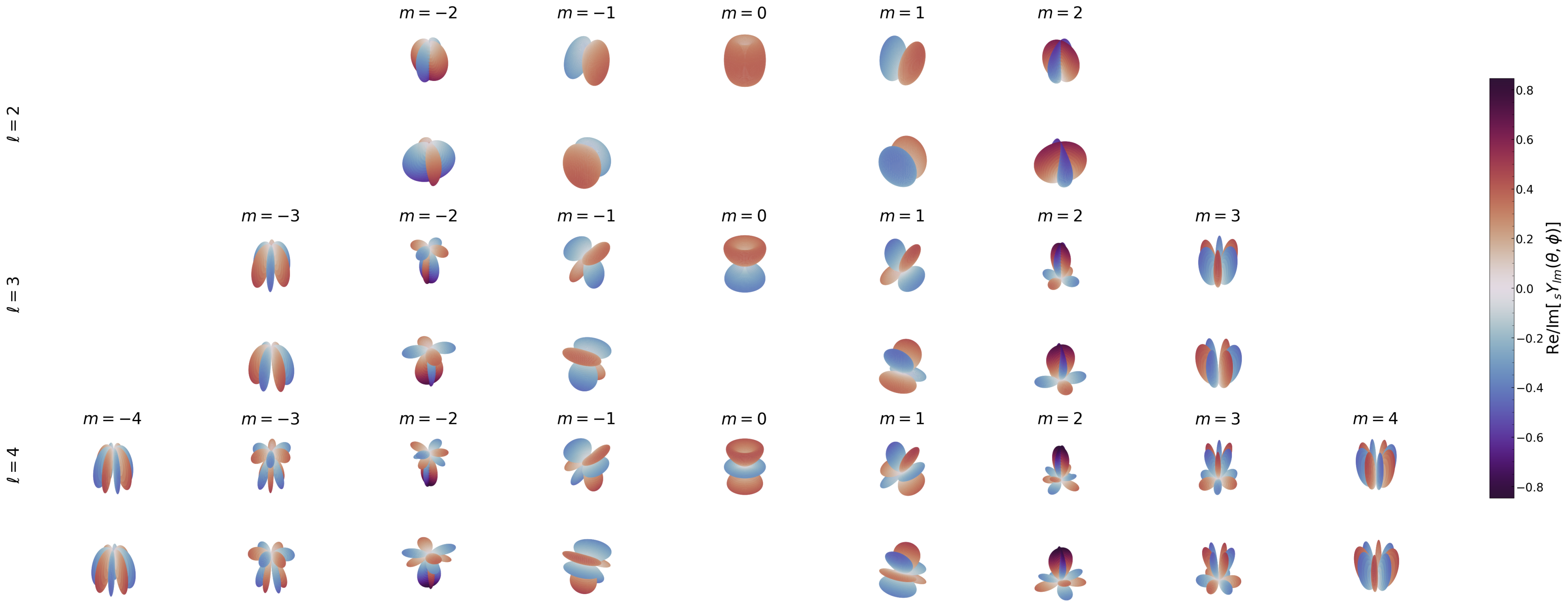


Figure A.1: Spin-weighted spherical harmonics $_sY_{lm}(\theta, \phi)$ for a spin weight of $s = -2$ and for $\ell$ values of 2, 3, and 4. For each $(\ell, m)$ mode, the top plot shows the real part and the bottom plot shows the imaginary part. The color indicates the normalized value of the function on the sphere. The mode $(\ell = 3, m = 2)$ is used on the front page.

## A.4 Planck window on the memory signal

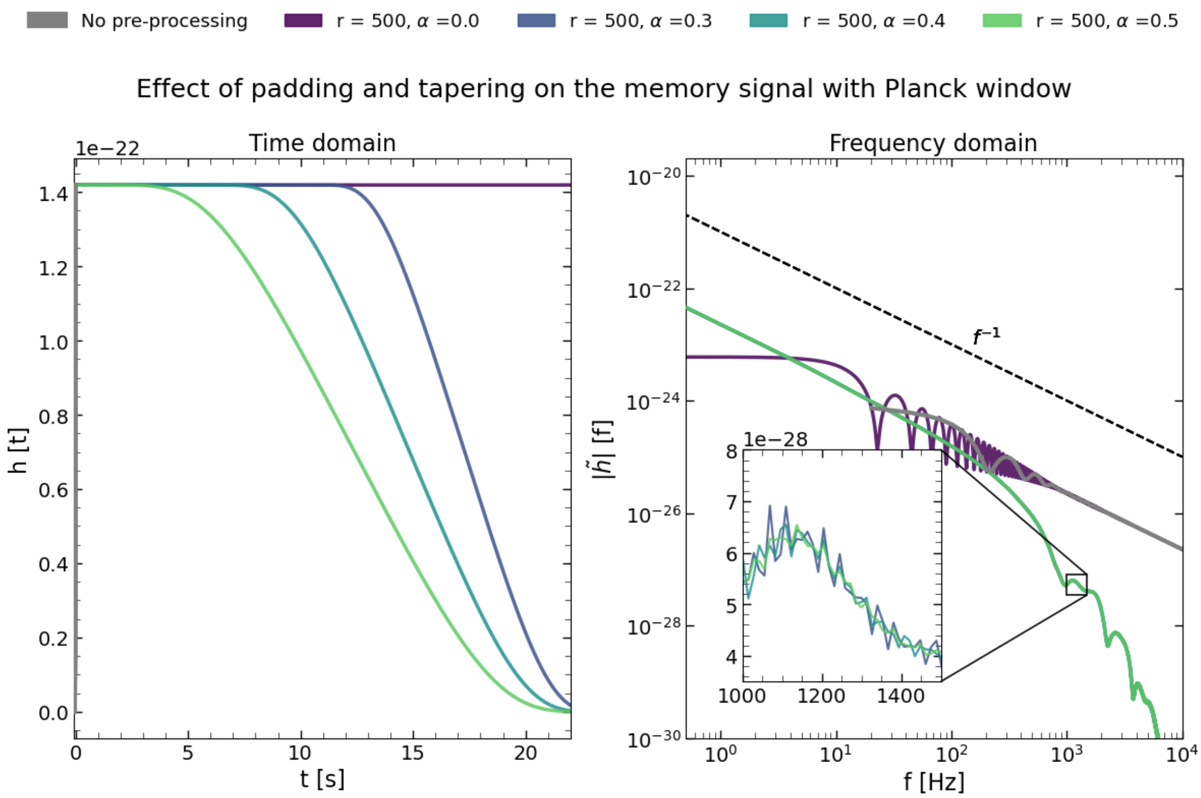


Figure A.2: Effect of both padding and tapering on the memory signal for the same parameter as in Fig. 2.2. In this case, the Planck window is used contrary to the Tukey window in this work. No major differences are present.

## A.5 Geometry of GRB jets

### A.5.1 Jet modeling

In this work, GRBs and their afterglow have been approximated by a simple accelerating point-particle associated with an energy $E_{\text{GRB, iso}}$. This point-like approximation can also be viewed as a jet with an infinitely narrow cross-section. We now wish to investigate the effect on the memory of a jet with a non-zero aperture. To do so, we will use the half-opening angle $\theta_j$ as the variable of interest. The results obtained are then the specific case $\theta_j = 0$.

The uniform (or top-hat) and structured models of jet GRBs were mentioned in the introduction and propose a uniform and layered geometry, respectively. We aim to compare these models with the case of a point-like jet at the same energy. To do this, we construct a model in which the emission is described by the sum of point-like contributions within the jet, modulated by a function $f(\theta)$ that describes the jet's structure. Furthermore, the function $f(\theta)$ is normalized to ensure energy conservation. Specifically, the energy of a point-like jet is more concentrated than that of a jet with $\theta_j$ not equal to zero. The jet distribution function $f(\theta)$ considered for our jet geometry is [120]:

I. Uniform jet:

$$f(\theta) = \begin{cases} 1 & \theta < \theta_j \ , \\ 0 & \theta > \theta_j . \end{cases} \tag{A.7}$$

II. Structured jet:

$$f(\theta) = \begin{cases} 1 & \theta < \Gamma^{-1} \ , \\ (\Gamma\theta)^{-2} & \Gamma^{-1} < \theta < \theta_j \ , \\ 0 & \theta > \theta_j \ , \end{cases} \tag{A.8}$$

where $\Gamma$ is the Lorentz factor and $\Gamma^{-1}$ is an estimate of the beam angle for a beam-shaped emission due to the relativistic effect. A plot of these functions along the jet's propagation axis is shown in Fig. A.3.

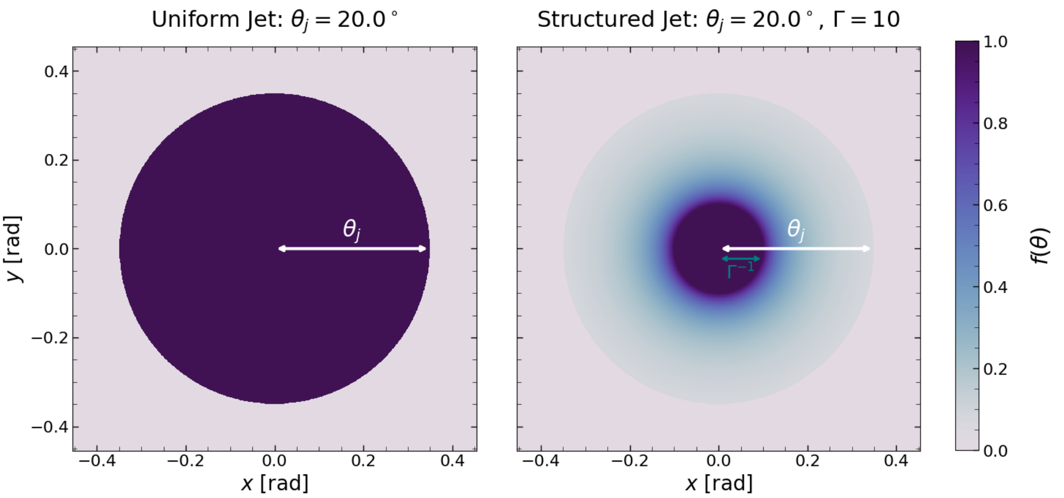


Figure A.3: Distribution within the jet described by $f(\theta)$ for the uniform model (*left*) and the structured model (*right*) with $\Gamma = 10$.

The total jet memory $\Delta h^{\mathrm{j}}_{\mathrm{GRB}}$ is constructed by superposing the point-particle memory $\Delta h^{\mathrm{pp}}_{\mathrm{GRB}}$ across the jet's opening angle, with each angular element weighted by the normalized energy density $f(\theta)$ at the corresponding viewing angle $\theta_{\mathrm{ej}}$. This yields [120]:

$$\Delta h^{\mathrm{j}}_{\mathrm{GRB}}(\theta_{\mathrm{ej}}) = \int f(\theta)\ \Delta h^{\mathrm{pp}}_{\mathrm{GRB}}(\theta, \phi, \theta_{\mathrm{ej}})\ \sin\theta\ d\theta d\phi\ . \tag{A.9}$$

where the integration is performed in the polar plane perpendicular to the direction of jet flow.

### A.5.2 Results for an off-axis observer

First, we investigate the evolution of the memory amplitude for an observer outside the jet. Fig. A.4 summarizes the results for the various models as well as the point-particle case. This latter remains constant (since it is, of course, independent of the jet opening angle) and will serve as a reference for the other models.

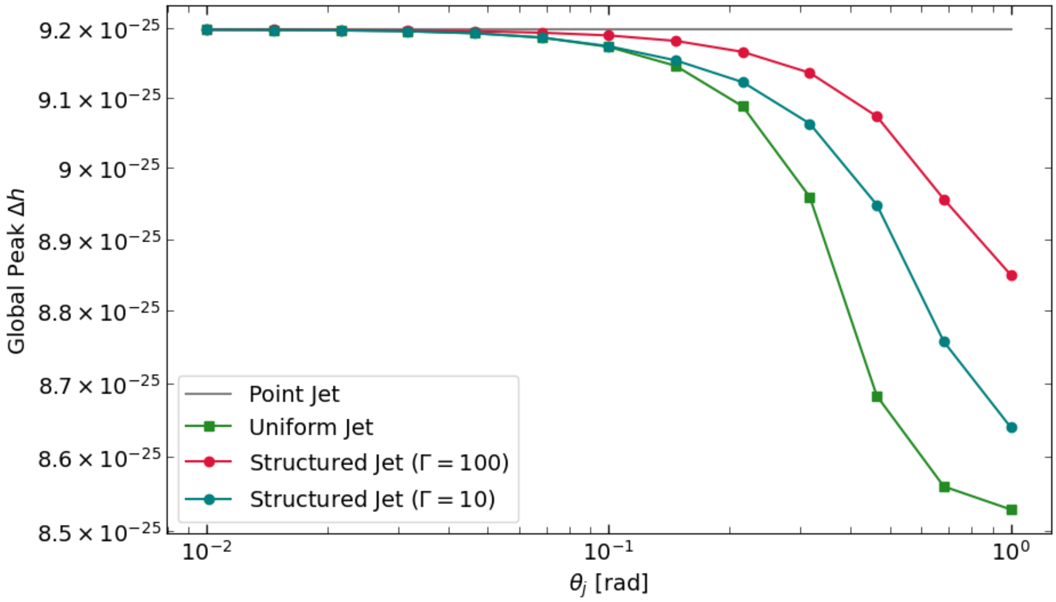


Figure A.4: Effect of the jet half-opening angle $\theta_j$ on the memory signal for a $10^{51}$ erg GRB with a prompt duration of $T_{90} = 10$ s, at a luminosity distance of 100 Mpc for an observer outside the jet axis and opening angle.

For angles $\theta_j \lesssim \Gamma^{-1}$, the models resemble point-particle jets, and the amplitude remains similar. As $\theta_j$ increases, the energy within the jet is spread over a larger area, resulting in a lower amplitude for each jet because of conservation of energy. For an off-axis observer, the memory is dominated by the edge of the jet closest to the line of sight. This explains why the amplitude decreases with $\theta_j$ as the closest jet energy is lower.

The decay rate also varies depending on the model. The memory decay is controlled by the distribution inside the jet: narrower, more collimated jets produce slower decline, while broader jets exhibit steeper falloff. This is for the same reason explained above. For structured jets, for example, the emission occurs mainly in the region around $\Gamma^{-1}$, thus, for these more collimated jets, the energy remains concentrated at the core and resembles a point-like source. A log-log fit returns a memory decay of $\theta_j^{-0.04}$ for the uniform model, $\theta_j^{-0.03}$ for the structured model ($\Gamma = 10$), and $\theta_j^{-0.02}$ for the structured model ($\Gamma = 100$). The estimated dependencies obtained are lower than those presented in the article [120], where the dependency is in the order of $\theta_j^{-0.1}$. Further analysis is needed to understand this difference, but the fact that only four opening angles ($\theta_j = 0.01, 0.05, 0.1, 0.2$) were considered in this study is one possible reason.

### A.5.3 Results for an on-axis observer

In this second case, we consider an observer along the jet axis ($\theta_{\rm ej} = 0$). In this configuration, the memory for a point-particle model is zero due to the anti-beaming effect. However, the other models exhibit off-axis emission, resulting in a non-zero memory. We find that the memory is approximately one order of magnitude smaller for a half-opening angle of $10^{-1}$ rad compared to the peak memory, as shown in Fig. A.5.

Furthermore, the wider the jet, the more emission causing a memory effect is present, and the larger the memory. For small openings ($\theta_j \lesssim 10^{-2}$), the memory from the different models is the same because their geometric effects do not dominate. A break occurs at $\theta_j = 10^{-2}$ and $\theta_j = 10^{-1}$ for the structured models with $\Gamma = 100$ and $\Gamma = 10$, respectively. The reason lies in their geometry, where the emission is mainly concentrated up to $\theta_j \lesssim \Gamma^{-1}$, beyond that the emission is weaker, resulting in a shallower slope.

To indicate the trend in the evolution of the maximum memory effect, a log-log fit provides a dependence $\Delta h^{\rm j}_{\rm GRB}(\theta_{\rm ej} = 0) \propto \theta_j^{1.9}$ for both the uniform and the structured model ($\Gamma = 10$) in the region where $\theta_j \in [10^{-2}, 10^{-1}]$. For $\theta_j \geqslant 10^{-1}$, the structured model ($\Gamma = 10$) grows as $\theta_j^{0.45}$. Finally, for the structured model ($\Gamma = 100$), the decay occurs at a shallower rate, yielding a weaker dependence of $\theta_j^{1.45}$ for the region $\theta_j \in [10^{-2}, 10^{-1}]$.

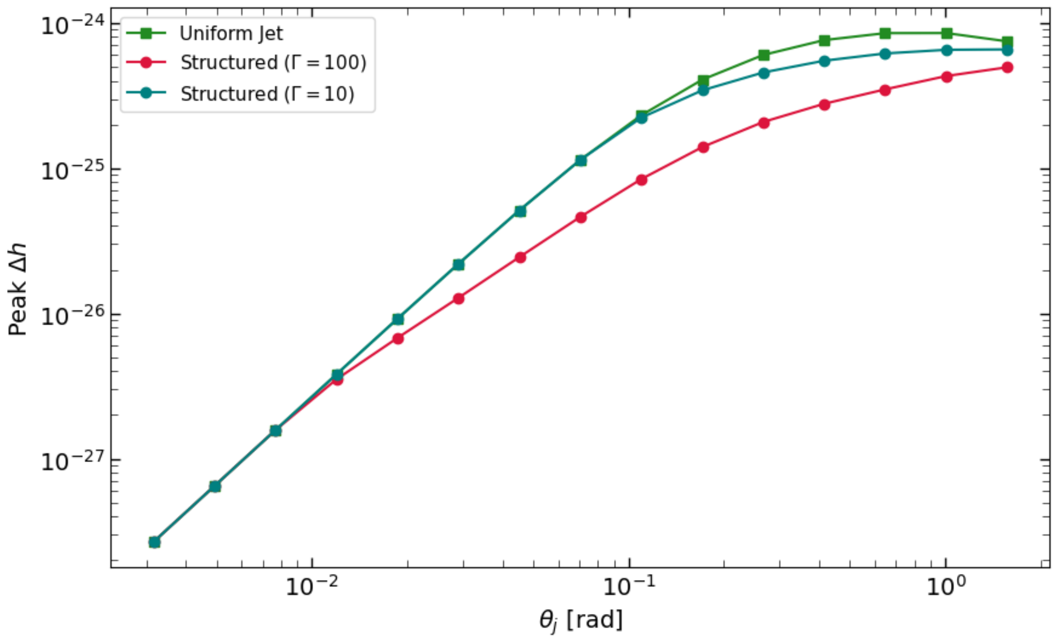


Figure A.5: Effect of the jet half-opening angle $\theta_j$ on the memory signal for a $10^{51}$ erg prompt GRB with a duration of $T_{90} = 10$ s at a luminosity distance of 100 Mpc for an observer along the jet axis.

## A.6 Angular dependence plots for plus polarization

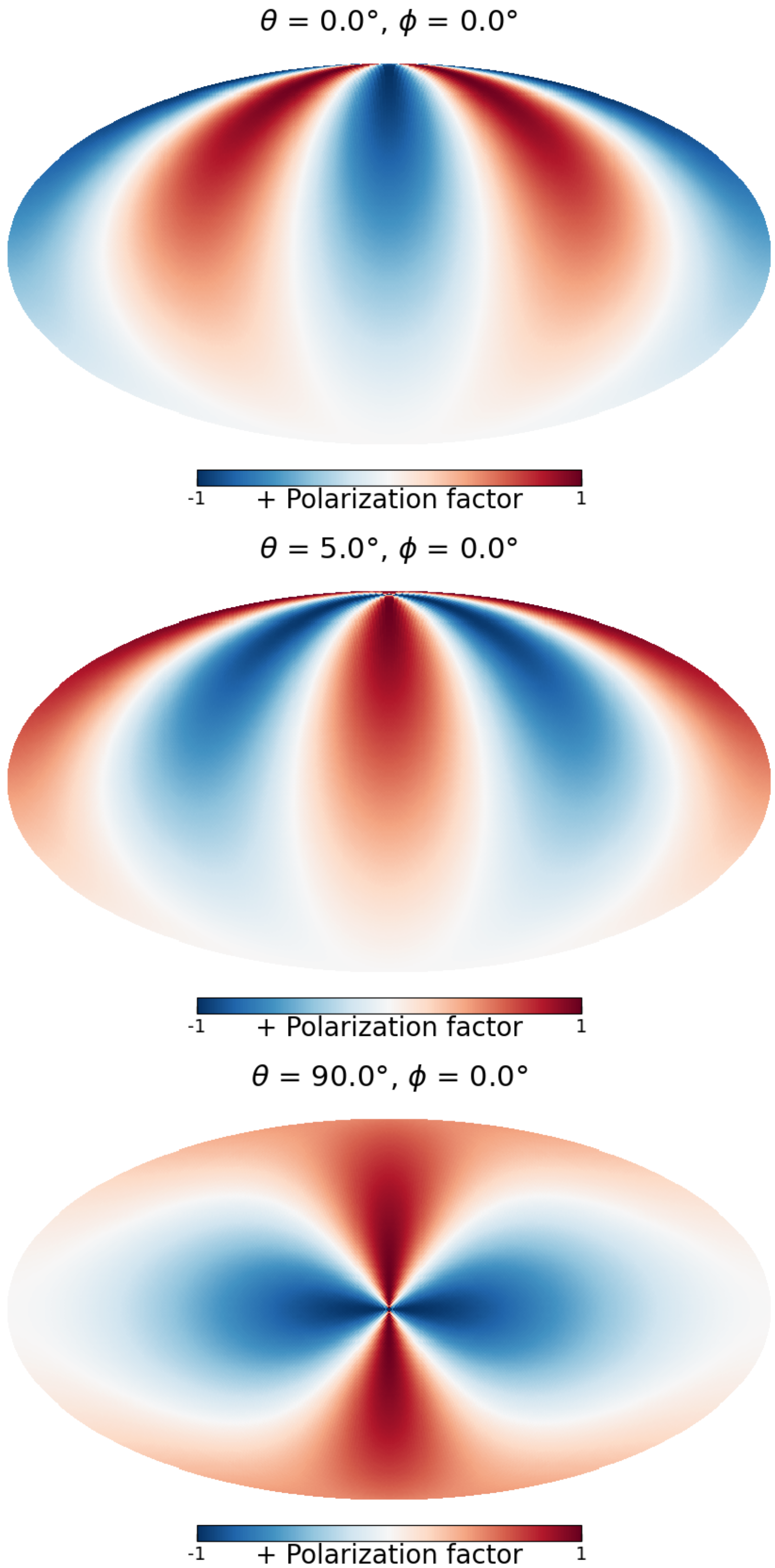


Figure A.6: Plus component of the angular factor projected defined in Eq. (3.50) for different viewing angles.

# Bibliography


[1] B. P. Abbott, R. Abbott, T. D. Abbott, et al., "Observation of gravitational waves from a binary black hole merger", Physical review letters **116**, 061102 (2016).

[2] A. Einstein, "Die grundlage der allgemeinen relativitätstheorie", Annalen der Physik **354**, 769–822 (1916), `https://onlinelibrary.wiley.com/doi/abs/10.1002/andp.19163540702`.

[3] C. M. Will, "The confrontation between general relativity and experiment", Living Reviews in Relativity **17**, `10.12942/lrr-2014-4` (2014), `http://dx.doi.org/10.12942/lrr-2014-4`.

[4] P. Jetzer, *Applications of general relativity: with problems*, 1st ed. (Springer, 2022), p. 195, `https://doi.org/10.1007/978-3-030-95718-6`.

[5] M. Favata, "The gravitational-wave memory effect", Classical and Quantum Gravity **27**, 084036 (2010).

[6] M. Favata, "Post-newtonian corrections to the gravitational-wave memory for quasicircular, inspiralling compact binaries", Physical Review D **80**, 024002 (2009), `http://arxiv.org/abs/0812.0069`.

[7] A. Nitz, I. Harry, D. Brown, et al., *Gwastro/pycbc: v2.3.3 release of pycbc*, version v2.3.3, Jan. 2024, `https://doi.org/10.5281/zenodo.10473621`.

[8] C. Talbot, E. Thrane, P. D. Lasky, and F. Lin, *Gwmemory: a python package for calculating gravitational-wave memory*, version 1.0.6, Python package for gravitational wave memory calculations using SEOBNRv4 approximant, 2019, `https://github.com/ColmTalbot/gwmemory`.

[9] Y. B. Zel'dovich and A. G. Polnarev, "Radiation of gravitational waves by a cluster of superdense stars", sovast **18**, 17 (1974).

[10] V. B. Braginskii and L. P. Grishchuk, "Kinematic resonance and the memory effect in free mass gravitational antennas", Zhurnal Eksperimentalnoi i Teoreticheskoi Fiziki **89**, 744–750 (1985).

[11] V. B. Braginsky and K. S. Thorne, "Gravitational-wave bursts with memory and experimental prospects", Nature **327**, 123–125 (1987).

[12] A. Burrows and J. Hayes, "Pulsar recoil and gravitational radiation due to asymmetrical stellar collapse and explosion", Physical Review Letters **76**, 352–355 (1996), `http://dx.doi.org/10.1103/PhysRevLett.76.352`.

[13] M. Turner, "Gravitational radiation from point-masses in unbound orbits: Newtonian results.", Astrophysical Journal **216**, 610–619 (1977).

[14] N. Sago, K. Ioka, T. Nakamura, and R. Yamazaki, “Gravitational wave memory of gamma-ray burst jets”, Physical Review D **70**, 10.1103/physrevd.70.104012 (2004), http://dx.doi.org/10.1103/PhysRevD.70.104012.

[15] L. Blanchet and T. Damour, “Hereditary effects in gravitational radiation”, Physical Review D **46**, 4304–4319 (1992), https://link.aps.org/doi/10.1103/PhysRevD.46.4304.

[16] D. Christodoulou, “Nonlinear nature of gravitation and gravitational-wave experiments”, Physical Review Letters. **67**, 1486–1489 (1991), https://link.aps.org/doi/10.1103/PhysRevLett.67.1486.

[17] K. S. Thorne, “Gravitational-wave bursts with memory: the christodoulou effect”, Physical Review D **45**, 520–524 (1992), https://link.aps.org/doi/10.1103/PhysRevD.45.520.

[18] L. Bieri, P. Chen, and S.-T. Yau, *Null asymptotics of solutions of the einstein-maxwell equations in general relativity and gravitational radiation*, 2010, https://arxiv.org/abs/1011.2267.

[19] A. G. Wiseman and C. M. Will, “Christodoulou’s nonlinear gravitational-wave memory: evaluation in the quadrupole approximation”, Physical Review D **44**, R2945 (1991).

[20] S. M. Du and A. Nishizawa, “Gravitational wave memory: a new approach to study modified gravity”, Physical Review D **94**, 104063 (2016), https://link.aps.org/doi/10.1103/PhysRevD.94.104063.

[21] M. Favata, “Nonlinear gravitational-wave memory from binary black hole mergers”, The Astrophysical Journal **696**, L159–L162 (2009), http://arxiv.org/abs/0902.3660 (visited on 08/03/2025).

[22] A. Strominger and A. Zhiboedov, “Gravitational memory, bms supertranslations and soft theorems”, Journal of High Energy Physics **2016**, 1–15 (2016).

[23] K. T. McDonald, “What is the stiffness of spacetime?”, https://kirkmcd.princeton.edu/examples/stiffness.pdf.

[24] I. Belahcene, “Searching for gravitational waves produced by cosmic strings in ligo-virgo data”, PhD thesis (Oct. 2019), https://theses.hal.science/tel-02878783v1/file/82248_BELAHCENE_2019_archivage.pdf.

[25] “Kagra: 2.5 generation interferometric gravitational wave detector”, Nature Astronomy **3**, 35–40 (2019).

[26] H. Middleton et al., “Communicating the gravitational-wave discoveries of the LIGO-Virgo-KAGRA Collaboration”, Journal of Science Communication **23**, N03 (2024).

[27] LIGO Scientific Collaboration, *Ligo’s interferometer*, LIGO Caltech, (2023) https://www.ligo.caltech.edu/page/ligos-ifo.

[28] D. V. Martynov, E. Hall, B. Abbott, et al., “Sensitivity of the advanced ligo detectors at the beginning of gravitational wave astronomy”, Physical Review D **93**, 112004 (2016).

[29] J. Aasi, B. P. Abbott, R. Abbott, et al., “Advanced ligo”, Classical and Quantum Gravity **32**, 074001 (2015), http://dx.doi.org/10.1088/0264-9381/32/7/074001.

[30] University of Glasgow, School of Physics & Astronomy, Institute for Gravitational Research, *Signal recycling*, Accessed 2025-09-29, (2025) `https://www.gla.ac.uk/schools/physics/research/groups/igr/research/signalrecycling/`.

[31] F. Acernese, M. Agathos, L. Aiello, et al., "Advanced virgo: a second-generation interferometric gravitational wave detector", Classical and Quantum Gravity **32**, 024001 (2015), `https://doi.org/10.1088/0264-9381/32/2/024001`.

[32] L. S. Collaboration, V. Collaboration, F. GBM, et al., "Multi-messenger observations of a binary neutron star merger", The Astrophysical Journal Letters **848**, L12 (2017), `http://arxiv.org/abs/1710.05833` (visited on 10/03/2025).

[33] R. Abbott, T. D. Abbott, F. Acernese, et al., "Gwtc-3: compact binary coalescences observed by ligo and virgo during the second part of the third observing run", Physical Review X **13**, `10.1103/physrevx.13.041039` (2023), `http://dx.doi.org/10.1103/PhysRevX.13.041039`.

[34] B. P. Abbott, R. Abbott, T. D. Abbott, et al., "Gw190425: observation of a compact binary coalescence with total mass$\sim 3.4M_{\odot}$", The Astrophysical Journal Letters **892**, L3 (2020), `http://dx.doi.org/10.3847/2041-8213/ab75f5`.

[35] R. Abbott, T. D. Abbott, S. Abraham, et al., "Observation of gravitational waves from two neutron star–black hole coalescences", The Astrophysical Journal Letters **915**, L5 (2021), `http://dx.doi.org/10.3847/2041-8213/ac082e`.

[36] M. Szczepanczyk et al., "Detecting and reconstructing gravitational waves from the next galactic core-collapse supernova in the advanced detector era", Physical Review D **104**, 102002 (2021).

[37] LIGO Scientific Collaboration and Virgo Collaboration and KAGRA Collaboration, *GWTC-4.0*, `https://gwosc.org/eventapi/html/GWTC-4.0/`, Accessed: 2026-04-03, Gravitational Wave Open Science Center (GWOSC), 2025.

[38] M.-A. Weinstein and J. Kanner, "A study of gravitational wave memory and its detectability with ligo using bayesian inference interim report", (2018).

[39] M. Punturo, M. Abernathy, F. Acernese, et al., "The einstein telescope: a third-generation gravitational wave observatory", Classical and Quantum Gravity **27**, 194002 (2010), `https://doi.org/10.1088/0264-9381/27/19/194002`.

[40] P. Amaro-Seoane, J. Andrews, M. Arca Sedda, et al., "Astrophysics with the laser interferometer space antenna", Living Reviews in Relativity **26**, `10.1007/s41114-022-00041-y` (2023), `http://dx.doi.org/10.1007/s41114-022-00041-y`.

[41] *Laser interferometer space antenna*, Accessed: 2025-10-13, Wikipédia, (2024) `https://fr.wikipedia.org/wiki/Laser_Interferometer_Space_Antenna`.

[42] F.-I. für Lasertechnik ILT, *Einstein telescope could launch a new era in astronomy*, Accessed: 2025-10-13, (June 12, 2024) `https://phys.org/news/2024-06-einstein-telescope-era-astronomy.html`.

[43] A. Sesana, M. Volonteri, and F. Haardt, "Lisa detection of massive black hole binaries: imprint of seed populations and extreme recoils", Classical and Quantum Gravity **26**, 094033 (2009).

[44] M. Maggiore, C. Van Den Broeck, N. Bartolo, et al., "Science case for the einstein telescope", Journal of Cosmology and Astroparticle Physics **2020**, 050 (2020).

[45] M. D. Becker, *Astrophysics course*, 2025, `https://www.programmes.uliege.be/cocoon/20252026/en/cours/SPAT0033-1.html`.

[46] L. Rezzolla, E. R. Most, and L. R. Weih, “Using gravitational-wave observations and quasi-universal relations to constrain the maximum mass of neutron stars”, The Astrophysical Journal Letters **852**, L25 (2018).

[47] B. D. Metzger, “Kilonovae”, Living Reviews in Relativity **23**, 1 (2020), `http://arxiv.org/abs/1910.01617` (visited on 10/03/2025).

[48] D. Kasen, B. Metzger, J. Barnes, E. Quataert, and E. Ramirez-Ruiz, “Origin of the heavy elements in binary neutron-star mergers from a gravitational-wave event”, Nature **551**, 80–84 (2017).

[49] D. Finstad, S. De, D. A. Brown, E. Berger, and C. M. Biwer, “Measuring the viewing angle of gw170817 with electromagnetic and gravitational waves”, The Astrophysical Journal Letters **860**, L2 (2018), `http://dx.doi.org/10.3847/2041-8213/aac6c1`.

[50] V. A. Villar, J. Guillochon, E. Berger, et al., “The combined ultraviolet, optical, and near-infrared light curves of the kilonova associated with the binary neutron star merger gw170817: unified data set, analytic models, and physical implications”, The Astrophysical Journal Letters **851**, L21 (2017).

[51] Z. Ji, J. Chen, and G. Wu, “Insights into Neutron Star Matter: EoS Models and Observations”, (2025).

[52] K. Kawaguchi, M. Shibata, and M. Tanaka, “Diversity of kilonova light curves”, The Astrophysical Journal **889**, 171 (2020).

[53] A. Perego, S. Rosswog, R. M. Cabezón, et al., “Neutrino-driven winds from neutron star merger remnants”, Monthly Notices of the Royal Astronomical Society **443**, 3134–3156 (2014).

[54] R. Mochkovitch, F. Daigne, R. Duque, and H. Zitouni, “Prospects for kilonova signals in the gravitational-wave era”, Astronomy & Astrophysics **651**, A83 (2021).

[55] H. Koehn, T. Wouters, P. T. H. Pang, et al., “Efficient bayesian analysis of kilonovae and gamma ray burst afterglows with fiesta”, Astronomy & Astrophysics **704**, A55 (2025), `http://dx.doi.org/10.1051/0004-6361/202556626`.

[56] J. Granot, *The structure and dynamics of grb jets*, 2006, `https://arxiv.org/abs/astro-ph/0610379`.

[57] J. Granot, “Gamma-ray bursts from magnetic reconnection: variability and robustness of light curves”, The Astrophysical Journal Letters **816**, L20 (2016), `http://dx.doi.org/10.3847/2041-8205/816/2/L20`.

[58] S. Dado and A. Dar, *Critical tests of leading gamma ray burst theories*, 2019, `https://arxiv.org/abs/1810.03514`.

[59] R. Poggiani, “Gw170817: a short review of the first multimessenger event in gravitational astronomy”, Galaxies **13**, `10.3390/galaxies13050112` (2025), `https://www.mdpi.com/2075-4434/13/5/112`.

[60] T. Ahumada, L. P. Singer, S. Anand, et al., “Discovery and confirmation of the shortest gamma-ray burst from a collapsar”, Nature Astronomy **5**, 917–927 (2021), `http://dx.doi.org/10.1038/s41550-021-01428-7`.

[61] J. C. Rastinejad, B. P. Gompertz, A. J. Levan, et al., “A kilonova following a long-duration gamma-ray burst at 350 mpc”, Nature **612**, 223–227 (2022), `http://dx.doi.org/10.1038/s41586-022-05390-w`.

[62] M. Pillas, “Exploring the physics of neutron star mergers with gravitational waves and gamma-ray bursts”, PhD thesis (Université Paris-Saclay, 2023), `https://theses.hal.science/tel-04302425`.

[63] B. P. Abbott, R. Abbott, T. D. Abbott, et al., “Gravitational waves and gamma-rays from a binary neutron star merger: gw170817 and grb 170817a”, The Astrophysical Journal Letters **848**, L13 (2017), `http://dx.doi.org/10.3847/2041-8213/aa920c`.

[64] M. Axelsson, M. Ajello, M. Arimoto, et al., *Grb 221009a: the b.o.a.t burst that shines in gamma rays*, 2024, `https://arxiv.org/abs/2409.04580`.

[65] S. Lesage, P. Veres, M. S. Briggs, et al., “Fermi-gbm discovery of grb 221009a: an extraordinarily bright grb from onset to afterglow”, The Astrophysical Journal Letters **952**, L42 (2023), `http://dx.doi.org/10.3847/2041-8213/ace5b4`.

[66] Z. Cao, F. Aharonian, Q. An, et al., “A tera–electron volt afterglow from a narrow jet in an extremely bright gamma-ray burst”, Science **380**, 1390–1396 (2023), `http://dx.doi.org/10.1126/science.adg9328`.

[67] B. Zhang, Y. Z. Fan, J. Dyks, et al., “Physical Processes Shaping Gamma-Ray Burst X-Ray Afterglow Light Curves: Theoretical Implications from the Swift X-Ray Telescope Observations”, Astrophysical Journal **642**, 354–370 (2006).

[68] Y.-Z. Fan, T. Piran, and D.-M. Wei, “Central engine afterglow of gamma-ray bursts”, in Aip conference proceedings, Vol. 968, 1 (American Institute of Physics, 2008), pp. 32–35.

[69] J. A. Nousek, C. Kouveliotou, D. Grupe, et al., “Evidence for a Canonical Gamma-Ray Burst Afterglow Light Curve in the Swift XRT Data”, Astrophysical Journal **642**, 389–400 (2006).

[70] M. Maggiore, *Gravitational Waves. Vol. 1: Theory and Experiments* (Oxford University Press, 2007).

[71] S. M. Carroll, *Spacetime and geometry, A no-nonsense introduction to general relativity* (Addison-Wesley, San Francisco, 2001).

[72] S. M. Carroll, *Spacetime and geometry: an introduction to general relativity* (Cambridge University Press, 2019).

[73] L. Blanchet, “Gravitational radiation from post-newtonian sources and inspiralling compact binaries”, Living Reviews in Relativity **5**, `10.12942/lrr-2002-3` (2002), `http://dx.doi.org/10.12942/lrr-2002-3`.

[74] E. Bertschinger, *Number-flux vector and stress-energy tensor*, Massachusetts Institute of Technology, (2002) `https://web.mit.edu/edbert/GR/gr2b.pdf#page=3.42`.

[75] L. D. Landau and E. M. Lifshitz, *The classical theory of fields*, Fourth Revised English Edition, Vol. 2, Course of Theoretical Physics (Pergamon Press, 1975).

[76] C. Talbot, E. Thrane, P. D. Lasky, and F. Lin, “Gravitational-wave memory: waveforms and phenomenology”, Physical Review D **98**, 064031 (2018), `https://arxiv.org/pdf/1807.00990`.

[77] D. Lopez, S. Tiwari, and M. Ebersold, “Gravitational wave memory of compact binary coalescence in the presence of matter effects”, Physical Review D **109**, `10.1103/physrevd.109.043039` (2024), `http://dx.doi.org/10.1103/PhysRevD.109.043039`.

[78] Y. Xu, M. Rosselló-Sastre, S. Tiwari, et al., "Enhancing gravitational wave parameter estimation with nonlinear memory: breaking the distance-inclination degeneracy", Physical Review D **109**, 10.1103/physrevd.109.123034 (2024), http://dx.doi.org/10.1103/PhysRevD.109.123034.

[79] E. T. Newman and R. Penrose, "Note on the bondi-metzner-sachs group", Journal of Mathematical Physics **7**, 863–870 (1966), https://pubs.aip.org/jmp/article/7/5/863/234092/Note-on-the-Bondi-Metzner-Sachs-Group (visited on 12/10/2025).

[80] G. Torres del Castillo, "Spin-weighted spherical harmonics and their applications", Revista mexicana de física **53**, 125–134 (2007).

[81] W. B. Campbell, "Tensor and spinor spherical harmonics and the spin-s harmonics sYlm", Journal of Mathematical Physics **12**, _eprint: https://pubs.aip.org/aip/jmp/article-pdf/12/8/1763/19114184/1763_1_online.pdf, 1763–1770 (1971), https://doi.org/10.1063/1.1665802.

[82] J. Zosso, S. Gasparotto, A. Cogez, et al., *Towards claiming a detection of gravitational memory*, tech. rep. (2026).

[83] Wikipedia contributors, *Wigner d-matrix — Wikipedia, the free encyclopedia*, [Online; accessed 13-December-2025], 2025, https://en.wikipedia.org/w/index.php?title=Wigner_D-matrix&oldid=1322920597.

[84] E. P. Wigner and U. Fano, "Group Theory and Its Application to the Quantum Mechanics of Atomic Spectra", American Journal of Physics **28**, 408–409 (1960).

[85] A. Cogez, S. Gasparotto, J. Zosso, et al., *Detectability of gravitational-wave memory with lisa: a bayesian approach*, 2026, https://arxiv.org/abs/2601.23230.

[86] A. Buonanno, B. R. Iyer, E. Ochsner, Y. Pan, and B. S. Sathyaprakash, "Comparison of post-newtonian templates for compact binary inspiral signals in gravitational-wave detectors", Physical Review D **80**, 10.1103/physrevd.80.084043 (2009), http://dx.doi.org/10.1103/PhysRevD.80.084043.

[87] S. E. Field, V. Varma, J. Blackman, et al., "GWSurrogate: A Python package for gravitational wave surrogate models", J. Open Source Softw. **10**, 7073 (2025).

[88] V. Varma, S. E. Field, M. A. Scheel, et al., "Surrogate models for precessing binary black hole simulations with unequal masses", Physical Review Research **1**, 10.1103/physrevresearch.1.033015 (2019), http://dx.doi.org/10.1103/PhysRevResearch.1.033015.

[89] V. Varma, S. E. Field, M. A. Scheel, et al., "Surrogate model of hybridized numerical relativity binary black hole waveforms", Physical Review D **99**, 10.1103/physrevd.99.064045 (2019), http://dx.doi.org/10.1103/PhysRevD.99.064045.

[90] J. Yoo, V. Varma, M. Giesler, et al., "Targeted large mass ratio numerical relativity surrogate waveform model for gw190814", Physical Review D **106**, 10.1103/physrevd.106.044001 (2022), http://dx.doi.org/10.1103/PhysRevD.106.044001.

[91] J. Yoo, K. Mitman, V. Varma, et al., "Numerical relativity surrogate model with memory effects and post-newtonian hybridization", Physical Review D **108**, 10.1103/physrevd.108.064027 (2023), http://dx.doi.org/10.1103/PhysRevD.108.064027.

[92] O. M. Boersma, D. A. Nichols, and P. Schmidt, “Forecasts for detecting the gravitational-wave memory effect with advanced ligo and virgo”, Physical Review D **101**, 10.1103/physrevd.101.083026 (2020), http://dx.doi.org/10.1103/PhysRevD.101.083026.

[93] J. Valencia, R. Tenorio, M. Rosselló-Sastre, and S. Husa, “Frequency-domain analysis of gravitational-wave memory waveforms”, Physical Review D **110**, 10.1103/physrevd.110.124026 (2024), http://dx.doi.org/10.1103/PhysRevD.110.124026.

[94] E. O. Brigham and R. E. Morrow, “The fast fourier transform”, IEEE Spectrum **4**, 63–70 (1967).

[95] F. Miller, A. Vandome, and J. McBrewster, *Nyquist-shannon sampling theorem: aliasing, sine wave, signal processing, nyquist rate, nyquist frequency, sampling rate, shannon-hartley theorem, whittaker-shannon interpolation formula, reconstruction from zero crossings* (Alphascript Publishing, 2010), https://books.google.be/books?id=lPvtQQAACAAJ.

[96] L. Surhone, M. Timpledon, and S. Marseken, *Spectral leakage* (VDM Publishing, 2010), https://books.google.be/books?id=7-5BXwAACAAJ.

[97] A. Cogez, S. Gasparotto, J. Zosso, et al., *Detectability of gravitational-wave memory with lisa: a bayesian approach*, 2026, https://arxiv.org/abs/2601.23230.

[98] B.-Q. Huang, T. Liu, L. Xue, and Y.-Q. Qi, “Low-frequency gravitational-wave memories from gamma-ray burst afterglows with energy injections”, The Astrophysical Journal **944**, 189 (2023), http://dx.doi.org/10.3847/1538-4357/acb76f.

[99] M. Mukhopadhyay, C. Cardona, and C. Lunardini, “The neutrino gravitational memory from a core collapse supernova: phenomenology and physics potential”, Journal of Cosmology and Astroparticle Physics **2021**, 055 (2021), http://dx.doi.org/10.1088/1475-7516/2021/07/055.

[100] E. Nakar, “The electromagnetic counterparts of compact binary mergers”, Physics Reports **886**, 1–84 (2020), http://dx.doi.org/10.1016/j.physrep.2020.08.008.

[101] D. Lazzati, R. Perna, B. J. Morsony, et al., “Late time afterglow observations reveal a collimated relativistic jet in the ejecta of the binary neutron star merger gw170817”, Physical Review Letters **120**, 10.1103/physrevlett.120.241103 (2018), http://dx.doi.org/10.1103/PhysRevLett.120.241103.

[102] R. Sari and T. Piran, “Predictions for the very early afterglow and the optical flash”, The Astrophysical Journal **520**, 641–649 (1999), http://dx.doi.org/10.1086/307508.

[103] J. D. Salmonson, “Perspective on afterglows: numerically computed views, light curves, and the analysis of homogeneous and structured jets with lateral expansion”, The Astrophysical Journal **592**, 1002–1017 (2003), http://dx.doi.org/10.1086/375580.

[104] A. Panaitescu, “Jet breaks in the x-ray light-curves of swift gamma-ray burst afterglows: jet breaks in swift afterglows”, Monthly Notices of the Royal Astronomical Society **380**, 374–380 (2007), http://dx.doi.org/10.1111/j.1365-2966.2007.12084.x.

[105] R. Sari, T. Piran, and J. P. Halpern, “Jets in gamma-ray bursts”, The Astrophysical Journal **519**, L17–L20 (1999), `http://dx.doi.org/10.1086/312109`.

[106] J. Bamber, A. Tsokaros, M. Ruiz, et al., “Gravitational wave memory from binary neutron star mergers”, Physical Review Letters **136**, `10.1103/k3hl-4n82` (2026), `http://dx.doi.org/10.1103/k3hl-4n82`.

[107] M. Bulla, “Possis: predicting spectra, light curves, and polarization for multidimensional models of supernovae and kilonovae”, Monthly Notices of the Royal Astronomical Society **489**, 5037–5045 (2019).

[108] T. Dietrich, M. W. Coughlin, P. T. H. Pang, et al., “Multimessenger constraints on the neutron-star equation of state and the Hubble constant”, Science **370**, 1450–1453 (2020).

[109] Z. Cao, F. Aharonian, Q. An, et al., “A tera–electron volt afterglow from a narrow jet in an extremely bright gamma-ray burst”, Science **380**, 1390–1396 (2023), `http://dx.doi.org/10.1126/science.adg9328`.

[110] L. Zhou and Y.-C. Zou, *Determining the viewing angle from tev light curve of grb 221009a*, 2024, `https://arxiv.org/abs/2407.03743`.

[111] B. P. Gompertz, A. J. Levan, T. Laskar, et al., *Jwst spectroscopy of grb 250702b: an extremely rare and exceptionally energetic burst in a dusty, massive galaxy at* $z = 1.036$, 2025, `https://arxiv.org/abs/2509.22778`.

[112] E. Neights, E. Burns, C. L. Fryer, et al., “Grb 250702b: discovery of a gamma-ray burst from a black hole falling into a star”, Monthly Notices of the Royal Astronomical Society **545**, `10.1093/mnras/staf2019` (2025), `http://dx.doi.org/10.1093/mnras/staf2019`.

[113] Z.-Y. Li and R. A. Chevalier, “Radio supernova sn 1998bw and its relation to grb 980425”, The Astrophysical Journal **526**, 716–726 (1999), `http://dx.doi.org/10.1086/308031`.

[114] T. Ahumada, L. P. Singer, S. Anand, et al., “Discovery and confirmation of the shortest gamma-ray burst from a collapsar”, Nature Astronomy **5**, 917–927 (2021), `http://dx.doi.org/10.1038/s41550-021-01428-7`.

[115] J. C. Rastinejad, B. P. Gompertz, A. J. Levan, et al., “A kilonova following a long-duration gamma-ray burst at 350 mpc”, Nature **612**, 223–227 (2022), `http://dx.doi.org/10.1038/s41586-022-05390-w`.

[116] Astropy Collaboration, A. M. Price-Whelan, P. L. Lim, et al., “The Astropy Project: Sustaining and Growing a Community-oriented Open-source Project and the Latest Major Release (v5.0) of the Core Package”, Astrophysical Journal **935**, 167, 167 (2022).

[117] LISA Consortium, *LISA Data Challenges (LDC) – Documentation*, `https://lisa.pages.in2p3.fr/LDC/`, Accessed: 4/11/2026.

[118] A. von Kienlin, C. A. Meegan, W. S. Paciesas, et al., “The fourth fermi-gbm gamma-ray burst catalog: a decade of data”, The Astrophysical Journal **893**, 46 (2020), `http://dx.doi.org/10.3847/1538-4357/ab7a18`.

[119] H.-Y. Yuan, H.-J. Lü, Y. Li, et al., “Probing the progenitor of high- <i>z</i> short-duration grb 201221d and its possible bulk acceleration in prompt emission”, Research in Astronomy and Astrophysics **22**, 075011 (2022), `http://dx.doi.org/10.1088/1674-4527/ac712d`.

[120] O. Birnholtz and T. Piran, "Gravitational wave memory from gamma ray bursts' jets", Physical Review D **87**, 10.1103/physrevd.87.123007 (2013), http://dx.doi.org/10.1103/PhysRevD.87.123007.